RSC Advances

ROYAL SOCIETY OF CHEMISTRY

PAPER

View Article Online
View Journal | View Issue

Cite this: *RSC Adv.*, 2025, **15**, 44711

Comprehensive first-principles analysis and device simulations of vacancy-ordered D_2CeX_6 double perovskites for high-efficiency lead-free solar cells

Rifat Rafiu,[a] Karim Kriaa,[b] Md. Sakib Hasan Saikot,[a] Md. Azizur Rahman, *[c] Imtiaz Ahamed Apon,[d] N. Sfina,[e] Mohd Taukeer Khan,[f] Noureddine Elboughdiri,[g] S. AlFaify[h] and Imtiaz Ahmmed Talukder[c]

The quest for efficient and durable absorber materials has steered attention toward vacancy-ordered double perovskites, which exhibit tunable band gaps and strong optical absorption, making them promising candidates for next-generation solar cell architectures. In particular, lead-free vacancy-ordered halide double perovskites have emerged as viable alternatives to toxic Pb-based counterparts. In this study, we systematically investigate the structural, electronic, charges density, mechanical, optical, phonon stability, molecular dynamics (MD), population analysis and photovoltaic properties of D_2CeX_6 (D = Ga, In, Tl; X = Cl, Br) compounds by employing first-principles calculations in conjunction with SCAPS-1D device simulations. Our results reveal that all compounds crystallize in a stable cubic phase with negative formation enthalpies, confirming their thermodynamic stability. Within GGA–PBE, the calculated direct band gaps are 1.733 eV (Ga_2CeCl_6), 1.276 eV (Ga_2CeBr_6), 1.555 eV (In_2CeCl_6), 0.859 eV (In_2CeBr_6), 1.755 eV (Tl_2CeCl_6), and 1.364 eV (Tl_2CeBr_6), placing all but In_2CeBr_6 within or near the optimal 1.1 to 1.8 eV range for single-junction solar cells. HSE06 hybrid functional results yield wider gaps of 1.776 eV, 2.843 eV, 2.261 eV, 2.170 eV, 3.632 eV, and 1.418 eV, respectively, suggesting suitability for both single-junction and tandem architectures. Optical analyses demonstrate high absorption coefficients (>10^5 cm^{-1}), strong dielectric responses, and large refractive indices, particularly in In_2CeBr_6 and Tl_2CeBr_6. Mechanical evaluations confirm ductile behavior, with Tl_2CeBr_6 and In_2CeBr_6 exhibiting superior stiffness and near-isotropic mechanical stability. Molecular dynamics simulations (NPT ensemble, 50 ps) at room temperature confirm the excellent thermal robustness of the studied compounds. The phonon dispersion analysis further indicates full dynamical stability for Ga_2CeCl_6, In_2CeCl_6, and Tl_2CeCl_6, while Ga_2CeBr_6, In_2CeBr_6, and Tl_2CeBr_6 exhibit minor soft or near-zero modes that are likely stabilized by finite-temperature effects. Device-level simulations predict power conversion efficiencies (PCE) up to 25.29% for Ga_2CeBr_6, with In_2CeCl_6 and Tl_2CeBr_6 also exceeding 24%. These findings position the D_2CeX_6 family, especially bromide-based compounds, as promising candidates for efficient and stable lead-free perovskite solar cells.

Received 22nd September 2025
Accepted 11th November 2025

DOI: 10.1039/d5ra07162c

rsc.li/rsc-advances

1 Introduction

The global energy landscape is undergoing a profound transformation as the urgency to reduce dependence on fossil fuels and mitigate the impacts of climate change continues to intensify. Among the portfolio of renewable technologies, solar photovoltaics (PVs) have emerged as one of the most promising candidates, offering clean, abundant, and sustainable electricity generation.[1,2] While silicon-based solar cells dominate the market due to their maturity and long-term reliability, their high fabrication costs and rigid processing requirements highlight the necessity of exploring alternative materials.[3] In recent years, halide perovskite solar cells (PSCs) have revolutionized the field of photovoltaics, achieving remarkable power conversion efficiencies (PCEs) through cost-effective solution

[a]*Department of Material Science and Engineering, Khulna University of Engineering & Technology (KUET), Khulna 9203, Bangladesh*
[b]*Imam Mohammad Ibn Saud Islamic University (IMSIU), Riyadh 11432, Saudi Arabia*
[c]*Department of Electrical and Electronic Engineering, Begum Rokeya University, Rangpur, 5400, Bangladesh. E-mail: azizurrahmanatik49@gmail.com*
[d]*Department of Electrical and Electronic Engineering, Bangladesh Army University of Science and Technology (BAUST), Saidpur 5311, Bangladesh*
[e]*Applied College at Mohayel Assir, King Khalid University, Abha 61413, Saudi Arabia*
[f]*Department of Physics, Faculty of Science, Islamic University of Madinah, Al Jamiah, Madinah, 42351, Saudi Arabia*
[g]*Chemical Engineering Department, College of Engineering, University of Ha'il, P. O. Box 2440, 81441, Ha'il, Saudi Arabia*
[h]*Department of Physics, College of Science, King Khalid University, POST BOX 960, Abha, AlQura'a 61421, Saudi Arabia*

processing and outstanding optoelectronic properties.[4,5] However, the toxicity and environmental instability of Pb-based perovskites remain significant obstacles to their commercialization, thereby motivating the search for sustainable, lead-free alternatives.[6] Vacancy-ordered double perovskites (A_2BX_6) are derived from the ABX_3 structure by removing half of the B-site cations, forming isolated BX_6 octahedra surrounded by A-site cations (*e.g.*, Ga^+, In^+, Tl^+) and halides (Cl^-, Br^-).[7] This structural modification enhances stability and makes them promising lead-free alternatives for optoelectronic and energy applications. Depending on the B-site cation (*e.g.*, Ce^{4+}), they exhibit strong optical absorption, indirect-to-direct band gaps, and low thermal conductivity, supporting applications in solar cells, LEDs, radiation detectors, and thermoelectric.[8,9]

Previous studies have provided important insights into related systems. For example, A. Jabar *et al.* investigated Cs_2CeCl_6 using LSDA + mBJ in Wien2k, reporting a semiconducting bandgap of ~1.828 eV along with its optical and thermoelectric behavior, though photovoltaic device-level performance was not assessed.[10] Earlier, Kaatz and Marcovich (in the year of 1966) established that Cs_2CeCl_6 crystallizes in a cubic K_2PtCl_6-type structure (*Pm*3*m*), where Ce^{4+} is octahedrally coordinated by Cl^- ions and Cs^+ is twelve-fold coordinated, offering a useful structural reference for related Ce-based halide perovskites.[11] Meanwhile, hybrid organic–inorganic Pb-halide perovskites have achieved record PCEs of up to 25.5%,[12] but their deployment is hampered by inherent toxicity and poor environmental durability. Building on these motivations, we turned our attention to Ce-based vacancy-ordered double perovskites D_2CeX_6 (D = Ga, In, Tl; X = Cl, Br). Similar investigations, such as that of Redi Kristian Pingak *et al.*, confirmed the structural stability and semiconducting behavior of Tl_2SnCl_6 and Tl_2SnBr_6, with Tl_2SnBr_6 (1.48 eV) identified as a promising absorber due to its strong visible-light response.[13] Beyond photovoltaics, Ce-based oxides and halides demonstrate intriguing functionalities. Mehwish K. Butt *et al.* reported ferromagnetic half-metallicity in $CeAlO_3$ arising from Ce-4f states, suggesting potential in spintronic and optical applications.[14] Likewise, Mariya Zhuravleva *et al.* showed that Ce-halides such as Cs_3CeCl_6, Cs_3CeBr_6, $CsCe_2Cl_7$, and $CsCe_2Br_7$ exhibit high light yields and fast decay times, underlining their promise as scintillators for radiation detection.[15] Recent studies have shown that vacancy-ordered $CsRbGeCl_6$ and $CsRbGeBr_6$ possess direct band gaps of 2.60 eV and 1.78 eV, respectively, at the Γ-point, making them highly effective for light absorption across the visible to UV spectrum. Their excellent structural stability, non-toxic composition, and favorable electronic properties make these materials promising candidates for photovoltaic and other optoelectronic applications.[16] Similarly, Rb_2GeCl_6 and Rb_2GeBr_6 have been identified as lead-free alternatives with direct band gaps, mechanical robustness, and thermodynamic stability, making them suitable for renewable energy applications.[17] Further, N. V. Skorodumova *et al.* demonstrated that Ce-4f states in CeO_2 and Ce_2O_3 play decisive roles in governing electronic structure and bonding.[18] Tianyu Tang *et al.* reported that vacancy-ordered double halide perovskites A_2BX_6 (A = In, Tl; B = Pd, Pt; X = Cl, Br, I) are structurally stable semiconductors with tunable band gaps, strong UV-IR absorption, and potential applications as solar absorbers (Tl_2PdBr_6) or transparent conductors (In_2PtCl_6, Tl_2PtCl_6), yet their device-level performance and practical applicability remain unexplored.[19]

Additionally, vacancy-ordered halide perovskites A_2BX_6 (A = In, Tl; B = Pd, Pt; X = Cl, Br, I) offer extensive tunability of their band gaps (from 0.328 eV to 3.238 eV in HSE functional) and exhibit pronounced optical responses across the visible to infrared spectrum. Compounds such as Tl_2PdBr_6 and In_2PtCl_6 are emerging as leading candidates for solar absorber layers and transparent conductors, respectively, owing to their superior absorption coefficients and direct or quasi-direct band structures.[20–22] Similarly, Showkat Hassan Mir *et al.* investigated Cerium-based double perovskites A_2CeX_6 (A = Cs, K; X = Cl, Br) and found them to be structurally stable, non-magnetic semiconductors with direct band gaps, anisotropic mechanical and electronic properties, and strong visible-light absorption.[23] Taken together, these studies suggest that incorporating Ce into vacancy-ordered double perovskites can yield a rich interplay of structural stability, optical absorption, and electronic diversity.

The present investigation focuses on the performance analysis of D_2CeX_6 (D = Ga, In, Tl; X = Cl, Br) double perovskite compounds, carried out through a combination of first-principles calculations within the CASTEP framework and SCAPS-1D device simulations. The study comprehensively examines their structural, electronic, optical, thermoelectric, and mechanical properties, phonon stability, molecular dynamics, which are critical for energy-harvesting and photovoltaic applications. Structural stability was confirmed under cubic symmetry and mechanical deformation, ensuring robustness for practical implementation. Among the investigated compounds, bromide-based perovskites, particularly Ga_2CeBr_6 and Tl_2CeBr_6, demonstrated superior optoelectronic performance, characterized by optimal band gaps, high absorption coefficients, and strong dielectric responses, while In_2CeBr_6 exhibited notable mechanical robustness and ductility. To the best of current knowledge, no prior theoretical or experimental study has systematically explored the D_2CeX_6 family in this context. The findings establish Ce-based halide double perovskites as promising lead-free alternatives to toxic Pb-based materials, offering a well-balanced combination of efficiency, stability, and sustainability for next-generation photovoltaic and advanced power-generation technologies.

2 Computational method

2.1. Density functional theory (DFT)

We employed Density Functional Theory (DFT) within the CASTEP package to systematically investigate the XRD, structural, electronic, mechanical, optical properties, population analysis, and phonon properties of D_2CeX_6 (D = Ga, In, Tl; X = Cl, Br) double perovskites.[24–27] This *ab initio* approach is widely recognized for its reliability in describing the physicochemical characteristics of crystalline materials. Ultra-soft Vanderbilt-type pseudopotentials[28] were employed for Ga, In, Tl, Ce, Cl, and Br atoms to describe the electron-ion interactions while

maintaining computational accuracy efficiently.[29,30] A plane-wave cut-off energy of 700 eV was adopted to ensure precise representation of the electronic states and reliable energy convergence. The Brillouin zone was sampled using a Monkhorst–Pack *k*-point[31] grid of 8 × 8 × 8 for all compounds, guaranteeing consistent convergence of total energy, forces, and stress tensors across reciprocal space.[32] Geometry optimizations were performed under stringent convergence criteria, with thresholds set to 1.0×10^{-6} eV per atom for total energy, 0.006 eV $Å^{-1}$ for maximum force, 2.0×10^{-4} Å for maximum atomic displacement, and 0.02 GPa for maximum stress. The generalized gradient approximation with the Perdew–Burke–Ernzerhof (GGA–PBE) functional was mainly employed, as it ensures a reasonable compromise between accuracy and computational efficiency.[33,34] In contrast, the Heyd–Scuseria–Ernzerhof (HSE06) hybrid functional, though more accurate,[35] is highly time-consuming; thus, GGA–PBE was chosen as the primary functional, with HSE06 selectively applied to validate key geometry optimizations and electronic results. Calculations of the density of states (DOS), optical properties, X-ray diffraction (XRD) patterns, elastic constants, mechanical parameters, anisotropy index, and population analysis were performed within the GGA–PBE framework. The crystal structures of the compounds were modeled and visualized using VESTA software.[36] Mechanical properties and elastic constants were analyzed through the Voigt–Reuss–Hill approximation, while Poisson's ratio, shear modulus, and Young's modulus for both 2D and 3D anisotropic structures were obtained using Python-based tools. Furthermore, to investigate the thermodynamic stability and dynamic behavior of the system, molecular dynamics simulations were carried out in the NPT ensemble at 298 K using a timestep of 1.0 fs, with the production run extended to 50 ps after equilibration.[37]

2.2. SCAPS-1D-based performance assessment for solar cell

The photovoltaic performance of D_2CeX_6-based solar cell devices was simulated using SCAPS-1D software (Version 3.3.09),[38] while the corresponding device architecture was designed with Adobe Illustrator (Version 2020). In this study, the SCAPS-1D-based performance evaluation of D_2CeX_6 double perovskites was carried out by numerically solving the fundamental semiconductor equations that describe charge carrier generation, distribution, and transport within the device.[39] These include the Poisson equation,

$$\frac{\partial^2 \varphi}{\partial x^2} = \frac{q}{\varepsilon}(n(x) - p(x) + N_A(x) - N_D(x) - p_t(x) - N_t(x)) \quad (1)$$

which describes the potential distribution, the continuity equations for holes and electrons,[40]

$$\frac{\partial j_p}{\partial_x} = -q\left(R_p - G_p + \frac{\partial_p}{\partial_t}\right) \quad (2)$$

$$\frac{\partial j_n}{\partial_x} = q\left(R_n - G_n + \frac{\partial_n}{\partial_t}\right) \quad (3)$$

Drift-diffusion current equations,

$$J_p = -qD_p\frac{\partial p}{\partial x} + q\mu_p p\frac{\partial \varphi}{\partial x} \quad (4)$$

$$J_n = qD_n\frac{\partial n}{\partial x} + q\mu_n n\frac{\partial \varphi}{\partial x} \quad (5)$$

Here, ε is the dielectric constant, n and p are carrier concentrations, N and N_A are donor and acceptor densities, D p/n are diffusion coefficients, and μ p/n are carrier mobilities. The program calculates key performance parameters such as open-circuit voltage (V_{OC}),

$$V_{OC} = \frac{n \times k \times T}{q}\ln\left(\frac{I_{ph}}{I_O} + 1\right) \quad (6)$$

Short-circuit current density (J_{SC}),

$$J_{SC} = q \times A \times G \times \eta \quad (7)$$

Fill factor (FF),

$$FF = \frac{P_{Max}}{P_{in}} = \frac{I_{Max} \times V_{Max}}{V_{OC} \times I_{SC}} \quad (8)$$

Power conversion efficiency (PCE),

$$PCE = \frac{I_{SC} \times FF \times V_{OC}}{P_{in}} \quad (9)$$

where P_{in} is the incident solar power, n is the diode ideality factor, and k is Boltzmann's constant,[41] T is temperature, I_{ph} is the photo-generated current, I_0 is the reverse saturation current, A is the active area, G is the irradiance, and η is the quantum efficiency. By incorporating experimentally or theoretically derived material properties, including band gap, electron affinity, relative permittivity, and carrier mobility into these equations, SCAPS-1D enables the evaluation of recombination mechanisms, carrier transport, and defect tolerance. This facilitates the identification of optimal halide (Cl, Br) and D-site cation (Ga, In, Tl) combinations with balanced optoelectronic properties, reduced recombination losses, and enhanced efficiency, thus offering a cost-effective and accurate approach to designing high-efficiency, lead-free double perovskite solar cells before fabrication. These device-level simulations were complemented by first-principles calculations, which provided detailed insights into the structural, electronic, optical, mechanical, phonon, and population properties of vacancy-ordered D_2CeX_6 perovskites. The integration of DFT analyses with SCAPS-1D simulations delivers a comprehensive evaluation of the material's potential in optoelectronic and photovoltaic applications, offering valuable guidance for the development of lead-free vacancy-ordered perovskite solar cells.

3 Results and discussion

3.1. X-ray diffraction (XRD) analysis

X-ray diffraction (XRD) is a fundamental characterization technique used to determine the crystal structure, phase purity, and lattice parameters of materials by measuring the angles and

intensities of diffracted X-rays.[42] This analysis is essential as it enables precise identification of crystalline phases, detection of structural distortions, estimation of unit cell dimensions, and confirmation of material synthesis without destructive testing. For perovskites, XRD provides critical insights into how atomic arrangements vary with different cations or anions, reveals lattice strain and defects, and helps explain changes in electronic, optical, and mechanical properties.[43] Such structural information is indispensable for correlating crystal geometry with performance in photovoltaics, optoelectronics, and thermoelectric, thereby ensuring consistency between theoretical predictions and experimental results in optimized device design.[44] The X-ray diffraction (XRD) patterns of vacancy-ordered halide perovskites D_2CeX_6 (D = Ga, In, Tl; X = Cl, Br) reveal sharp and intense peaks, confirming their high crystallinity and phase purity. The measured 2θ values show that Ga_2CeCl_6 has its first diffraction peak at 13.2° and the last prominent peak at 44.05°, while Ga_2CeBr_6 ranges from 12.7° to 42.3°, as shown in Fig. 1(a). Similarly, In_2CeCl_6 spans from 13.2° to 44.05°, and In_2CeBr_6 from 12.7° to 42.3°, as shown in Fig. 1(b). Tl_2CeCl_6 exhibits a slightly higher starting angle of 13.3° and extends to 44.4°, whereas Tl_2CeBr_6 lies between 12.7° and 42.6°, as shown in Fig. 1(c). The consistent observation that bromide-based compounds have their diffraction peaks shifted toward lower angles compared to chlorides indicates lattice expansion, attributable to the larger ionic radius of Br^-, which increases the interplanar spacing (d-spacing) according to Bragg's law.[45] Differences among Ga, In, and Tl compositions, particularly at both lowest and highest 2θ positions, reflect the influence of A-site cation size, mass, and bonding characteristics on unit cell parameters. This variation in lattice dimensions directly impacts electronic band structure, phonon dynamics, and defect formation tendencies, which are crucial for optoelectronic and thermoelectric applications. The importance of XRD here lies not only in confirming the successful synthesis of the targeted phase but also in quantitatively linking structural

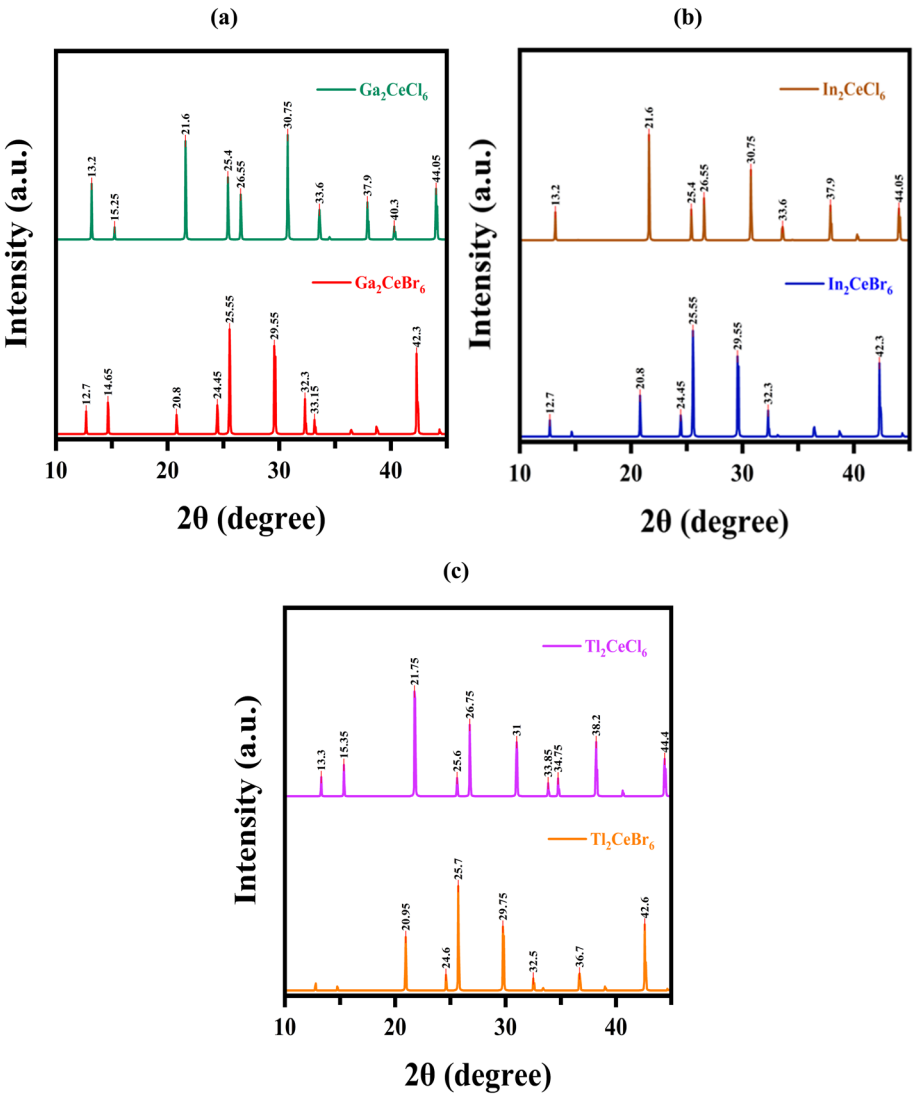

Fig. 1 X-ray diffraction (XRD) patterns of (a) Ga_2CeCl_6 and Ga_2CeBr_6, (b) In_2CeCl_6 and In_2CeBr_6, (c) Tl_2CeCl_6 and Tl_2CeBr_6 vacancy-ordered perovskites.

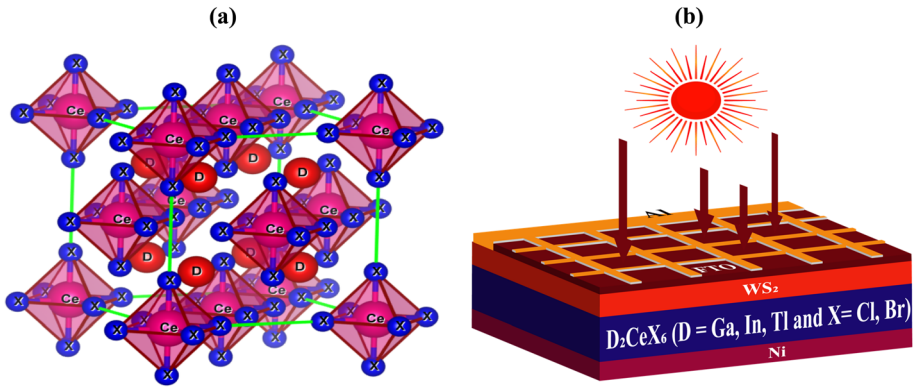

Fig. 2 The (a) crystal structure, (b) proposed solar cell device structure of D_2CeX_6 vacancy-ordered perovskites.

parameters to physical properties, thereby enabling predictive modeling in density functional theory (DFT) simulations and guiding experimental optimization for photovoltaic device integration.

3.2. Structural characteristics of vacancy-ordered perovskites

The D_2CeX_6 (D = Ga, In, Tl; X = Cl, Br) double perovskites adopt a highly symmetric cubic crystal structure, typically belonging to the space group $Fm\bar{3}m$ (#225).[46] Within this framework, the Ce^{4+} cations occupy the octahedral coordination sites, where each Ce atom is surrounded by six halide ions (Cl^- or Br^-), forming corner-sharing CeX_6 octahedra that serve as the fundamental building blocks of the lattice. The D-site cations (Ga, In, Tl) are accommodated in the interstitial cavities, stabilizing the perovskite structure through electrostatic interactions. In terms of crystallographic positions, the D-site atoms reside at the face-centered Wyckoff position 3c (0, 0.5, 0.5), the Ce atom is located at the corner site with Wyckoff position 1a (0, 0, 0), and the halide atoms occupy the body-centered Wyckoff position 1b (0.5, 0.5, 0.5).

This ordered arrangement reflects the vacancy-ordered nature of the perovskite, where one of the B-site cations in the conventional ABX_3 lattice is replaced by a structural vacancy, giving rise to the distinctive A_2BX_6 stoichiometry. As illustrated in Fig. 2(a), the atomic configurations of analogous compounds such as Ga_2CeCl_6, Ga_2CeBr_6, In_2CeCl_6, In_2CeBr_6, Tl_2CeCl_6, and Tl_2CeBr_6 display a similar cubic symmetry and site occupancy pattern, highlighting the robustness of this structural motif across different compositions. The high degree of symmetry and well-defined cation coordination in these materials play a crucial role in determining their electronic structure, phonon dynamics, and defect tolerance properties that are directly linked to their optoelectronic and photovoltaic performance.

The optimized lattice constants of these vacancy-ordered perovskites are 7.071 Å to 7.784 Å, as shown in Table 1, primarily governed by the ionic radii of both the D-site cations and halide anions. Predictably, substitution of Cl^- with the larger Br^- ion results in a noticeable increase in lattice parameters. For instance, Ga_2CeCl_6 possesses a lattice constant of 7.410 Å, which expands to 7.784 Å for Ga_2CeBr_6. A similar lattice expansion trend is observed for the In- and Tl-based systems. The corresponding unit cell volumes reflect this trend, increasing with the incorporation of the larger halide anion. The highest unit cell volume of 333.524 $Å^3$ is recorded for Ga_2CeBr_6, while In_2CeBr_6 and Tl_2CeBr_6 both display volumes of 249.999 $Å^3$, indicating a consistent cubic framework for these bromide compounds. Furthermore, the calculated volumes obtained using GGA–PBE and HSE06 functionals show

Table 1 The energy band gap, lattice constants, unit cell volume, density, and formation energy of D_2CeX_6 vacancy-ordered perovskites

		GGA–PBE				HSE-06		
Ref.	Compounds	Energy band gap, eV	Lattice constant a^0 (Å)	Unit cell volume, V ($Å^3$)	Density, g cm^{-3}	Energy band gap, eV	Unit cell volume, V ($Å^3$)	Formation energy, ΔE_f (eV per atom)
This work	Ga_2CeCl_6	1.733	7.410	287.748	2.841	1.776	287.775	−3.597
	Ga_2CeBr_6	1.276	7.784	333.524	3.778	2.843	333.528	−3.227
	In_2CeCl_6	1.555	7.473	295.156	3.277	2.261	249.999	−3.571
	In_2CeBr_6	0.859	7.071	249.999	5.640	2.170	249.999	−3.064
	Tl_2CeCl_6	1.755	7.503	298.718	4.233	3.632	298.732	−3.699
	Tl_2CeBr_6	1.364	7.071	249.999	6.830	1.418	249.999	−3.178
48	K_2CeCl_6	1.742	7.522	300.945	2.378	—	—	−3.714
	Rb_2CeCl_6	1.748	7.619	312.774	2.780	—	—	−3.720
	Cs_2CeCl_6	1.807	7.863	343.881	2.987	—	—	−3.746
	Fr_2CeCl_6	1.830	8.111	377.413	3.514	—	—	−3.705

negligible differences, indicating reliable structural optimization. Notably, the calculated densities are 2.841 g cm^{-3} for Ga_2CeCl_6, 3.277 g cm^{-3} for In_2CeCl_6, and 4.233 g cm^{-3} for Tl_2CeCl_6, while Ga_2CeBr_6, In_2CeBr_6, and Tl_2CeBr_6 exhibit 3.778, 5.640, and 6.830 g cm^{-3}, respectively. These variations clearly demonstrate that both the nature of the D_2-site cation (Ga, In, Tl) and the X_6 anion (Cl, Br) strongly influence the structural packing and overall density, with heavier Tl and Br substitutions yielding denser frameworks. In addition to structural analysis, the electronic band gaps were calculated using both GGA–PBE and HSE06 functionals (Table 1). As anticipated, the HSE06 hybrid functional produced consistently higher band gaps owing to its more accurate treatment of exchange–correlation effects. For instance, Ga_2CeCl_6 exhibited an increase from 1.733 eV (GGA–PBE) to 1.776 eV (HSE06), with similar enhancements observed across all compounds. The bromide analogues displayed the lowest gaps, with In_2CeBr_6 showing the smallest values of 0.859 eV (GGA–PBE) and 2.170 eV (HSE06), consistent with the established trend of band gap narrowing as the halide ionic radius increases.

To further evaluate the thermodynamic stability of these perovskites, their formation energy (ΔE_f) was computed,[47] as in Table 1.

$$\Delta E_f = E_{tot}(A_2CeX_6) - 2E(A) - E(Ce) - 6E(X) \quad (10)$$

Negative formation energy indicates that a compound is thermodynamically stable and can form spontaneously, with more negative values reflecting stronger bonding and greater intrinsic stability. It's a key factor in assessing whether a material is synthesizable and suitable for applications like photovoltaics or catalysis. All compounds exhibit negative formation energy, confirming their thermodynamic favorability. Tl_2CeCl_6 displayed the most negative formation energy value of −3.699 eV per atom, indicating it as the most stable composition among the series. In contrast, Ga_2CeBr_6 showed the least negative value (−3.227 eV per atom), likely due to the combined effect of the lighter Ga cation and the larger, less tightly bound Br^- anion.

The calculated structural and electronic properties of Ga_2CeX_6, In_2CeX_6, and Tl_2CeX_6 (X = Cl, Br) exhibit close similarities with the reported results of K_2CeCl_6, Rb_2CeCl_6, Cs_2CeCl_6, and Fr_2CeCl_6. In both cases, the GGA–PBE predicted band gaps are within the same semiconducting range. At the same time, the lattice constants and unit cell volumes follow a systematic increase with the incorporation of larger A-site cations. Furthermore, the negative formation enthalpies obtained in this work are comparable to those in ref. 48, confirming the thermodynamic stability of these Ce-based halide double perovskites.

3.2.1. Bond length variation analysis. The variation of bond lengths within D_2CeX_6 (D = Ga, In, Tl; X = Cl, Br) is important because it provides key insights into the structural stability, electronic interactions, and overall behavior of these vacancy-ordered double perovskites. Shorter Ce–X bonds indicate strong Ce-halide interactions, which help stabilize the crystal lattice, while variations in D–X and Ce–D distances reflect the influence of different cations and halides on the lattice geometry. These bond lengths directly affect orbital overlap, band structure, and optoelectronic properties, making them critical for accurately predicting electronic, optical, and mechanical behavior through computational methods. Overall, analyzing bond length variations connects atomic-scale geometry with material performance, providing a foundation for understanding and optimizing D_2CeX_6 compounds for applications such as solar cells and other optoelectronic devices.

Table 2 presents the bond length variations in D_2CeX_6 (D = Ga, In, Tl; X = Cl, Br), considering D–X, Ce–X, and Ce–D interactions. The D–X bonds range from 3.705 to 3.892 Å, with chlorides showing slightly shorter values (3.705 to 3.751 Å) than bromides, except for In_2CeBr_6 and Tl_2CeBr_6, where the D–X length decreases to 3.540 Å. The Ce–X bonds are consistently shorter (2.626 to 2.785 Å), indicating stronger Ce–X interactions compared to D–X; as expected, Ce–Br bonds (≈2.682 to 2.785 Å) are longer than Ce–Cl bonds (≈2.626 to 2.631 Å) owing to the larger ionic radius of Br^-. The Ce–D bonds are the longest, ranging between 4.330 and 4.766 Å, with the maximum in Ga_2CeBr_6 and the minimum in In_2CeBr_6 and Tl_2CeBr_6. These variations reveal that the bond lengths are sensitive to both the halide ion and the D-site cation, where bromides generally favor longer separations than chlorides, and the shorter Ce–X bonds suggest stronger Ce-centered bonding, which may play a decisive role in stabilizing the crystal structure and influencing the electronic interactions within these vacancy-ordered double perovskites.

3.2.2. Geometric stability parameters. For vacancy-ordered perovskite structures, the stability and structural distortion are often evaluated using the Goldschmidt tolerance factor (t) and the octahedral factor (μ). It is defined as:

$$t = \frac{(r_A + r_X)}{\sqrt{2}(r_{Ce} + r_X)} \quad (11)$$

$$\mu = \frac{r_B}{r_X} \quad (12)$$

The tolerance factor generally falls within the range of 0.8 to 1.0, where values close to 1.0 represent an ideal cubic configuration with minimal lattice distortion. Meanwhile, the octahedral factor typically lies between 0.41 and 0.90, indicating that the B-site cation is appropriately sized to fit within the BX_6

Table 2 The variation of bond length within the atom of D_2CeX_6 (where D = Ga, In, Tl, and X = Cl, Br)

	Bond length, L (Å)		
Compounds	L_{D-X}	L_{Ce-X}	L_{Ce-D}
Ga_2CeCl_6	3.705	2.626	4.538
Ga_2CeBr_6	3.892	2.785	4.766
In_2CeCl_6	3.736	2.629	4.576
In_2CeBr_6	3.540	2.682	4.330
Tl_2CeCl_6	3.751	2.631	4.594
Tl_2CeBr_6	3.540	2.682	4.330

Table 3 Tolerance factor and octahedral factors variation in D_2CeX_6 vacancy-ordered perovskites

Materials	r_A	r_{Ce}	r_X	Tolerance factor (t)	Octahedral factor (μ)
Ga_2CeCl_6	1.3	0.97	1.81	0.791	0.5359
Ga_2CeBr_6	1.3	0.97	1.96	0.7867	0.4949
In_2CeCl_6	1.44	0.97	1.81	0.8267	0.5359
In_2CeBr_6	1.44	0.97	1.96	0.8205	0.4949
Tl_2CeCl_6	1.59	0.97	1.81	0.8648	0.5359
Tl_2CeBr_6	1.59	0.97	1.96	0.8567	0.4949

octahedron.[49,50] When both factors fall within these ranges, the perovskite framework achieves a balanced geometric arrangement, leading to enhanced structural stability. Deviations outside these limits may result in lattice distortions, octahedral tilting, or complete structural instability, highlighting the critical role of ionic size matching in the design of stable vacancy-ordered perovskites.

The calculated tolerance factors, as summarized in Table 2, are 0.7867, 0.7867, 0.8267, 0.8205, 0.8648, and 0.8567 for Ga_2CeCl_6, Ga_2CeBr_6, In_2CeCl_6, In_2CeBr_6, Tl_2CeCl_6, and Tl_2CeBr_6, respectively. All compounds exhibit values within the structural stability range, except Ga_2CeCl_6 and Ga_2CeBr_6, which fall slightly below the lower limit but remain close to the stability threshold. This indicates that most of these halide double perovskites possess geometrically favorable ionic packing. At the same time, the Ga-based variants, though marginally less ideal, are still likely to form stable frameworks with only minor octahedral tilting or distortion. The calculated octahedral factors, presented in Table 3, are 0.5359, 0.4949, 0.5359, 0.4949, 0.5359, and 0.4949 for Ga_2CeCl_6, Ga_2CeBr_6, In_2CeCl_6, In_2CeBr_6, Tl_2CeCl_6, and Tl_2CeBr_6, respectively. All values fall within the established structural stability window (0.41 to 0.90), confirming that the B-site cations are appropriately accommodated within the BX_6 octahedral framework. This suggests that these compounds are geometrically favorable for forming stable vacancy-ordered perovskite structures.

3.3. Electronic properties

The electronic properties of materials refer to how electrons behave within a solid, influencing key characteristics like

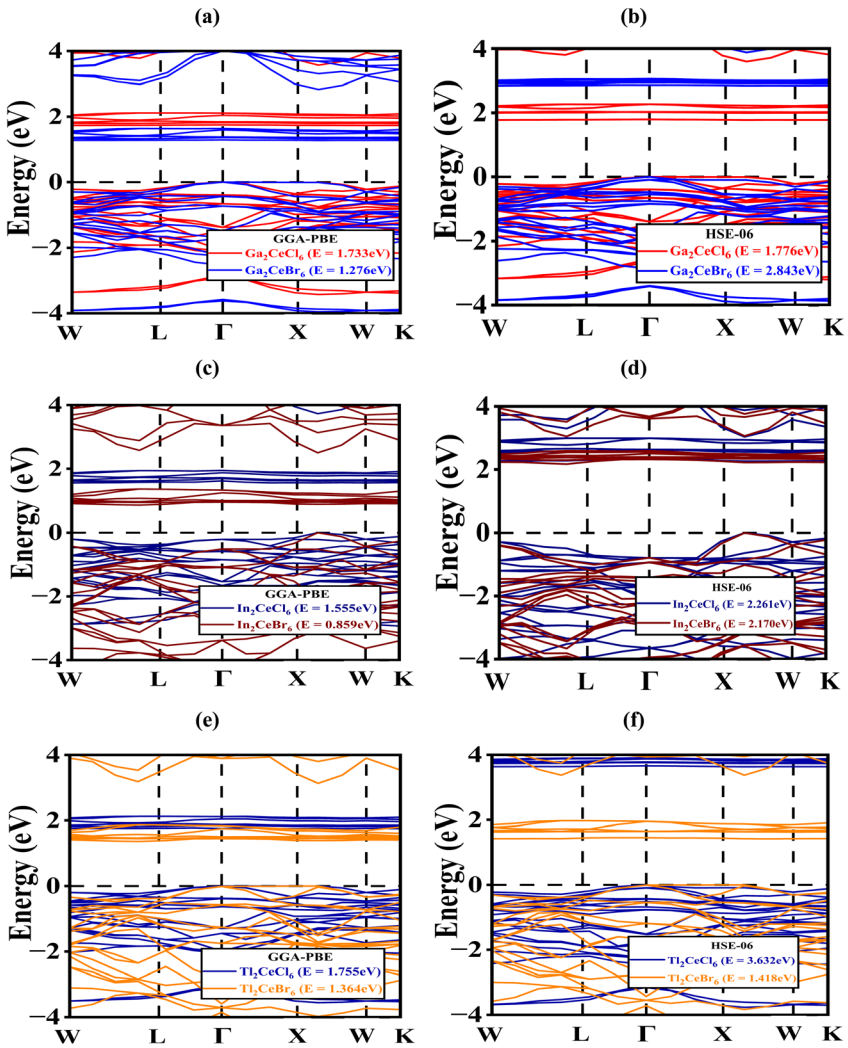

Fig. 3 Energy band gap of (a and b) Ga_2CeX_6, (c and d) In_2CeX_6 and (e and f) Tl_2CeX_6 double perovskite materials using GGA–PBE and HSE06 function.

electrical conductivity, resistivity, carrier mobility, band structure, and band gap.[51,52] These parameters determine whether a material behaves as a metal, semiconductor, or insulator and directly influence its suitability for electronic, optoelectronic, and energy-related applications. By analyzing electronic features, particularly the band structure, band gap nature (direct or indirect), and partial density of states, researchers can assess whether a specific D_2CeX_6 compound is more appropriate for light-emitting applications, such as LEDs, or for light-harvesting and charge-separating functions, such as photovoltaics. The band structure, a cornerstone of solid-state physics, illustrates the variation of electron energy with momentum in a crystalline material.[53] For vacancy-ordered double perovskites D_2CeX_6, knowledge of the band dispersion and gap is essential, as these parameters dictate their electronic and optoelectronic performance, influencing applications in solar cells. Fig. 3 presents the calculated band structures using two computational approaches, GGA–PBE (Fig. 3(a, c and e)) and HSE06 (Fig. 3(b, d and f)), where the energy (E–E_X, in eV) is plotted along high-symmetry Brillouin zone paths (W–L–Γ–X–W–K), with the Fermi level fixed at 0 eV.

The band gap forms between the valence-band maximum (VBM) and conduction-band minimum (CBM). As shown in Fig. 3(a–f), DFT reveals a clear dependence on both the D-site cation (D = Ga, In, Tl) and halide (X = Cl, Br). In Fig. 3(a, c and e), within GGA–PBE, the calculated gaps are: Ga_2CeCl_6 of 1.733 eV, Ga_2CeBr_6 of 1.276 eV, In_2CeCl_6 of 1.555 eV, In_2CeBr_6 of 0.859 eV, Tl_2CeCl_6 of 1.755 eV, and Tl_2CeBr_6 of 1.364 eV, placing all but In_2CeBr_6 (too narrow) within or near the 1.1 to 1.8 eV single-junction "sweet spot." A clear anion dependence is observed: replacing Cl with Br consistently reduces the band gap due to the higher energy of Br-4p orbitals, which raises the

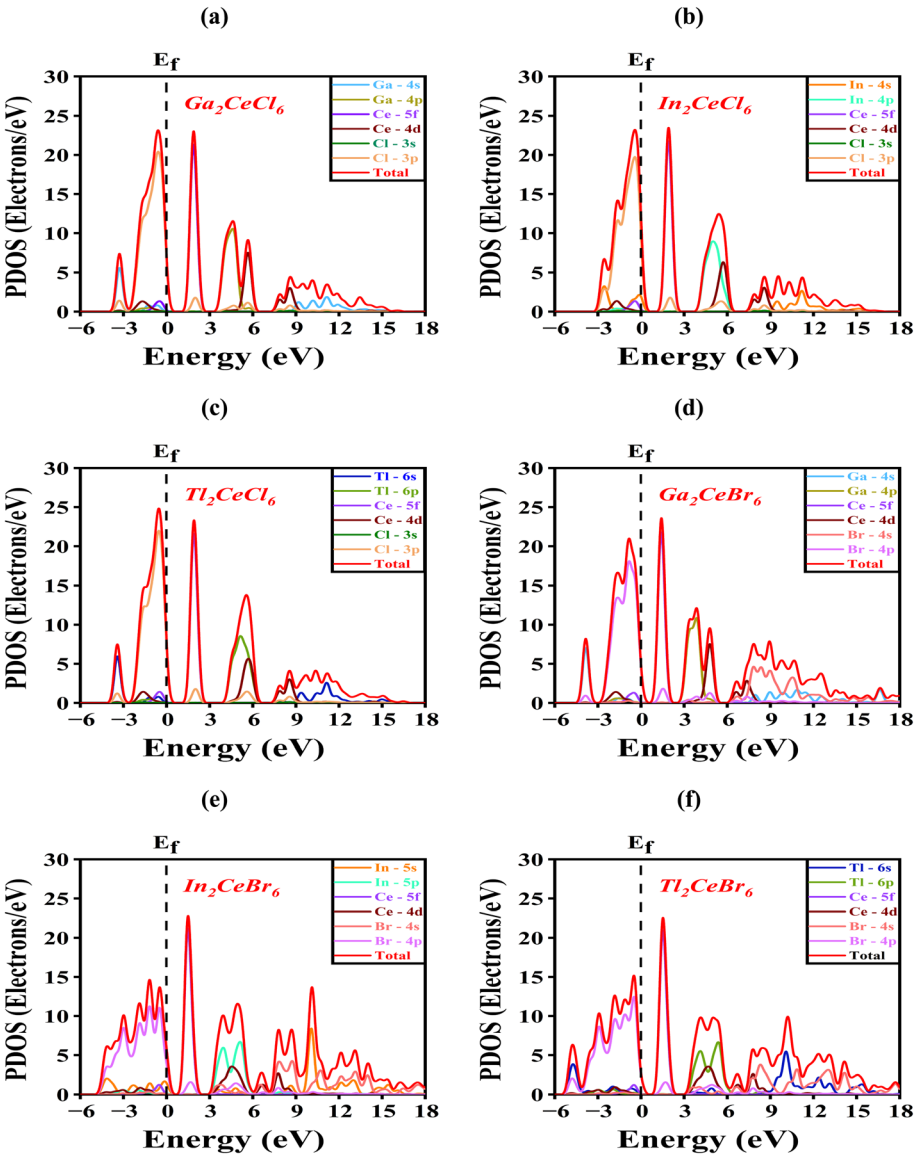

Fig. 4 The partial density of states of (a) Ga_2CeCl_6, (b) Ga_2CeBr_6, (c) In_2CeCl_6, (d) In_2CeBr_6, (e) Tl_2CeCl_6, and (f) Tl_2CeBr_6 vacancy-ordered double perovskites.

VBM and narrows the gap. As expected, HSE06 increases the gaps because of its improved treatment of exchange: Ga_2CeCl_6 of 1.776 eV, Ga_2CeBr_6 of 2.843 eV, In_2CeCl_6 of 2.261 eV, In_2CeBr_6 of 2.170 eV, Tl_2CeCl_6 of 3.632 eV, and Tl_2CeBr_6 of 1.418 eV, as shown in Fig. 3(b, d and f). Under HSE06, Tl_2CeBr_6 (1.418 eV) and Ga_2CeCl_6 (1.776 eV) remain suitable for single-junction devices, whereas the wider-gap Ga_2CeBr_6, In_2CeCl_6, In_2CeBr_6, and Tl_2CeCl_6 (>2.0 eV) are better suited as top cells in tandem architectures. In contrast, In_2CeBr_6 at the PBE level (0.859 eV) exemplifies the "narrow-gap" regime (<1.1 eV), which enhances IR absorption but suffers from higher thermalization losses.

The Partial Density of States (PDOS) is a powerful tool in materials science for identifying the orbital and atomic contributions to the electronic structure of compounds.[54] Such analysis provides key insights into the electronic behavior relevant for solar cells and light-emitting devices. For the D_2CeX_6 vacancy-ordered perovskites, the valence band (VB) extends from −6 to 0 eV, while the conduction band (CB) spans from 0 to +18 eV, as illustrated in Fig. 4. In the valence band region, the dominant contributions originate from halogen p-states hybridized with the D-site cation s-states: Cl-3p and Ga-4s in Ga_2CeCl_6 (Fig. 4(a)), Cl-3p and In-5s in In_2CeCl_6 (Fig. 4(b)), Cl-3p and Tl-6s in Tl_2CeCl_6 (Fig. 4(c)), Br-4p and Ga-4s in Ga_2CeBr_6 (Fig. 4(d)), Br-4p and In-5s in In_2CeBr_6 (Fig. 4(e)), and Br-4p and Tl-6s in Tl_2CeBr_6 (Fig. 4(f)). In all cases, Ce-4d states provide a minor but noticeable contribution to the VB. In the conduction band region, the primary states arise from Ce-5f orbitals, strongly mixed with the p-states of the D-site cations: Ce-5f and Ga-4p in Ga_2CeCl_6 (Fig. 4(a)), Ce-5f and In-5p in In_2CeCl_6 (Fig. 4(b)), Ce-5f and Tl-6p in Tl_2CeCl_6 (Fig. 4(c)), Ce-5f and Ga-4p in Ga_2CeBr_6 (Fig. 4(d)), Ce-5f and In-5p in In_2CeBr_6 (Fig. 4(e)), and Ce-5f and Tl-6p in Tl_2CeBr_6 (Fig. 4(f)).

Notably, localized peaks appear just above the Fermi level (E_X), confirming that the conduction-band minimum (CBM) is dominated by Ce-derived states. Overall, the PDOS indicates that the VBM is mainly governed by halogen p-states hybridized with D-site s-states, while the CBM is strongly influenced by Ce-5f states, a characteristic feature of these vacancy-ordered double perovskites. It is worth noting that a slight mismatch between the band gap values obtained from the band structure (Fig. 3) and the PDOS (Fig. 4) is observed. This minor deviation originates from the intrinsic limitations of DFT within the PBE framework, differences in *k*-point sampling, and the broadening applied in DOS plotting.[55] Nevertheless, all data have been carefully rechecked, and the overall electronic trends remain fully consistent, confirming the reliability of the presented results.

3.4. Homo–lumo analysis

HOMO–LUMO analysis investigates the energy difference between the Highest Occupied Molecular Orbital (HOMO) and the Lowest Unoccupied Molecular Orbital (LUMO), offering key insights into a material's chemical reactivity, stability, and electronic characteristics.[56,57] The HOMO corresponds to the molecule's ability to donate electrons, while the LUMO reflects its capacity to accept electrons. A smaller HOMO–LUMO energy gap signifies higher chemical reactivity, lower stability, and improved electrical conductivity, whereas a larger gap indicates greater stability and reduced reactivity. Thus, this analysis is fundamental for understanding charge transfer, optical transitions, and bandgap behavior in both molecular and solid-state systems, serving as an essential tool for designing materials with tailored electronic and optoelectronic properties.[58]

Table 4 Calculated HOMO–LUMO energies and electronic characteristics of D_2CeX_6 double perovskite compounds

Compounds	Type	*N*	s	Eigenvalue	Field
Ga_2CeCl_6	HOMO	111	+	−0.263252	Yes
	LUMO	112	+	−0.219414	Yes
Ga_2CeBr_6	HOMO	165	+	−0.244130	Yes
	LUMO	166	+	−0.212826	Yes
In_2CeCl_6	HOMO	129	+	−0.266703	Yes
	LUMO	130	+	−0.222910	Yes
In_2CeBr_6	HOMO	183	+	−0.227664	Yes
	LUMO	184	+	−0.185877	Yes
Tl_2CeCl_6	HOMO	161	+	−0.267885	Yes
	LUMO	162	+	−0.224097	Yes
Tl_2CeBr_6	HOMO	215	+	−0.229307	Yes
	LUMO	216	+	−0.186823	Yes

Table 4 presents the HOMO–LUMO energy values of six halide double perovskite compounds, namely Ga_2CeCl_6, Ga_2CeBr_6, In_2CeCl_6, In_2CeBr_6, Tl_2CeCl_6, and Tl_2CeBr_6, which help evaluate their electronic properties and chemical reactivity. The eigenvalues of both HOMO and LUMO orbitals are negative, indicating bound electronic states, while the difference between them represents the HOMO–LUMO energy gap (ΔE), which reflects the ease of electronic excitation. Among these, bromine-based compounds (Br_6) exhibit slightly smaller energy gaps than their chlorine-based counterparts (Cl_6), implying that Br-based systems are more reactive and less stable, with better potential for charge transfer and optical activity.

Conversely, Cl-based compounds show larger gaps, indicating greater chemical stability and lower electronic polarizability. Thus, the trend reveals that the HOMO–LUMO gap decreases in the order $Cl_6 > Br_6$, suggesting that substitution of Cl by Br enhances the electronic softness and conductivity of the materials, which is beneficial for optoelectronic and semiconductor applications.

Fig. 5 presents the spatial distributions of the HOMO and LUMO for Ga_2CeCl_6 and Ga_2CeBr_6 double perovskites, illustrating their electronic charge density and orbital hybridization characteristics. In both compounds, the HOMO states are primarily localized around the halogen atoms (Cl or Br) and partially extend toward the Ce atoms, indicating that the valence band maximum (VBM) mainly originates from the p-orbitals of the halogens with minor Ce contributions.

Conversely, the LUMO orbitals are more delocalized over the Ce and Ga atoms, suggesting that the conduction band minimum (CBM) is predominantly governed by Ce 4f and Ga 4s/4p orbitals. This behavior highlights a charge transfer from the halogen sites to the metal centers during electronic excitation. Comparatively, Ga_2CeCl_6 exhibits a more compact and

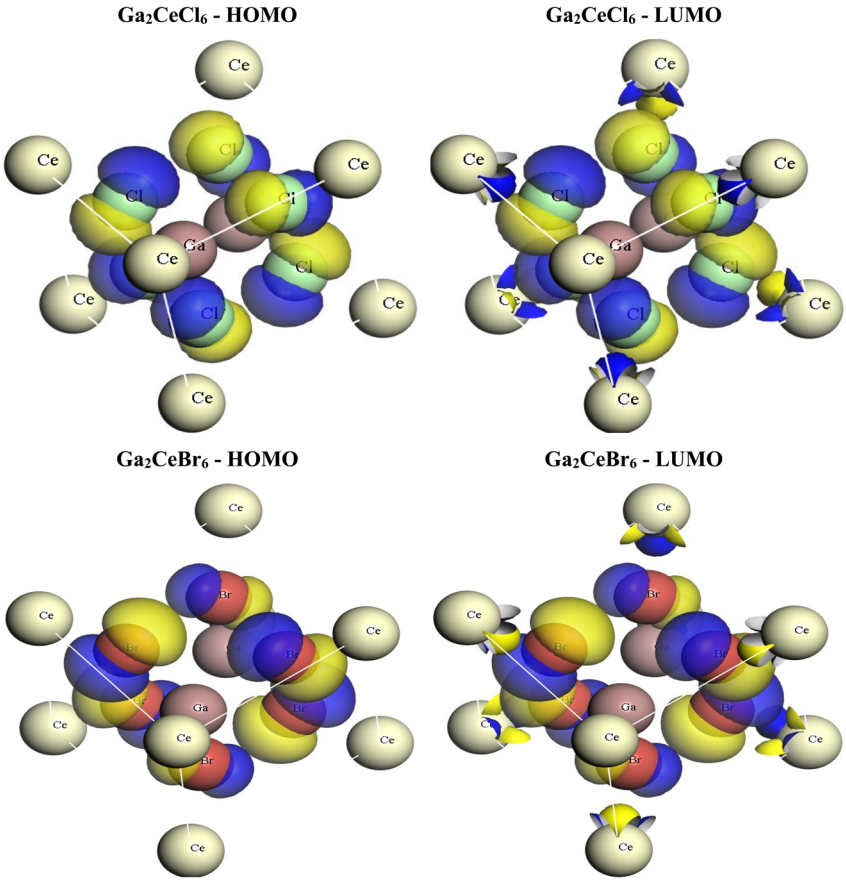

Fig. 5 HOMO and LUMO charge density distributions of Ga_2CeCl_6 and Ga_2CeBr_6 double perovskites.

symmetric orbital distribution owing to the smaller ionic radius and stronger bonding of Cl atoms, whereas Ga_2CeBr_6 shows broader and slightly distorted orbital features due to the weaker Ga–Br and Ce–Br interactions associated with the larger Br ions. Overall, both materials demonstrate a similar electronic transition pattern—from halogen-dominated HOMO to metal-centered LUMO—but Ga_2CeCl_6 displays stronger orbital overlap and higher electronic localization, resulting in a wider band gap and enhanced bonding strength. In contrast, Ga_2CeBr_6 exhibits narrower band gaps and improved charge transfer characteristics, making it potentially more favorable for optoelectronic applications.

Fig. 6 illustrates the HOMO and LUMO charge density distributions of In_2CeCl_6 and In_2CeBr_6 double perovskites, providing a detailed visualization of their electronic interactions, orbital hybridization, and charge transfer mechanisms. In both compounds, the HOMO orbitals are primarily localized around the halogen atoms (Cl or Br), with noticeable overlap extending toward the Ce atoms. This indicates that the VBM mainly originates from the halogen p-orbitals, slightly hybridized with Ce f-orbitals, suggesting a strong halogen–Ce bonding contribution in the occupied states. Conversely, the LUMO orbitals are predominantly distributed over the Ce and In atoms, revealing that the CBM is mainly derived from Ce 4f and In 5s/5p orbitals. This spatial separation between the HOMO and LUMO charge densities confirms a halogen-to-metal charge transfer (HMCT) mechanism during electronic excitation, a typical feature of Ce-based halide perovskites. Comparatively, In_2CeCl_6 exhibits more compact and symmetric charge density lobes around the Ce–Cl–In framework, indicating stronger covalent bonding and tighter electronic confinement. This results in a larger band gap and enhanced structural rigidity. The smaller ionic radius and higher electronegativity of Cl promote stronger orbital overlap and increased charge localization. In contrast, In_2CeBr_6 displays more extended and diffuse charge distributions around the Br atoms, reflecting weaker In–Br and Ce–Br interactions due to the larger atomic radius and lower electronegativity of Br. This delocalization facilitates higher electron mobility and reduces the band gap, making the bromide compound more suitable for optoelectronic and photovoltaic applications that demand efficient charge transport. Overall, while both In_2CeCl_6 and In_2CeBr_6 exhibit a similar electronic transition pattern (halogen $p \rightarrow$ Ce/In f/s), In_2CeCl_6 is characterized by stronger bonding and greater electronic localization—ideal for structural and electronic stability—whereas In_2CeBr_6 shows enhanced delocalization and charge transport properties, making it a promising candidate for devices requiring improved conductivity and light absorption efficiency.

Fig. 7 presents the spatial charge density distributions of the frontier molecular orbitals HOMO and LUMO for Tl_2CeCl_6 and Tl_2CeBr_6, offering crucial insight into their electronic behavior

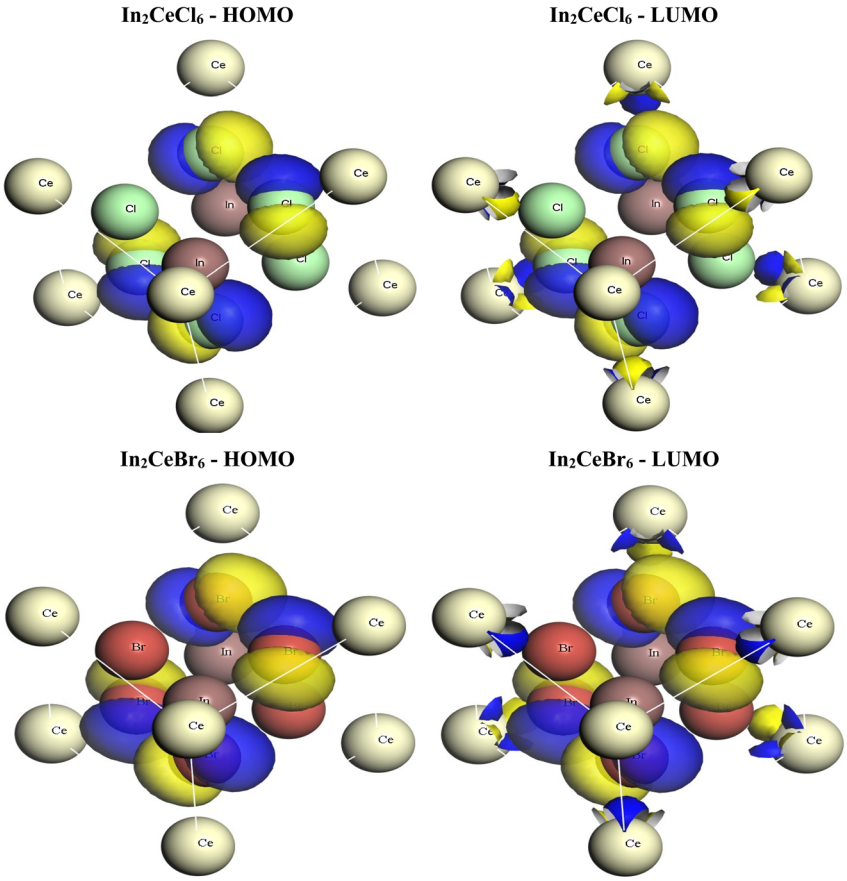

Fig. 6 HOMO and LUMO charge density distributions of In_2CeCl_6 and In_2CeBr_6 double perovskites.

and bonding nature. In Tl_2CeCl_6, the HOMO (top left) shows electron density predominantly concentrated around the Cl and Ce atoms, suggesting strong Cl-p and Ce-f orbital hybridization within the valence band. This localization near the halide atoms indicates that the valence band maximum (VBM) is largely halogen-derived, with only a minor contribution from Ce orbitals.

Conversely, in the LUMO (top right), the charge density becomes more delocalized toward Ce and Tl centers, signifying that the conduction band minimum (CBM) arises mainly from Ce-d and Tl-p orbitals. This spatial transition of electron density from halogen to metal centers across HOMO–LUMO levels highlight a characteristic charge-transfer excitation process within the Tl–Ce–Cl framework. For Tl_2CeBr_6 (bottom row), a similar orbital distribution pattern is observed, yet with notable differences in the extent and nature of charge delocalization. The HOMO charge density around Br and Ce atoms appears more diffused and extensive than in Tl_2CeCl_6, reflecting the larger size and lower electronegativity of Br compared to Cl. This results in weaker bonding and reduced orbital confinement, which can lower the band gap energy. In the LUMO of Tl_2CeBr_6, electron density remains focused on Ce and Tl sites but extends more toward the Br orbitals, implying enhanced orbital overlap and electronic coupling between the halide and metal centers. Overall, both compounds share similar electronic topologies, where the valence band is dominated by halide-Ce interactions and the conduction band by Ce–Tl hybridization. However, the Br-based compound exhibits greater orbital delocalization, smoother charge transitions, and stronger metal-halide interaction continuity, all of which contribute to narrower band gaps and potentially improved optical absorption and charge transport. These electronic distinctions underline the role of halide substitution in tuning the band-edge characteristics and optoelectronic performance of Tl–Ce halide perovskites.

3.5. Charge density mapping

Charge density mapping is a powerful technique that visualizes the distribution of electronic charge within a crystal lattice, providing direct insight into the nature of chemical bonding and electronic interactions between constituent atoms.[59,60] For D_2CeX_6 vacancy-ordered double perovskites, charge density analysis is particularly important as it reveals bonding characteristics, charge localization around different atomic sites, and potential pathways for defect formation, all of which critically influence their optical, electronic, and structural properties. Fig. 8 elucidates the charge density maps of D_2CeX_6 (D = Ga, In, Tl; X = Cl, Br) double perovskites, where electron localization is visualized using a color scale. In all compounds, significant charge accumulation is observed at the Ce sites and around the

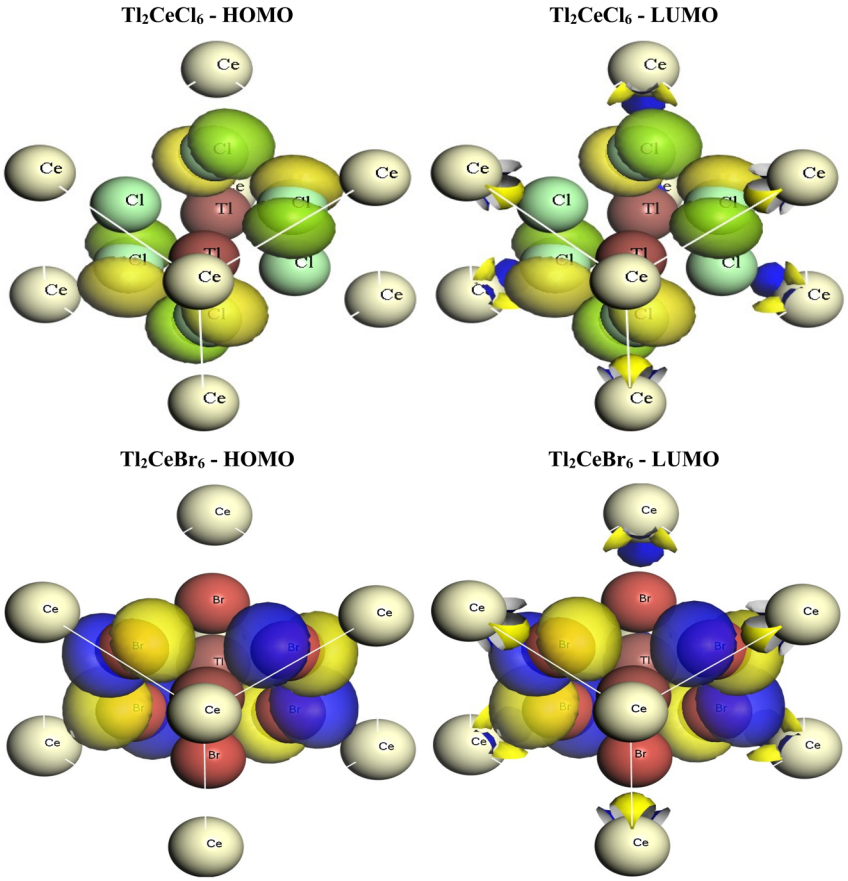

Fig. 7 HOMO and LUMO charge density distributions of Tl_2CeCl_6 and Tl_2CeBr_6 double perovskites.

halogen atoms, with Cl exhibiting stronger localization than Br due to its higher electronegativity. For Tl_2CeCl_6, the maximum charge density reaches 1.61×10^1 a.u. with a near-zero minimum of -3.97×10^{-3} a.u., indicating strong electron localization at the Cl sites and predominantly ionic Tl–Cl and Ce–Cl interactions.

Tl_2CeBr_6 shows a slightly lower maximum of 1.61×10^1 a.u. with a minimum of 1.29×10^{-2} a.u., reflecting substantial accumulation around Br but limited interstitial density. In_2CeCl_6 exhibits a lower maximum of 1.09×10^1 a.u. and a very small minimum of 7.61×10^{-4} a.u., while In_2CeBr_6 shows a comparable maximum with a slightly higher minimum (1.36×10^{-2} a.u.), suggesting more diffuse electron density around Br. The Ga-based systems display the strongest localization: Ga_2CeCl_6 reaches the highest maximum among all studied compounds at 3.95×10^1 a.u. with a near-zero minimum of 2.92×10^{-3} a.u., while Ga_2CeBr_6 retains similarly high values (3.94×10^1 a.u.; minimum 3.76×10^{-3} a.u.). Overall, the Ga-containing systems demonstrate the highest peak charge densities, whereas the In-based compounds show the lowest. A systematic trend emerges with A-site substitution, where electron density becomes more diffuse from Ga → In → Tl, consistent with increasing ionic size and reduced covalent interactions. Furthermore, Cl-based perovskites consistently exhibit stronger electron localization than their Br-based counterparts. These results highlight the direct connection between charge density features, bonding character, and the electronic stability of the D_2CeX_6 family. Notable studies supporting these findings include work by Faizan *et al.*, Rifat *et al.*, and Saikot *et al.*, which collectively highlight the role of charge density analysis in advancing halide double perovskite research for next-generation optoelectronic applications.[7,48,61]

3.6. Optical properties

The optical properties of a material define how it interacts with incident light, encompassing absorption, transmission, reflection, and emission processes across the ultraviolet (UV), visible, and infrared (IR) regions of the spectrum.[62] These characteristics are directly linked to the electronic structure and band gap, making them critical for determining a material's potential in optoelectronic applications. For double perovskites, analyzing the absorption coefficient, reflectivity, refractive index, dielectric function, and optical conductivity provides valuable insights into their suitability for device integration.

In this study, Fig. 9 presents the calculated optical properties of the D_2CeX_6 (D = Ga, In, Tl; X = Cl, Br) vacancy-ordered double perovskite compounds. The refractive indices of conventional double perovskites such as $(Cs_2, K_2, Rb_2)PbCl_6$ in the visible and ultraviolet regions offer significant advantages for solar cell applications, as their wide dielectric constants

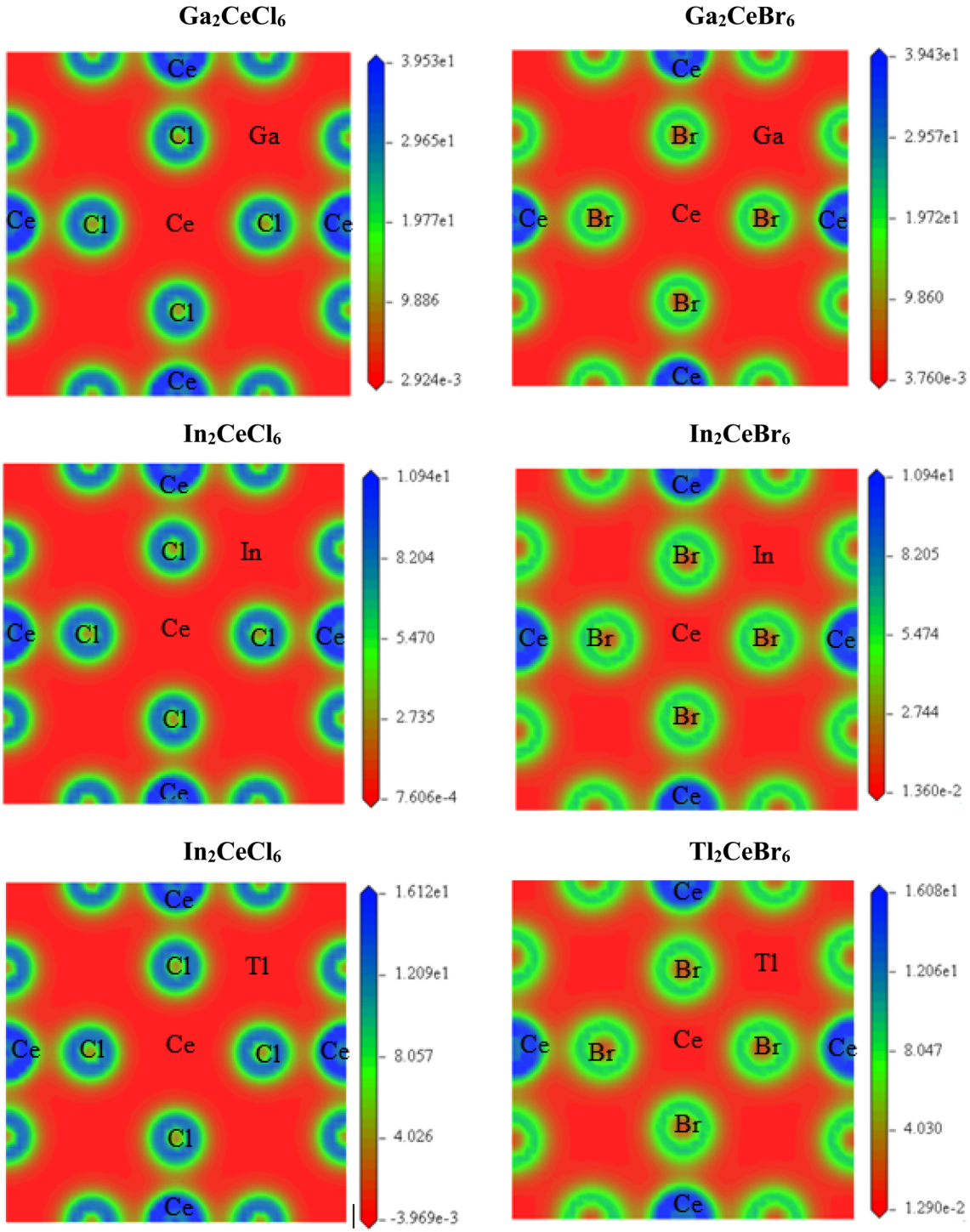

Fig. 8 Charge density mapping of D_2CeX_6 double perovskites.

enable strong photon absorption within the 1 to 5 eV energy range, making them suitable for efficient solar energy harvesting.[63] Similarly, Cs_2PbX_6 (X = Cl, Br, I) double perovskites demonstrate excellent optoelectronic properties, with direct band gaps ranging from 0.45 to 2.54 eV and high absorption coefficients of approximately 5.95×10^5 cm^{-1}, which highlight their potential for photovoltaic and optical applications.[64] However, the inherent toxicity and poor environmental stability of lead severely limit its large-scale utilization. On the other hand, Although Si-based halide double perovskites A_2SiI_6 (A = K, Rb, Cs; X = Cl, Br, I) show suitable band gaps (0.84 to 1.15 eV), strong visible absorption, and good thermal stability, conventional silicon materials still suffer from an indirect 1.12 eV band gap, weak light absorption, high-temperature processing requirements, and limited flexibility, making them less efficient.[65] In contrast, our investigated D_2CeX_6 compounds

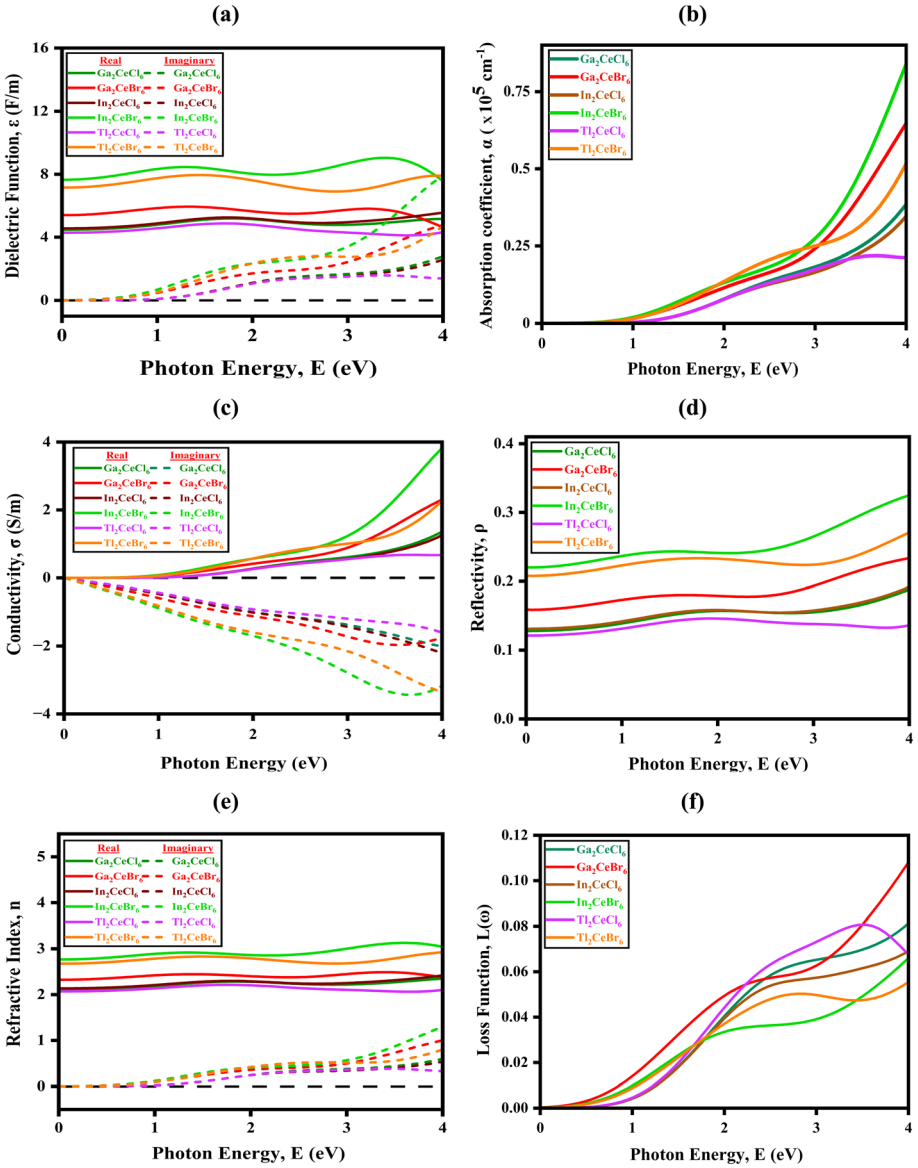

Fig. 9 Optical functions (a) dielectric function, (b) absorption coefficient, (c) conductivity, (d) refractive index, (e) reflectivity, (f) loss function of D_2CeX_6 double perovskites.

exhibit comparable or even superior optical characteristics, such as strong visible-light absorption, high dielectric constants, and large refractive indices, while eliminating the environmental and health hazards associated with lead. Moreover, their tunable band gaps within the optimal range for solar energy conversion, coupled with robust structural and mechanical stability, establish D_2CeX_6 materials as advanced, sustainable, and highly promising candidates for next-generation lead-free optoelectronic and photovoltaic devices.

3.6.1. Dielectric function. The dielectric function (ε) is a key parameter for understanding the optical and electronic behavior of materials. It consists of a real part (ε_1), which describes the material's ability to store electric energy, and an imaginary part (ε_2), which reflects energy loss due to absorption of electromagnetic radiation. For the D_2CeX_6 double perovskites, the calculated dielectric function is shown in Fig. 9(a) and is expressed as: $\varepsilon(\omega) = \varepsilon_1(\omega) + i\varepsilon_2(\omega)$.[66] Analyzing ε_1 and ε_2 provides insight into light–matter interactions, including polarization, charge screening, and optical absorption. These insights are essential for designing high-performance optoelectronic and photovoltaic devices, such as solar cells, LEDs, and photodetectors, where efficient light harvesting and minimal energy loss are critical.[67] It is defined as,[68]

$$\varepsilon_1(\omega) = 1 + \frac{2}{\pi} P \int_0^{\infty} \frac{\omega' \varepsilon_2 \left(\omega'\right)}{\omega'^2 - \omega^2} \mathrm{d}\omega' \tag{13}$$

$$\varepsilon_2(\omega) = \frac{8}{2\pi\omega^2} \sum_{nn'} |p_{nn'}(k)|^2 \frac{dS_k}{\nabla\omega_{nn'}(ks)} \tag{14}$$

Among the studied compounds, the static (0 eV) real part of the dielectric function (ε_1) is found to be 4.48 for Ga_2CeCl_6, 5.41 for Ga_2CeBr_6, 4.56 for In_2CeCl_6, 7.65 for In_2CeBr_6, 4.28 for Tl_2CeCl_6, and 7.216 for Tl_2CeBr_6, as presented in Fig. 9(a). The ε_1 parameter reflects a material's capacity to store electric energy when subjected to an external electromagnetic field. With increasing photon energy, ε_1 initially increases due to enhanced polarization arising from interband electronic transitions, reaching a peak value before gradually declining. The relatively high ε_1 values suggest strong polarization capability and effective screening of internal electric fields, which are beneficial for lowering exciton binding energy and improving charge carrier separation in optoelectronic applications.

For all the investigated compounds, the imaginary part of the dielectric function (ε_2), which represents the material's ability to absorb electromagnetic energy, begins to increase from photon energies between 0.31 and 0.87 eV. As photon energy rises, ε_2 increases and reaches its maximum within the visible region (1.5–4 eV), with peak values of 2.83 for Ga_2CeCl_6, 4.74 for Ga_2CeBr_6, 2.67 for In_2CeCl_6, 8.15 for In_2CeBr_6, 1.59 (at 3.31 eV) for Tl_2CeCl_6, and 5.067 for Tl_2CeBr_6. These maximum values generally occur around 4.0 eV. The highest ε_2 peak observed in In_2CeBr_6 indicates significant energy loss due to strong absorption of electromagnetic radiation, whereas Tl_2CeCl_6 exhibits the lowest ε_2 value, suggesting comparatively weaker absorption behavior.

The comparison between chloride and bromide analogs reveals that Br-based compounds generally exhibit enhanced imaginary dielectric components due to narrower band gaps, which facilitate easier electronic excitations. Conversely, Cl-based compounds show higher real parts, indicating stronger dielectric screening. The cation variation (Ga → In → Tl) affects both amplitude and energy dispersion, with heavier cations (Tl) contributing to stronger polarization and broader spectral response. Collectively, these dielectric characteristics reveal that Ga_2CeCl_6 and Tl_2CeBr_6 are particularly promising for optoelectronic applications requiring high dielectric screening and effective visible-light absorption.

3.6.2. Absorption coefficient. The absorption coefficient (α) is a critical parameter in materials science that quantifies how strongly a material absorbs light at specific photon energies. It is an important factor in assessing the appropriateness of materials for applications in optoelectronics, photovoltaics, scintillators, and photodetectors.[69,70] The absorption coefficient can be determined using eqn (15).

$$\alpha(\omega) = \frac{2\omega k(\omega)}{c} \tag{15}$$

The absorption coefficient, $\alpha(\omega)$, indicates how efficiently a material absorbs light at a particular angular frequency ω. It is commonly measured in cm^{-1} and is directly related to the extinction coefficient $k(\omega)$, which represents the imaginary part of the complex refractive index.[71,72] Fig. 9(b) shows that all six D_2CeX_6 compounds exhibit significant absorption coefficients, starting at photon energies of 0.8 to 1.7 eV. As the photon energy increases toward 3.0 eV, the absorption coefficients rise sharply, reaching values of 18 524 cm^{-1} (Ga_2CeCl_6), 24 394 cm^{-1} (Ga_2CeBr_6), 16 784 cm^{-1} (In_2CeCl_6), 27 560 cm^{-1} (In_2CeBr_6), 17 765 cm^{-1} (Tl_2CeCl_6), and 25 221 cm^{-1} (Tl_2CeBr_6). Such high absorption coefficients ($\alpha > 10^4$ cm^{-1})[73,74] in the visible range are highly desirable for thin-film solar cells, as they allow efficient photon harvesting with minimal material thickness, indicating that all studied materials are promising candidates for photovoltaic applications. The absorption behavior is also influenced by the halide substitution (Cl to Br), which shifts the absorption edge toward lower energies due to the narrower band gap of Br-based compounds, thereby enhancing visible-light absorption. Additionally, the choice of D-site cation (Ga, In, Tl) affects the magnitude and position of absorption peaks, with In- and Tl-based compounds generally exhibiting higher absorption coefficients than Ga-based ones. These trends highlight the tunability of optical properties in D_2CeX_6 double perovskites through compositional engineering, which is crucial for optimizing performance in both solar energy conversion and optoelectronic applications.

3.6.3. Conductivity. Conductivity (σ) is a fundamental physical property that measures a material's ability to conduct electric current, especially under the influence of an electromagnetic field.[75] In D_2CeX_6 double perovskites, the optical conductivity is frequency-dependent and complex, consisting of a real part, which represents the dissipative response or actual current flow, and an imaginary part, which corresponds to energy storage and polarization, as shown in Fig. 9(c). Calculating the optical conductivity is essential for understanding charge carrier dynamics, photon–electron interactions, and energy transport mechanisms, all of which are critical for the design of high-performance optoelectronic and photonic devices. The optical conductivity is obtained directly from the complex dielectric function through the following relation:

$$\sigma_1(\omega) = \frac{2\pi e^2\hbar}{m^2\omega\Omega}\sum_{k,v,c}|\langle\psi_{ck}|p|\psi_{vk}\rangle|^2\delta(E_{ck} - E_{vk} - \hbar\omega) \tag{16}$$

In this expression, Ω denotes the volume of the unit cell, ψ_{vk} and ψ_{ck} represent the valence and conduction band wavefunctions at a given k-point, and δ is the Dirac delta function that maintains energy conservation, from the conductivity spectra. The real component of the optical conductivity exhibits a trend similar to that of the absorption coefficient, as both originate from electronic transitions between the valence and conduction bands. Higher values of real optical conductivity reflect stronger photon–electron interactions, leading to enhanced light absorption and more efficient generation of charge carriers. In D_2CeX_6 double perovskites, this relationship indicates that compounds with large absorption coefficients also display pronounced conductivity peaks, emphasizing their suitability for photovoltaic and optoelectronic applications, where effective light harvesting and rapid charge transport are crucial for device performance.

Fig. 9(c) shows the real and imaginary parts of optical conductivity (σ) as a function of photon energy (0 to 4 eV) for the double perovskites Ga_2CeCl_6, Ga_2CeBr_6, In_2CeCl_6, In_2CeBr_6, Tl_2CeCl_6, and Tl_2CeBr_6. Among all, Ga_2CeCl_6 exhibits the

highest real conductivity, rising sharply beyond 2.5 eV, indicating superior photon-induced carrier excitation and possible metallic-like behavior at high photon energy. Ga_2CeBr_6 also shows strong conductivity but slightly lower than Ga_2CeCl_6, suggesting that replacing Cl with Br slightly reduces the optical response, likely due to the larger ionic radius and weaker bonding of Br. The In-based compounds (In_2CeCl_6 and In_2CeBr_6) show moderate conductivity values, implying less efficient charge carrier transition compared to Ga-based systems; however, In_2CeBr_6 displays a smoother rise, indicating better optical absorption at higher energies than In_2CeCl_6. In contrast, Tl-based compounds (Tl_2CeCl_6 and Tl_2CeBr_6) possess the lowest real conductivity across the entire photon energy range, reflecting their relatively poor electronic transition probability and higher resistive character. As shown in Fig. 6(c), the imaginary part of the optical conductivity initially starts with negative values, indicating a reactive polarization response. With increasing photon energy, the conductivity decreases further and reaches minimum values of −2.0 at 4.00 eV for Ga_2CeCl_6, −1.95 at 3.40 eV for Ga_2CeBr_6, −2.184 at 4.00 eV for In_2CeCl_6, −3.43 at 3.42 eV for In_2CeBr_6, −1.57 at 4.00 eV for Tl_2CeCl_6, and −3.41 at 3.56 eV for Tl_2CeBr_6. This transient negative behavior reflects strong reactive polarization, which is advantageous for applications such as optical switching and memory devices. Notably, cation substitution (Ga → In → Tl) and halide replacement (Cl → Br) systematically influence the peak positions and depth of the negative conductivity response.

Heavier cations and larger halides generally shift the spectral features toward lower energies and enhance polarization effects, thereby tailoring the material's suitability for frequency-selective optoelectronic and photonic applications.

3.6.4. Reflectivity. Reflectivity (ρ) is a material's ability to reflect incident electromagnetic radiation, expressed as the ratio of reflected power to incident power at a specific photon energy.[76] It is a dimensionless quantity ranging from 0 to 1 (or 0% to 100%) and depends on the material's optical properties and surface characteristics. The reflectivity (ρ) is calculated from the complex dielectric function using the relation,

$$R(\omega) = \frac{(\eta - 1)^2 + k^2}{(\eta + 1)^2 + k^2} \quad (17)$$

Fig. 9(d) illustrates the variation of reflectivity (ρ) with photon energy (E) from 0 to 4 eV for six Ce-based double perovskite compounds: Ga_2CeCl_6, Ga_2CeBr_6, In_2CeCl_6, In_2CeBr_6, Tl_2CeCl_6, and Tl_2CeBr_6. Reflectivity represents the fraction of incident light that is reflected from a material's surface and serves as an important indicator of its optical response and surface electronic structure. Overall, all compounds exhibit relatively low reflectivity (<0.4), suggesting strong light absorption and significant potential for optoelectronic and photovoltaic applications. At 0.1 eV, the initial reflectivity values are 0.128, 0.1589, 0.131, 0.220, 0.1213, and 0.1213 for Ga_2CeCl_6, Ga_2CeBr_6, In_2CeCl_6, In_2CeBr_6, Tl_2CeCl_6, and Tl_2CeBr_6, respectively. All materials show notable optical activity in the visible range (1.5–4 eV). As the photon energy increases, the reflectivity rises to 0.189, 0.23, 0.185, 0.32, 0.135, and 0.27 for Ga_2CeCl_6, Ga_2CeBr_6, In_2CeCl_6, In_2CeBr_6, Tl_2CeCl_6, and Tl_2CeBr_6, respectively. Overall, these reflectivity characteristics highlight distinct, application-specific roles, underscoring the importance of reflectivity in optimizing these materials for optoelectronic technologies.

3.6.5. Refractive index. The refractive index (n) is a complex optical parameter that characterizes the propagation of light within a material.[77] It consists of a real part, indicating the phase velocity of light in the medium, and an imaginary part, which is associated with absorption losses (extinction coefficient). The refractive index of D_2CeX_6 double perovskites shown in Fig. 9(e) is essential for optimizing their performance in photonic, optoelectronic, and photovoltaic applications, since it governs light–matter interaction, reflection, refraction, and light confinement efficiency. The $n(\omega)$ is computed from the complex dielectric function, using the relation,[78]

$$n(\omega) = \frac{1}{\sqrt{2}}\left[\left(\varepsilon_1(\omega)^2 + \varepsilon_2(\omega)^2\right)^{\frac{1}{2}} + \varepsilon_1(\omega)\right]^{\frac{1}{2}} \quad (18)$$

$n(\omega)$ represents the frequency-dependent refractive index, indicating how the speed of light varies in the material at a particular photon energy.

Fig. 9(e) illustrates the variation of the refractive index (n), both real and imaginary components, with photon energy (0 to 4 eV) for six Ce-based double perovskite compounds: Ga_2CeCl_6, Ga_2CeBr_6, In_2CeCl_6, In_2CeBr_6, Tl_2CeCl_6, and Tl_2CeBr_6. The solid lines denote the real part of the refractive index, which signifies the phase velocity of light within the material, while the dashed lines indicate the imaginary part, which represents the extinction coefficient or absorption losses. Overall, the real part of n remains between approximately 2.0 and 4.5, showing moderate to high optical density typical of semiconducting materials. Ga_2CeCl_6 exhibits the highest real refractive index across most of the energy range, peaking near 4.5, implying stronger light–matter interaction and higher optical polarization. Ga_2CeBr_6 also shows a comparatively high refractive index but slightly lower than its Cl counterpart, suggesting that Br substitution reduces the electronic polarizability due to its larger ionic radius and weaker bond strength. The In-based compounds (In_2CeCl_6 and In_2CeBr_6) have intermediate refractive indices around 2.5–3.0, indicating moderate optical response with more uniform energy dependence, suitable for balanced optical transmission and absorption. In contrast, Tl_2CeCl_6 and Tl_2CeBr_6 display the lowest refractive indices (∼2.0 to 2.5), reflecting weaker electronic polarization and higher optical transparency. The imaginary components increase gradually beyond 2 eV for all compounds, highlighting the onset of interband electronic transitions that contribute to absorption. Among these, Ga-based compounds again exhibit the strongest imaginary peaks, confirming their intense optical activity, while Tl-based compounds show the weakest, consistent with their low absorption tendency. Overall, both halide and cation substitution significantly influence refractive behavior, with the comparative trend for real refractive index following Ga_2CeCl_6 >

Ga_2CeBr_6 > In_2CeBr_6 > In_2CeCl_6 > Tl_2CeCl_6 > Tl_2CeBr_6. This indicates that Ga-based systems, particularly Ga_2CeCl_6, possess superior optical confinement and are more suitable for light-modulating or refractive applications, whereas Tl-based perovskites are better for transparency-driven optoelectronic devices.

3.6.6. Loss function. The energy loss function, $L(\omega)$, defined as the imaginary part of the inverse dielectric function, describes the energy dissipated by fast electrons traversing a material and is essential for probing plasmonic behavior, electron scattering, and optical transitions.[79] The optical loss function, $L(\omega)$, can be calculated using the following relation:[80]

$$L(\omega) = -\mathrm{Im}\left[\frac{1}{\varepsilon(\omega)}\right] = \frac{\varepsilon_2(\omega)}{\varepsilon_1^2(\omega) + \varepsilon_2^2(\omega)} \quad (19)$$

As shown in Fig. 9(f), the relationship between the Loss Function, $L(\omega)$, on the y-axis and photon energy, E (in electron volts, eV), on the x-axis for six different materials: Ga_2CeCl_6, Ga_2CeBr_6, In_2CeCl_6, In_2CeBr_6, Tl_2CeCl_6, and Tl_2CeBr_6. Each material is represented by a distinct colored line as indicated in the legend: green for Ga_2CeCl_6, red for Ga_2CeBr_6, brown for In_2CeCl_6, cyan for In_2CeBr_6, magenta for Tl_2CeCl_6, and orange for Tl_2CeBr_6. The general trend for all materials shows that the loss function starts near zero at low photon energies (0 eV) and increases as the photon energy increases up to 4 eV. However, the rate and magnitude of increase differ for each compound. Ga_2CeBr_6 exhibits the highest loss function values, surpassing 0.10 at around 4 eV, indicating the strongest loss effect at high photon energies among the six. Tl_2CeCl_6 follows closely, peaking slightly below Ga_2CeBr_6 but still above 0.08. Ga_2CeCl_6 and In_2CeCl_6 show moderate increases, with their loss functions rising to approximately 0.08 and 0.07, respectively, at 4 eV. The In_2CeBr_6 and Tl_2CeBr_6 compounds display the lowest loss functions overall, with Tl_2CeBr_6 being the lowest, peaking near 0.06. Comparatively, the bromide variants (Ga_2CeBr_6, In_2CeBr_6, Tl_2CeBr_6) generally display higher loss functions than their chloride counterparts at higher photon energies, except for In_2CeBr_6, which is lower than In_2CeCl_6. Among the cations, Ga-based compounds tend to show higher loss functions than In-based compounds, while Tl-based compounds are intermediate but closer to Ga-based, especially in the chloride form.

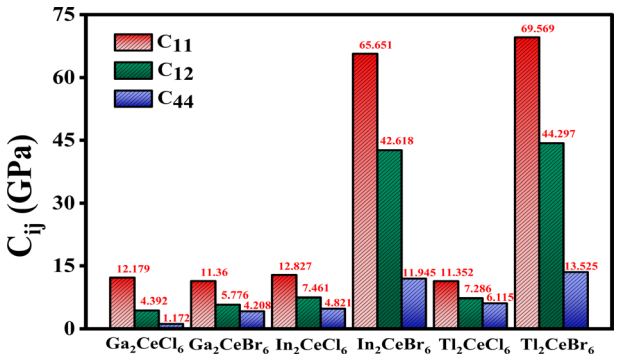

Fig. 10 Calculated elastic constants (C_{ij}) for D_2CeX_6 double perovskites.

This suggests that both the halide type and the central metal ion influence the loss function behavior, with bromides and Ga ions generally enhancing the loss function, except in specific cases like In_2CeBr_6.

3.7. Elastic and mechanical properties

Mechanical properties define a material's response to stress, including its strength, elasticity, stiffness, and ductility. These are vital for assessing structural stability and durability. In solar cells, especially in thin-film or flexible applications, materials must endure mechanical strain during fabrication and operation without cracking or deforming.[81] Elastic constants define the mechanical behavior of a solid under applied stress or strain, serving as essential indicators of its stability, rigidity, and bonding nature. In the framework of Hooke's law, the stress tensor (σ) is linearly related to the strain tensor (ε) through:[82]

$$\sigma_{ij} = C_{ijkl}\varepsilon_{kl} \quad (20)$$

where C_{ij} are the components of the fourth-rank elastic stiffness tensor. The symmetry of the crystal determines the number of independent elastic constants. In cubic crystals, there are only three independent constants: C_{11}, C_{12}, and C_{44}. The mechanical stability of cubic crystals was evaluated using the Born–Huang criteria, expressed as:[83–85]

$$C_{11} > 0,\ 4C_{44} > 0,\ C_{11} - C_{12} > 0 \text{ and } C_{11} + 2C_{12} > 0 \quad (21)$$

All the conditions of the Born–Huang stability criteria are satisfied and yield positive values, indicating that the D_2CeX_6 double perovskites are mechanically stable, as shown in Fig. 10. This confirms their ability to withstand external stress without structural failure, making them suitable for practical applications in devices where mechanical integrity is essential.

The mechanical properties of D_2CeX_6 double perovskites are critical for ensuring structural integrity, thermal stability, and resistance to external stress. The bulk modulus, shear modulus, Young's modulus, Poisson's ratio, and Pugh's ratio serve as indicators of ductility or brittleness, guiding decisions about the materials' suitability for device integration.[48,61] Mechanical stability plays a direct role in the long-term reliability and lifespan of perovskite-based solar cells. Therefore, a thorough understanding and optimization of these properties are essential for developing mechanically robust, efficient, and commercially viable perovskite solar absorbers for future energy applications.

Fig. 11 illustrates the mechanical parameters of D_2CeX_6 double perovskites, including bulk modulus (B), shear modulus (G), Young's modulus (Y), Poisson's ratio (ν), Pugh's ratio (B/G), and anisotropy factor (A^U), which are represented by equations as follows.[86]

$$B_H = \frac{B_H + B_R}{2} \quad (22)$$

$$G_H = \frac{G_V + B_R}{2} \quad (23)$$

$$Y = \frac{9BG}{(3B + G)} \quad (24)$$

Bulk modulus (B) measures a material's resistance to uniform compression and indicates mechanical stiffness. Higher B values reflect strong interatomic bonding and limited compressibility, while lower values correspond to flexible or soft materials. Typically, materials with $B > 40$ GPa are classified as hard, whereas $B < 40$ GPa denotes soft or flexible behavior.[48] As shown in Fig. 11(a), In_2CeBr_6 (50.30 GPa) and Tl_2CeBr_6 (52.72 GPa) are hard materials, while Ga_2CeCl_6, Ga_2CeBr_6, In_2CeCl_6, and Tl_2CeCl_6 are soft, capable of accommodating volume changes more easily. Shear modulus (G) quantifies resistance to shape (shear) deformation at constant volume. Higher G values indicate strong internal bonding and shear rigidity, while lower values correspond to easier shear deformation. As depicted in Fig. 11(b), Tl_2CeBr_6 (13.16 GPa) and In_2CeBr_6 (11.77 GPa) exhibit the highest shear moduli, making them suitable for load-bearing and wear-resistant applications.

In contrast, Ga_2CeCl_6 (1.94 GPa) and Ga_2CeBr_6 (3.57 GPa) are more flexible, advantageous for damping, vibration isolation, or low-shear optical layers. Young's modulus (E) reflects stiffness and resistance to elongation under uniaxial stress. Fig. 11(c) shows that In_2CeCl_6 and Tl_2CeBr_6 have the highest E values, consistent with their B and G moduli, making them ideal for rigid supports, optical mounts, and stiff structural components. Conversely, Ga_2CeCl_6 (5.34 GPa) exhibits enhanced elasticity, suitable for flexible electronics, wearable devices, and strain-tolerant applications. Overall, the variation of B, G, and E across cation–anion substitutions demonstrate the tunable mechanical behavior of D_2CeX_6 perovskites, enabling design for either rigid, high-strength applications (In- and Tl–Br based) or flexible, damping-oriented applications (Ga-based). The ductile or brittle nature of a material can be assessed using Poisson's ratio (ν) and Pugh's ratio (B/G). In general, materials with ν

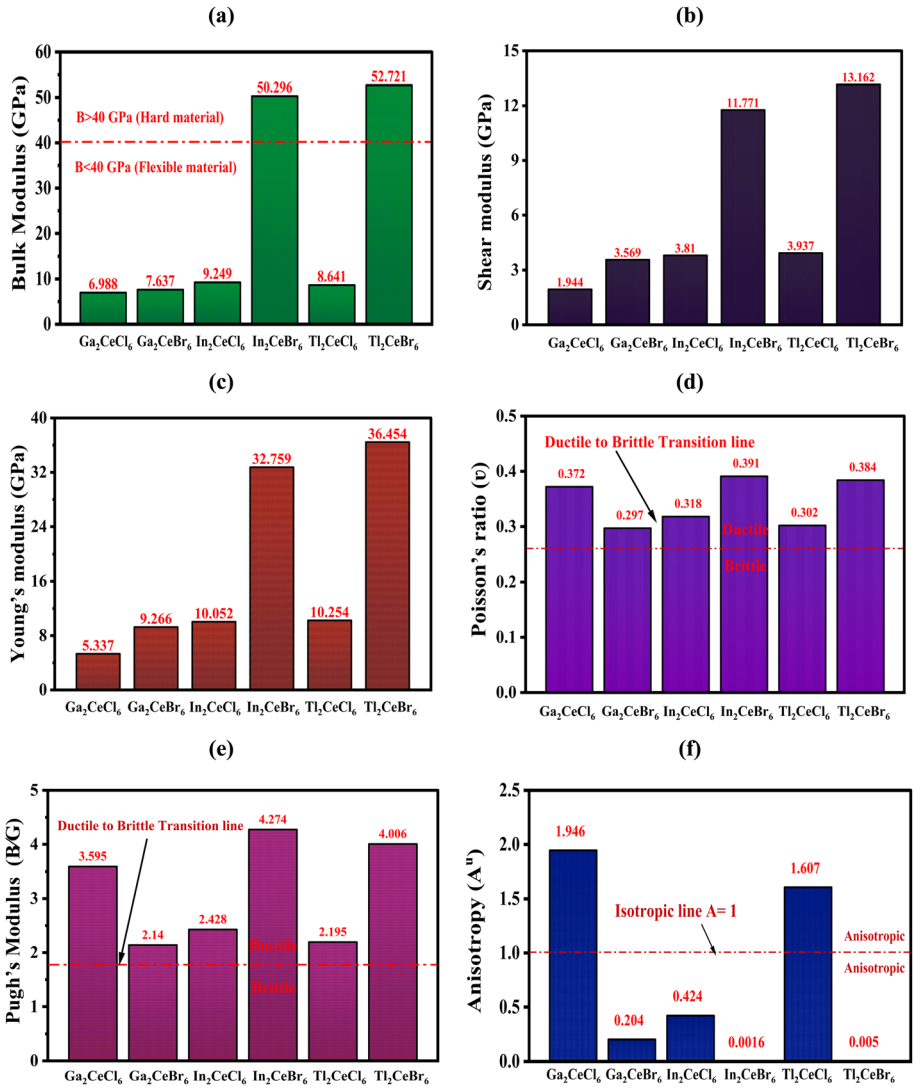

Fig. 11 Mechanical parameters of (a) Bulk modulus, (b) Shear modulus, (c) Young's modulus, (d) Poisson's ratio, (e) Pugh's modulus, and (f) anisotropy of D_2CeX_6 double perovskite materials.

exceeding 0.26 and B/G greater than 1.75 are classified as ductile.[29]

$$\nu = \frac{3B - 2G}{2(3B + G)} \quad (25)$$

Poisson's ratio (ν), illustrated in Fig. 11(d), describes the ratio of lateral to axial strain under applied stress, reflecting both bonding characteristics and ductility. For the D_2CeX_6 perovskites studied, the calculated ν values are 0.372, 0.297, 0.318, 0.391, 0.302, and 0.384 for Ga_2CeCl_6, Ga_2CeBr_6, In_2CeCl_6, In_2CeBr_6, Tl_2CeCl_6, and Tl_2CeBr_6, respectively. Since all values exceed the critical threshold of 0.26, these compounds exhibit ductile behavior, indicating their ability to undergo plastic deformation and their suitability for flexible applications such as strain-tolerant devices, vibration-damping layers, and ductile electrodes. Likewise, Pugh's ratio (B/G), shown in Fig. 11(e), provides a complementary measure of ductility, where values above 1.75 confirm ductile behavior. All investigated D_2CeX_6 perovskites surpass this criterion, reinforcing the conclusion from Poisson's ratio that these materials are inherently ductile.

The Universal Anisotropy Index (A^U) in Fig. 11(f) quantifies the directional dependence of elastic properties, where zero denotes perfect isotropy.[87]

$$A^U = \frac{B_V}{B_r} + 5\frac{G_V}{B_R} - 6 \geq 0 \quad (26)$$

In_2CeBr_6 ($A^U = 0.0016$) and Tl_2CeBr_6 ($A^U = 0.005$) exhibit near-isotropic behavior, suitable for applications where mechanical stability is critical, for example, in sensors, microelectronic substrates, and integrated circuits. On the other hand, Ga_2CeCl_6 displays significant anisotropy ($A^U = 1.946$), implying strongly direction-dependent mechanical responses, which could be leveraged in anisotropic optical or piezoelectric devices where orientation-dependent properties are desired.

3.8. Anisotropy

Anisotropy refers to the variation of material properties with direction, and its evaluation is crucial in understanding the mechanical behavior of D_2CeX_6 double perovskites.

From the graphical assessments, Fig. 12–14, Ga_2CeCl_6 displays the highest mechanical anisotropy with Young's modulus ranging between ~2.5 and 9.0 GPa, indicating its stiffness varies significantly with direction. In contrast, Tl_2CeBr_6 shows the highest and most isotropic stiffness (~35 to 37 GPa), followed by In_2CeBr_6 (~32 to 33 GPa), highlighting their superior mechanical robustness and uniformity. Similarly, in

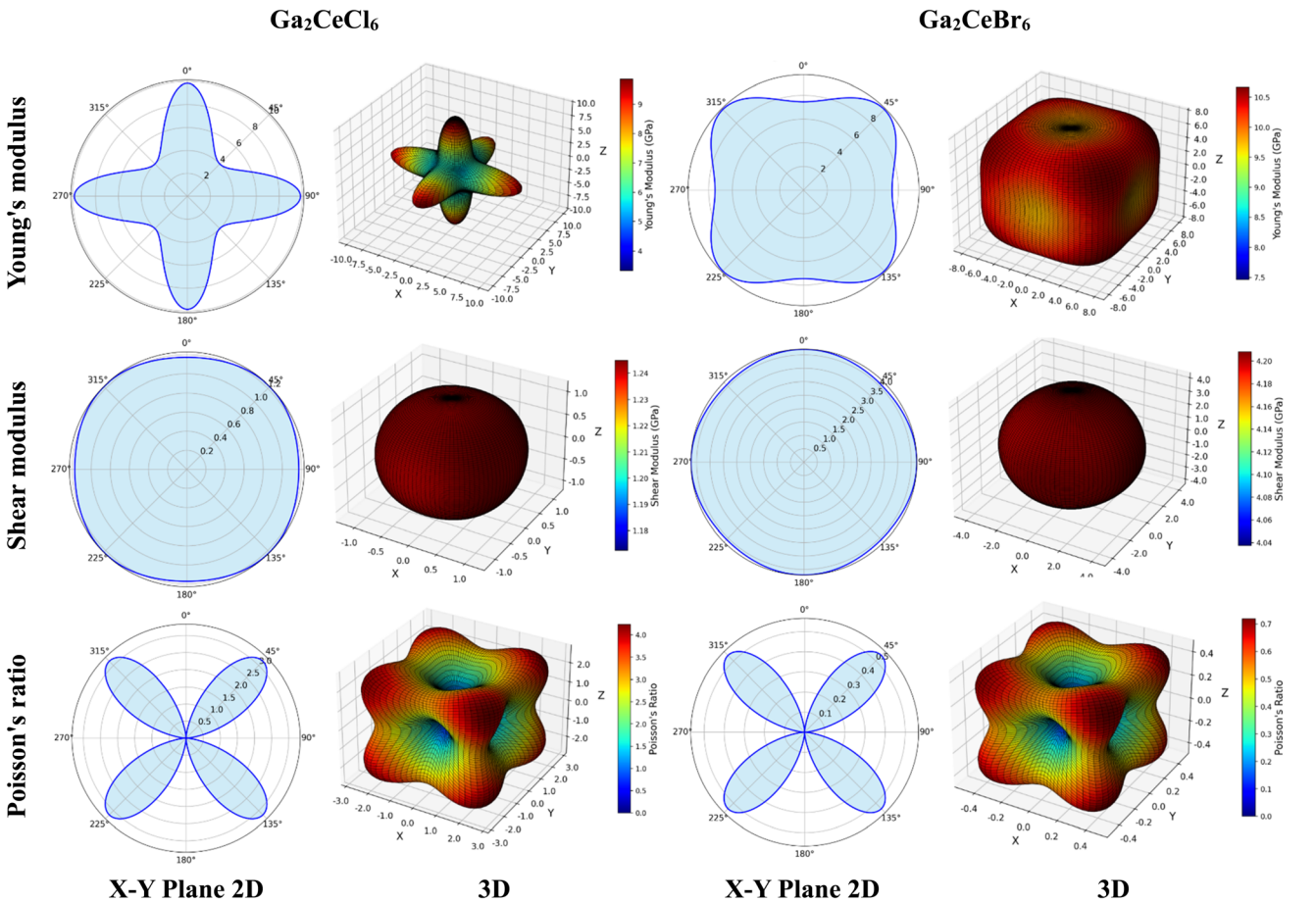

Fig. 12 Graphical assessment of Ga_2CeCl_6 and Ga_2CeBr_6 double perovskites anisotropy showing 2D and 3D figures.

shear modulus, Tl_2CeBr_6 peaks (~13.5 GPa), while Ga_2CeCl_6 registers the lowest (~1.17 to 1.24 GPa).

For Poisson's ratio, Tl_2CeBr_6 and In_2CeBr_6 exhibit broader, more spherical distributions (~0.2 to 1.0), suggesting low anisotropy, whereas Ga_2CeCl_6 again demonstrates high directionality with values dipping to ~0.05.

Comparing the compounds, bromide-based materials are generally stiffer and more isotropic than their chloride counterparts, and mechanical performance improves from Ga → In → Tl due to increasing atomic size and enhanced bonding.[88,89] These insights are vital for tailoring materials for specific directional mechanical responses or ensuring mechanical stability in multifunctional devices. Accurate anisotropy assessment helps optimize materials for real-world applications, guiding experimental synthesis and structural design.

3.9. Molecular dynamics (MD) analysis

Molecular Dynamics (MD) is a computational technique that simulates the motion of atoms and molecules over time by solving Newton's equations of motion, providing a dynamic perspective on material behavior under different energy components and temperatures.[90] In this study, simulations were performed at 300 K, 600 K, and 900 K to monitor the potential energy (P.E.), kinetic energy (K.E.), and total energy (T.E.) of the systems. MD analysis offers valuable insights into thermal and energetic stability, atomic vibrations, diffusion mechanisms, and structural evolution under varying temperature or pressure conditions.[91] This approach is particularly important for predicting material performance in real-world environments, including stability, phase transitions, and mechanical or electronic responses under thermal stress.[92] Therefore, MD simulations are essential for assessing and optimizing the structural robustness and functional reliability of materials in practical applications. Fig. 15 illustrates the variation of energy components and temperature with simulation time for Ga_2CeCl_6 at different temperatures (300 K, 600 K, and 900 K). In Fig. 15(a)–(c), the potential energy (P.E.), kinetic energy (K.E.), and total energy (T.E.) are plotted against time for 300 K, 600 K, and 900 K, respectively. At 300 K (Fig. 15(a)), the system shows relatively stable energy fluctuations, with total energy oscillating mildly around equilibrium, indicating thermal stability at lower temperatures. As the temperature increases to 600 K (Fig. 15(b)), both kinetic and total energies rise significantly, accompanied by slightly larger oscillations, reflecting enhanced atomic motion. At 900 K (Fig. 15(c)), the kinetic and total energies reach their highest values, exhibiting pronounced fluctuations, which suggests strong thermal vibrations and a possible onset of lattice instability.

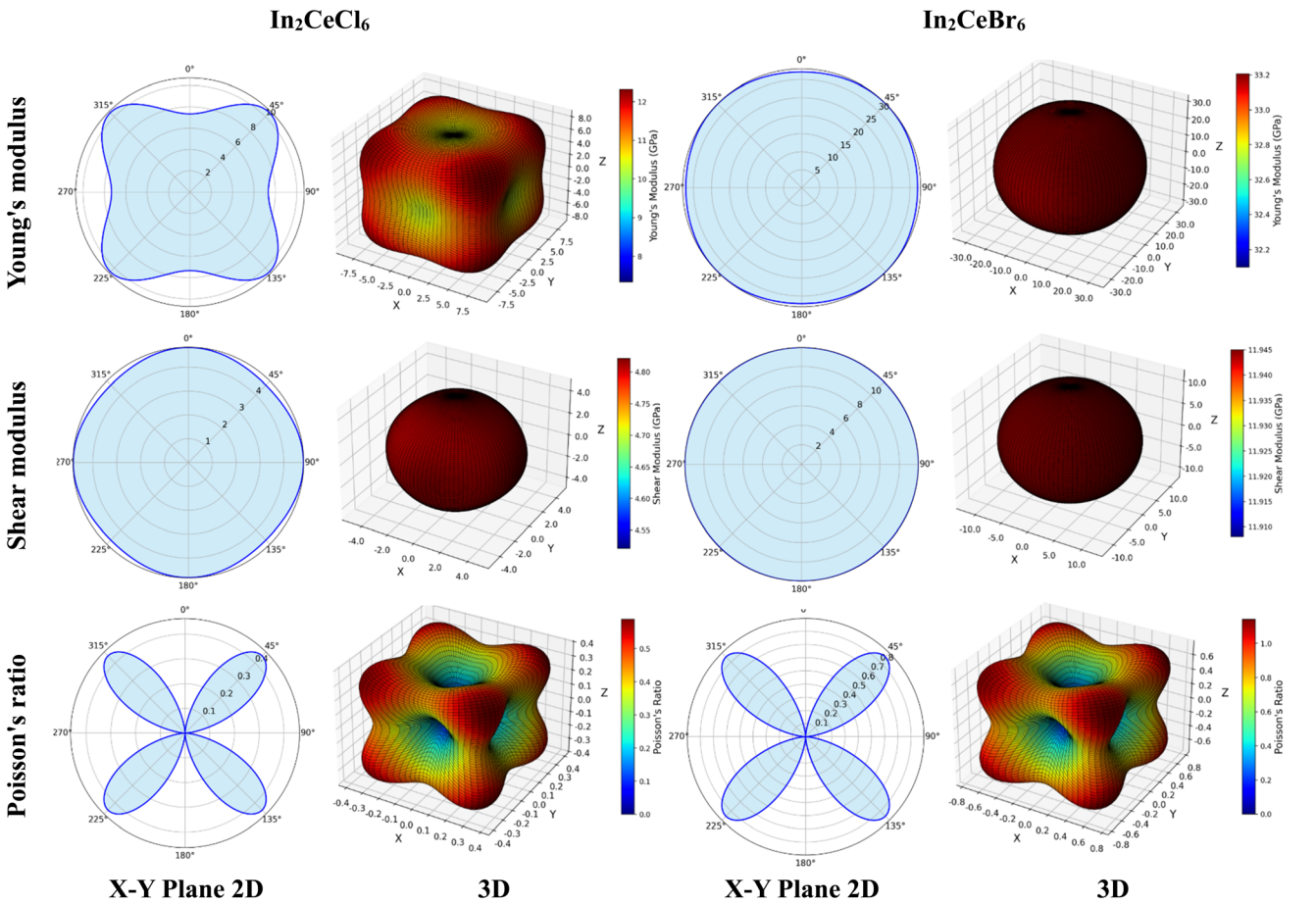

Fig. 13 Graphical assessment of In_2CeCl_6 and In_2CeBr_6 double perovskites anisotropy showing 2D and 3D figures.

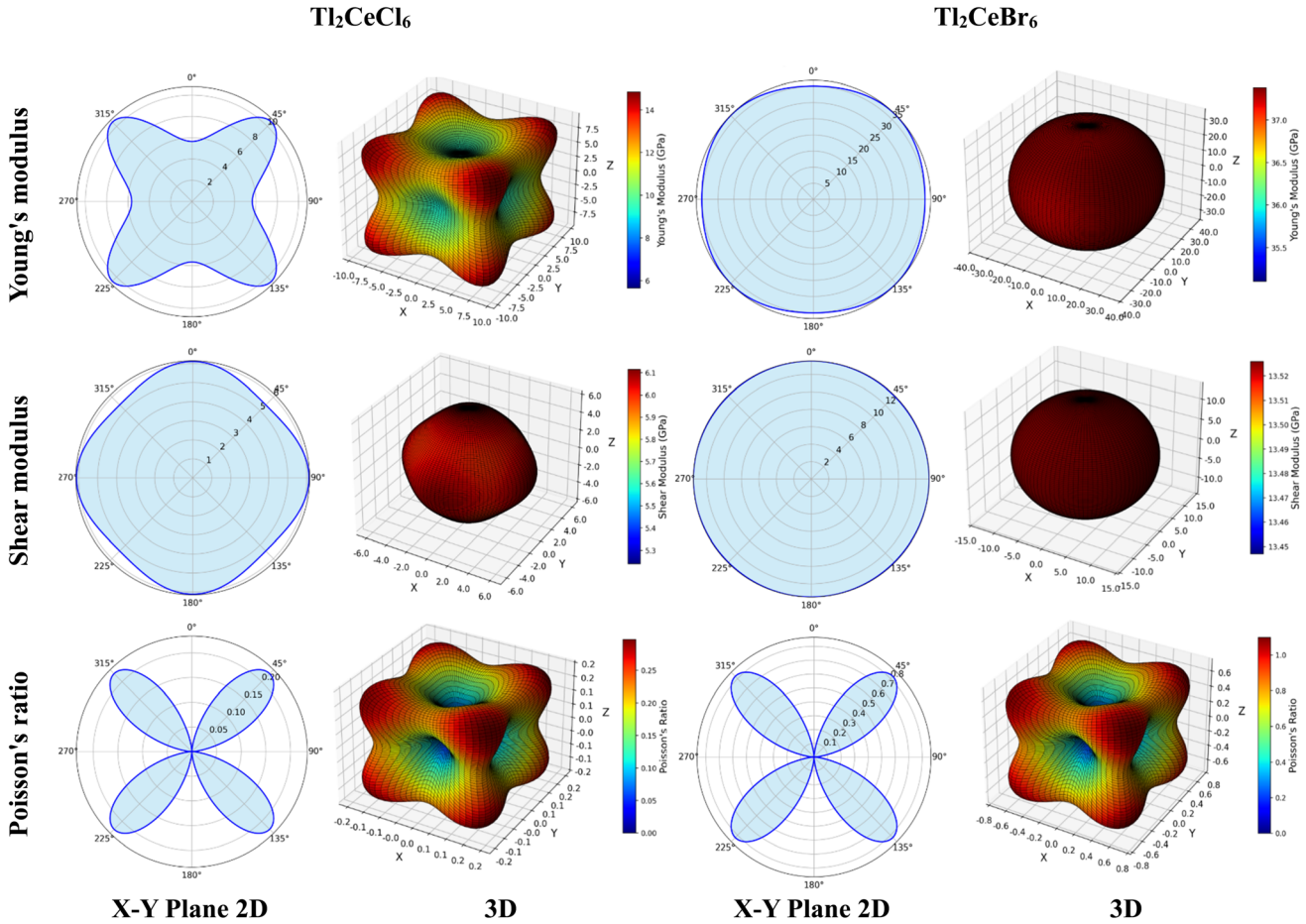

Fig. 14 Graphical assessment of Tl_2CeCl_6 and Tl_2CeBr_6 double perovskites anisotropy showing 2D and 3D figures.

The potential energy remains comparatively lower and negative in all cases, consistent with the system's bound state. Fig. 15(d) presents the temperature variation over time, showing steady temperature maintenance around the target values (300 K, 600 K, and 900 K), with moderate oscillations attributed to thermal equilibrium fluctuations.

Fig. 16 depicts the variation of kinetic energy (K.E.), potential energy (P.E.), total energy (T.E.), and temperature (T) of Ga_2CeBr_6 as a function of time at different temperatures (300 K, 600 K, and 900 K) during molecular dynamics (MD) simulations. Fig. 16(a)–(c) shows that as temperature increases, the amplitude and average values of K.E. and T.E. rise, reflecting enhanced atomic vibrations and thermal activity. At 300 K, the system exhibits relatively small oscillations and stable energy values, indicating a well-equilibrated and structurally stable phase. At 600 K, both K.E. and T.E increase moderately, with more frequent fluctuations due to higher thermal motion.

At 900 K, the oscillations become much larger, and the total energy reaches its maximum level, signifying strong lattice vibrations and possibly anharmonic effects. P.E remains negative across all temperatures but shows a gradual upward shift with increasing temperature, suggesting partial weakening of interatomic interactions. Fig. 16(d) compares the temperature variation over time, showing that each system stabilizes near its target temperature (300 K, 600 K, and 900 K) with expected thermal fluctuations.

Fig. 17 illustrates the variation of kinetic energy (K.E.), potential energy (P.E.), total energy (T.E.), and temperature (T) of In_2CeCl_6 during molecular dynamics (MD) simulations at 300 K, 600 K, and 900 K over a 50 ps timescale. Fig. 17(a)–(c), the energy profiles show that as temperature increases, both K.E. and T.E rise significantly, while P.E remains negative but slightly increases, indicating stronger atomic vibrations and enhanced atomic displacement at elevated temperatures.

At 300 K, the energy fluctuations are relatively small, implying structural stability with limited atomic motion. At 600 K, oscillations in K.E. and T.E become more pronounced, showing moderate thermal agitation. At 900 K, energy oscillations are much larger, signifying intense atomic vibration and possible lattice distortion. Fig. 17(d) compares the temperature profiles, showing stable fluctuations around the target temperatures (300 K, 600 K, and 900 K), confirming proper thermal equilibration during the MD simulations.

Fig. 18 presents the variation of kinetic energy (K.E.), potential energy (P.E.), total energy (T.E), and temperature (T) of In_2CeBr_6 over 50 ps at three different temperatures, 300 K, 600 K, and 900 K, obtained from molecular dynamics simulations. Fig. 18(a)–(c), the system exhibits increasing energy magnitudes

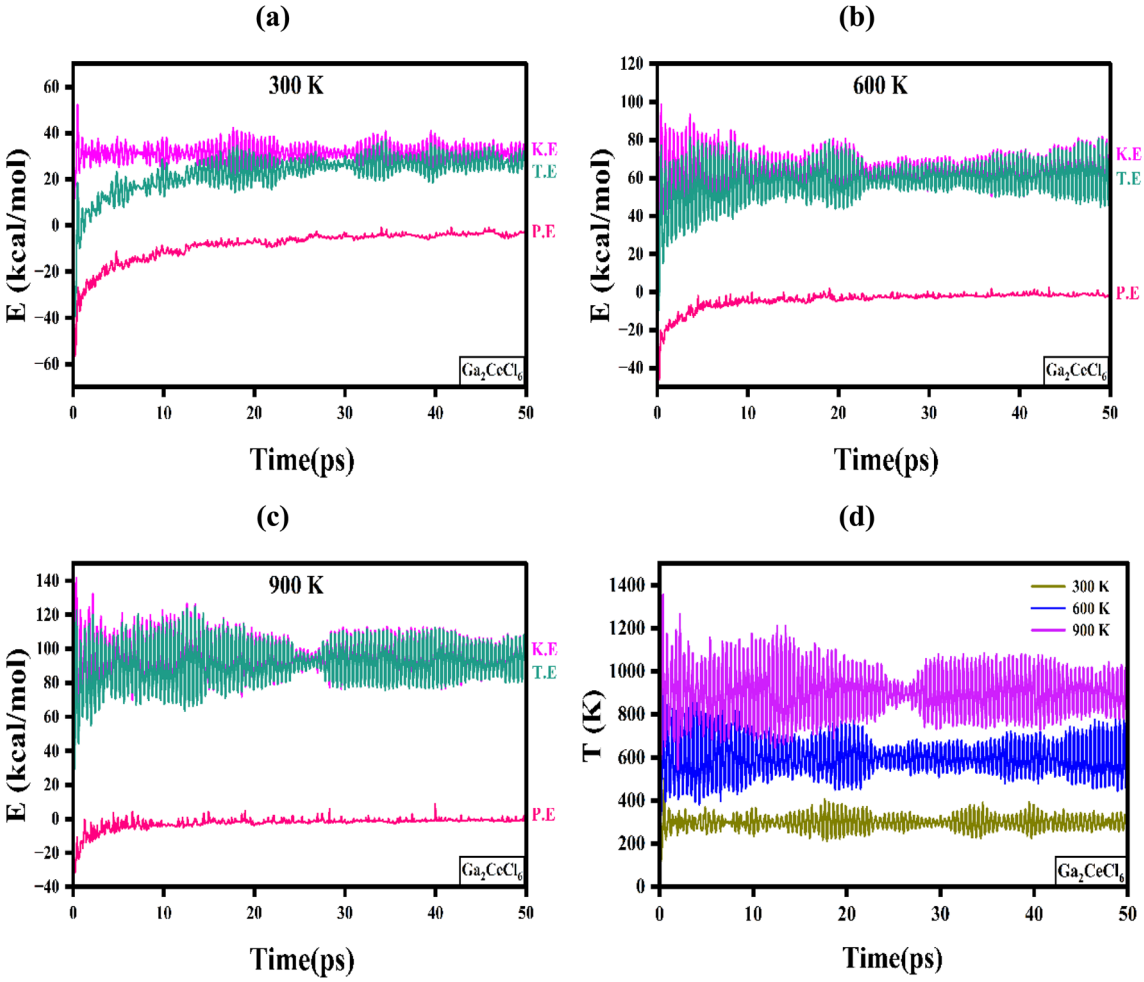

Fig. 15 Time evolution of potential, kinetic, and total energy for Ga_2CeCl_6 double perovskite at (a) 300 K, (b) 600 K, (c) 900 K, and (d) temperature variation over time.

with rising temperature, indicating stronger atomic vibrations and enhanced lattice dynamics. At 300 K, K.E. and T.E. remain relatively stable with small oscillations, reflecting a thermally equilibrated and structurally stable configuration. As the temperature increases to 600 K, both K.E. and T.E rise moderately, accompanied by more pronounced oscillations due to intensified thermal motion. At 900 K, large fluctuations in K.E. and T.E are observed, implying vigorous atomic vibrations and possible anharmonic effects, while P.E remains negative but shifts slightly upward, suggesting reduced interatomic binding strength. Panel (d) compares temperature variations over time, showing consistent stabilization near the target values of 300 K, 600 K, and 900 K with periodic fluctuations characteristic of dynamic equilibrium.

Fig. 19 presents the variation of energy and temperature with simulation time for Tl_2CeCl_6 at three different temperatures: 300 K, 600 K, and 900 K. Fig. 19(a to c) show the evolution of kinetic energy (K.E), potential energy (P.E), and total energy (T.E), while Fig. 19(d) depicts the temperature fluctuations over time. At 300 K, Fig. 19(a), the system displays stable energy oscillations with minor fluctuations, indicating good thermal equilibrium and structural stability. As the temperature rises to 600 K, Fig. 19(b), both kinetic and total energies increase noticeably, accompanied by slightly larger oscillations, suggesting enhanced atomic motion. At 900 K, Fig. 19(c), the total and kinetic energies reach their highest average values, and the oscillations become more pronounced, reflecting greater thermal agitation and the possible onset of lattice instability. The potential energy becomes less negative with increasing temperature, implying partial weakening of interatomic interactions. The temperature profile in Fig. 19(d) confirms consistent thermal behavior, where higher set temperatures produce broader fluctuations but maintain equilibrium around their respective mean values.

Fig. 20 illustrates the variation of total energy (T.E), kinetic energy (K.E), potential energy (P.E), and temperature (T) with time for Tl_2CeBr_6 at different temperatures, 300 K, 600 K, and 900 K, over a simulation period of 50 ps. Fig. 20(a)–(c) shows the energy profiles, while panel Fig. 17(d) presents the temperature fluctuations. At 300 K, Fig. 20(a), the system exhibits relatively stable energy oscillations with moderate kinetic and total energy values and a potential energy of around -40 kcal mol^{-1}, indicating structural stability. As the temperature increases to 600 K, Fig. 20(b), both K.E. and T.E rise, showing higher

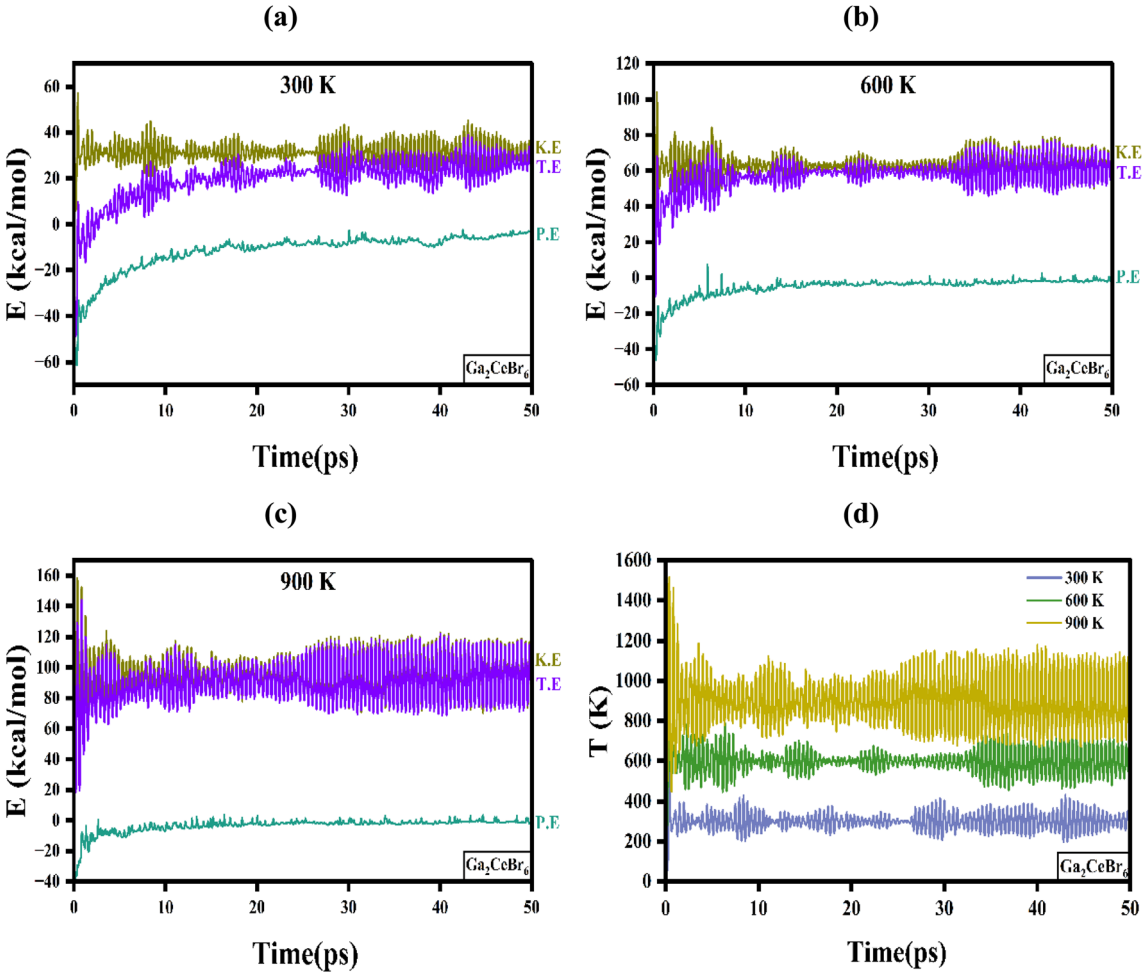

Fig. 16 Time evolution of potential, kinetic, and total energy for Ga_2CeBr_6 double perovskite at (a) 300 K, (b) 600 K, (c) 900 K, and (d) temperature variation over time.

fluctuation amplitudes, whereas P.E slightly shifts toward less negative values, reflecting increased atomic vibrations.

At 900 K, Fig. 17(c), kinetic and total energies reach their highest values, and fluctuations become more pronounced, suggesting enhanced atomic motion and thermal agitation. The temperature *vs.* time plot Fig. 17(d) confirms that Tl_2CeBr_6 maintains near-equilibrium average temperatures around 300 K, 600 K, and 900 K, respectively, though oscillations widen with rising temperature.

3.10. Phonon analysis

Phonon dispersion analysis is a key tool to investigate the vibrational and dynamical stability of materials.[93]

The phonon spectra indicate whether a crystal structure is stable: the absence of imaginary (negative) frequencies confirms dynamical stability, while the presence of such frequencies may signal lattice instabilities or soft phonon modes.[94] Fig. 21 presents the phonon dispersion curves for six Ce-based halide double perovskites plotted along the high-symmetry *K*-points (X–R–M–Γ–R) with frequency (THz) as a function of wave vector: (a) Ga_2CeCl_6, (b) Ga_2CeBr_6, (c) In_2CeCl_6, (d) In_2CeBr_6, (e) Tl_2CeCl_6, and (f) Tl_2CeBr_6 double perovskite materials. From the phonon spectra, Ga_2CeCl_6, In_2CeCl_6, and Tl_2CeCl_6 exhibit no negative frequencies across the entire Brillouin zone, confirming their excellent dynamical stability and structurally robust behavior under equilibrium conditions. In contrast, Ga_2CeBr_6, In_2CeBr_6, and Tl_2CeBr_6 display very small negative frequencies near the Γ-point, suggesting the presence of slight lattice instabilities or soft phonon modes. These modes may become stabilized under finite temperature or pressure, or through minor structural relaxation. Comparing the compounds, chloride-based perovskites possess a more rigid lattice and stronger bonding interactions due to the lighter Cl atoms, resulting in higher phonon frequencies and enhanced dynamic stability. Bromide-based compounds, on the other hand, display softer vibrational modes due to the heavier Br atoms, leading to slightly reduced structural robustness.

3.11. Population analysis

Population analysis is a fundamental computational technique in solid-state physics and quantum chemistry, employed to quantify the distribution of electronic charge among atoms in a compound. It provides crucial insight into bonding character,

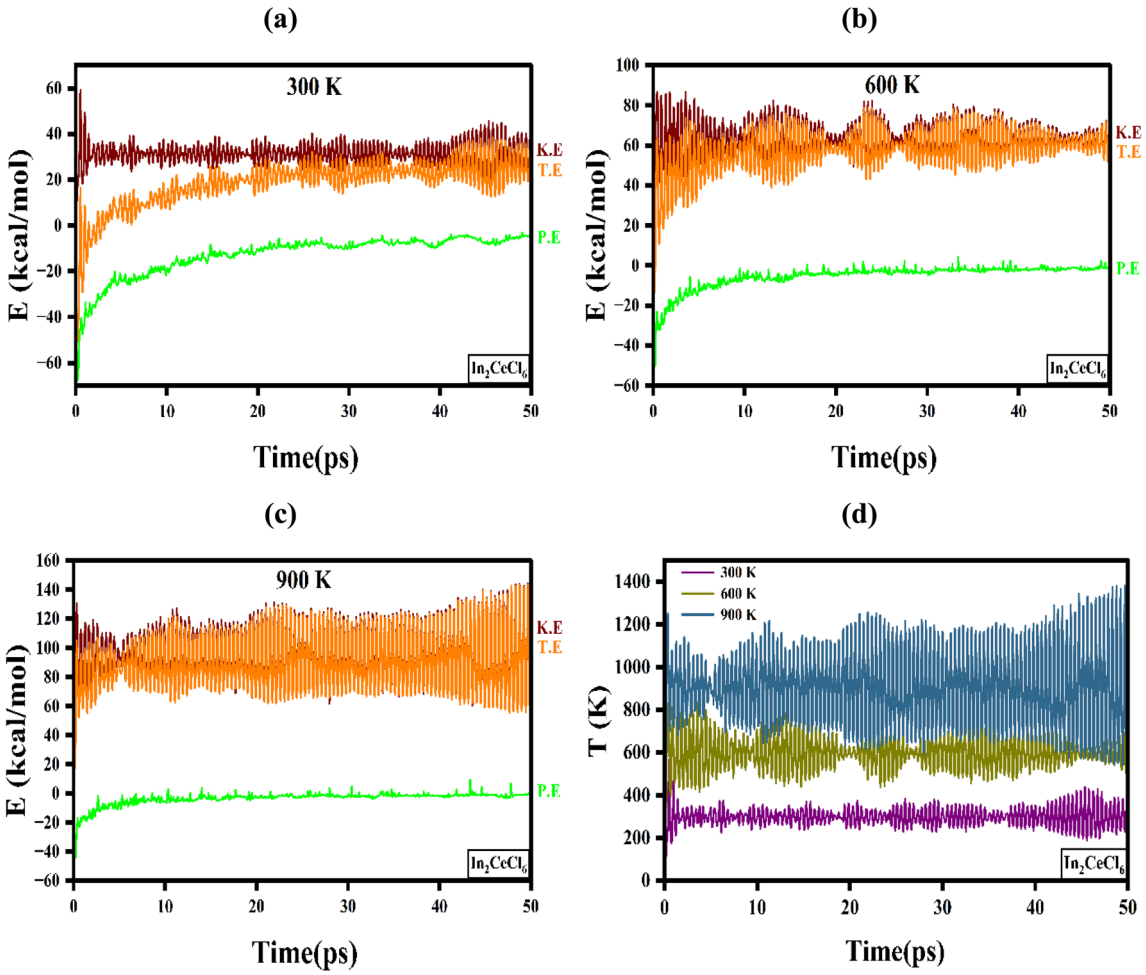

Fig. 17 Time evolution of potential, kinetic, and total energy for In_2CeCl_6 double perovskite at (a) 300 K, (b) 600 K, (c) 900 K, and (d) temperature variation over time.

charge transfer, and the electronic environment of individual species within complex materials. Among the established schemes, Mulliken and Hirshfeld population analyses are widely used.[95,96] Mulliken analysis partitions the electron density based on basis function overlaps, while Hirshfeld analysis assigns electron density relative to reference atomic densities in Table 5. These methods are particularly important for analyzing halide double perovskites such as D_2CeX_6, where mixed ionic-covalent bonding and intricate charge distributions significantly influence optoelectronic and structural properties.

In the present study, population analysis was carried out for a series of D_2CeX_6 compounds. The Mulliken atomic populations, categorized into s, p, d, and f orbitals, reveal substantial trends in Table 5. Notably, Tl atoms exhibit the highest total Mulliken population at 20.24 (in Tl_2CeCl_6), owing to their large atomic size and heavy electron contribution from the 6 s and 6p orbitals, whereas halide anions (Cl and Br) consistently show the lowest, with Br in Tl_2CeBr_6 at just 7.09. Among the cations, Ga atoms in Ga_2CeCl_6 possess the lowest total Mulliken population of 12.25, reflecting the lighter, less electron-rich nature of Ga compared to In and Tl. Cerium (Ce) atoms display significant f-orbital occupancy (1.10 to 1.15), underlining the role of 4f electrons in determining the material's optical and electronic properties. Further, the Mulliken charge change values indicate the extent of electron gain or loss relative to neutral atoms.

The highest positive charge transfer occurs for Tl in Tl_2CeCl_6 (0.76), while the largest electron acceptance is seen in Cl in the same compound (−0.36), reaffirming the ionic nature of halides as electron acceptors. Hirshfeld charge changes, though lower in magnitude, mirror these trends, with Tl showing a maximum of 0.46 and Cl a minimum of −0.19 in Tl_2CeCl_6. Comparing across halide substitutions, replacing Cl with Br generally results in reduced total atomic populations and charge transfers, consistent with Br's lower electronegativity. Similarly, moving from Ga to heavier In and Tl systematically increases total Mulliken populations and charge changes, reflecting the influence of cationic size and electronic configuration on charge distribution. The significance of such population analysis extends to practical applications, as the charge distribution in these double perovskites directly impacts their optical absorption behavior, defect tolerance, and charge carrier dynamics. These factors are critical in determining the performance of perovskite-based materials in applications such as

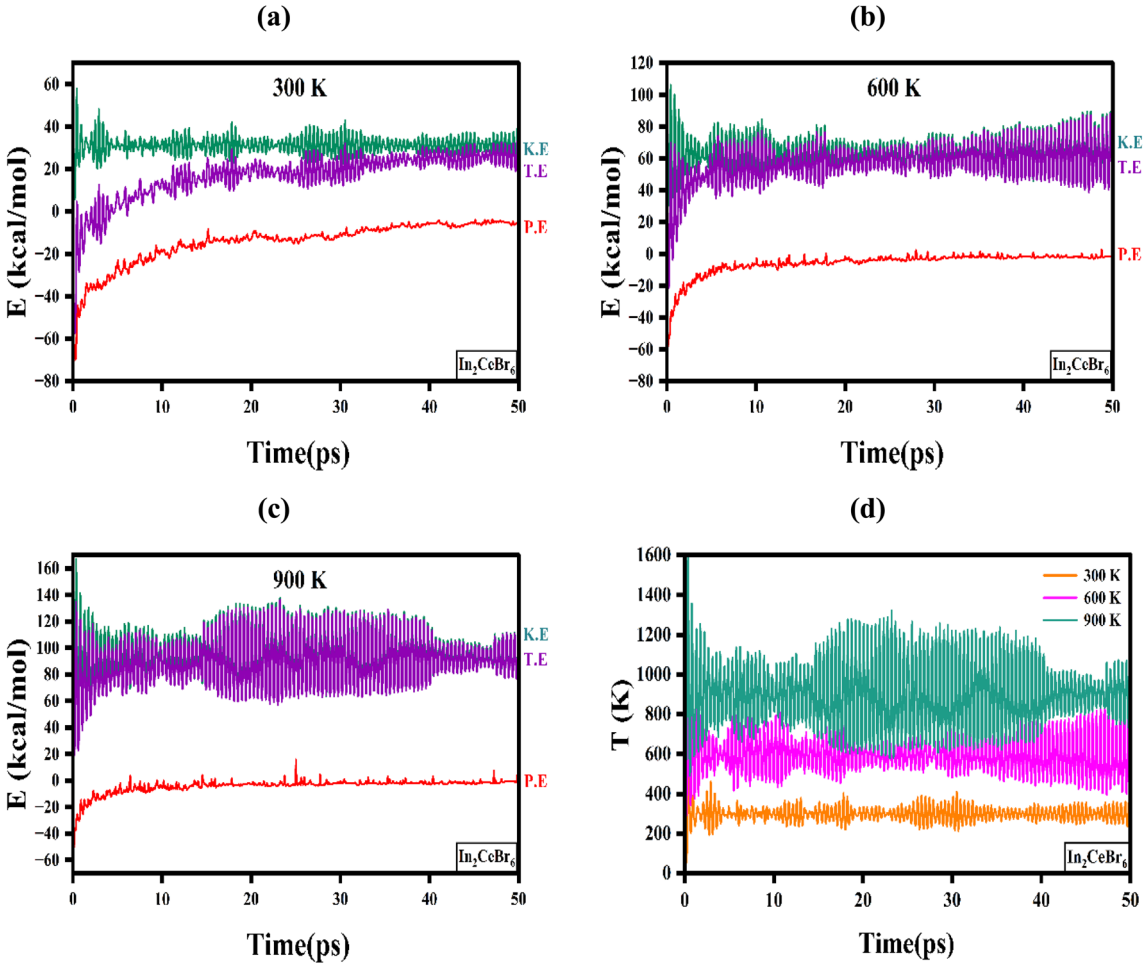

Fig. 18 Time evolution of potential, kinetic, and total energy for In_2CeBr_6 double perovskite at (a) 300 K, (b) 600 K, (c) 900 K, and (d) temperature variation over time.

photovoltaics, X-ray scintillators, and optoelectronic devices. Accurate knowledge of charge transfer tendencies aids in tuning material properties, enabling the rational design of compounds with optimized band gaps, enhanced stability, and superior optoelectronic performance. This comprehensive population analysis thus not only elucidates the fundamental electronic structure of D_2CeX_6 double perovskites but also guides the engineering of advanced materials for future energy and photonic technologies.

4 Device architecture and simulation parameters

In the present work, a series of photovoltaic multilayer structures was systematically designed with the configuration Al/FTO/WS_2/D_2CeX_6/Ni, where D = Ga, In, Tl, and X = Cl, Br. Six distinct device architectures were considered, namely Al/FTO/WS_2/Ga_2CeCl_6/Ni, Al/FTO/WS_2/Ga_2CeBr_6/Ni, Al/FTO/WS_2/In_2CeCl_6/Ni, Al/FTO/WS_2/In_2CeBr_6/Ni, Al/FTO/WS_2/Tl_2CeCl_6/Ni, and Al/FTO/WS_2/Tl_2CeBr_6/Ni. These structures were modeled using SCAPS-1D (Version 3.3.09), which numerically solves the fundamental semiconductor equations. including Poisson's equation and the electron–hole continuity equations under steady-state conditions. This ensures an accurate representation of charge generation, recombination, and transport processes within the device. The schematic layout of the proposed heterostructures is depicted in Fig. 2(b). Each solar cell consists of several functional layers engineered to optimize light absorption and charge carrier extraction. The aluminum (Al) front contact (work function: 4.20 eV) serves as the transparent conductive electrode, while the fluorine-doped tin oxide (FTO) layer acts as an additional transparent conductor, enabling efficient light transmission into the active layers. An n-type WS_2 electron transport layer (ETL) is introduced to facilitate selective electron extraction and minimize interfacial recombination losses. The D_2CeX_6 perovskite absorber layer functions as the primary photoactive medium, where incident photons are absorbed to generate electron–hole pairs. Finally, the nickel (Ni) back contact (work function: 5.22 eV) provides efficient hole collection and establishes an ohmic interface with the absorber. Nickel was deliberately selected as the back electrode because of its favorable combination of properties, including high electrical conductivity, excellent interfacial adhesion, chemical stability, and significantly lower cost

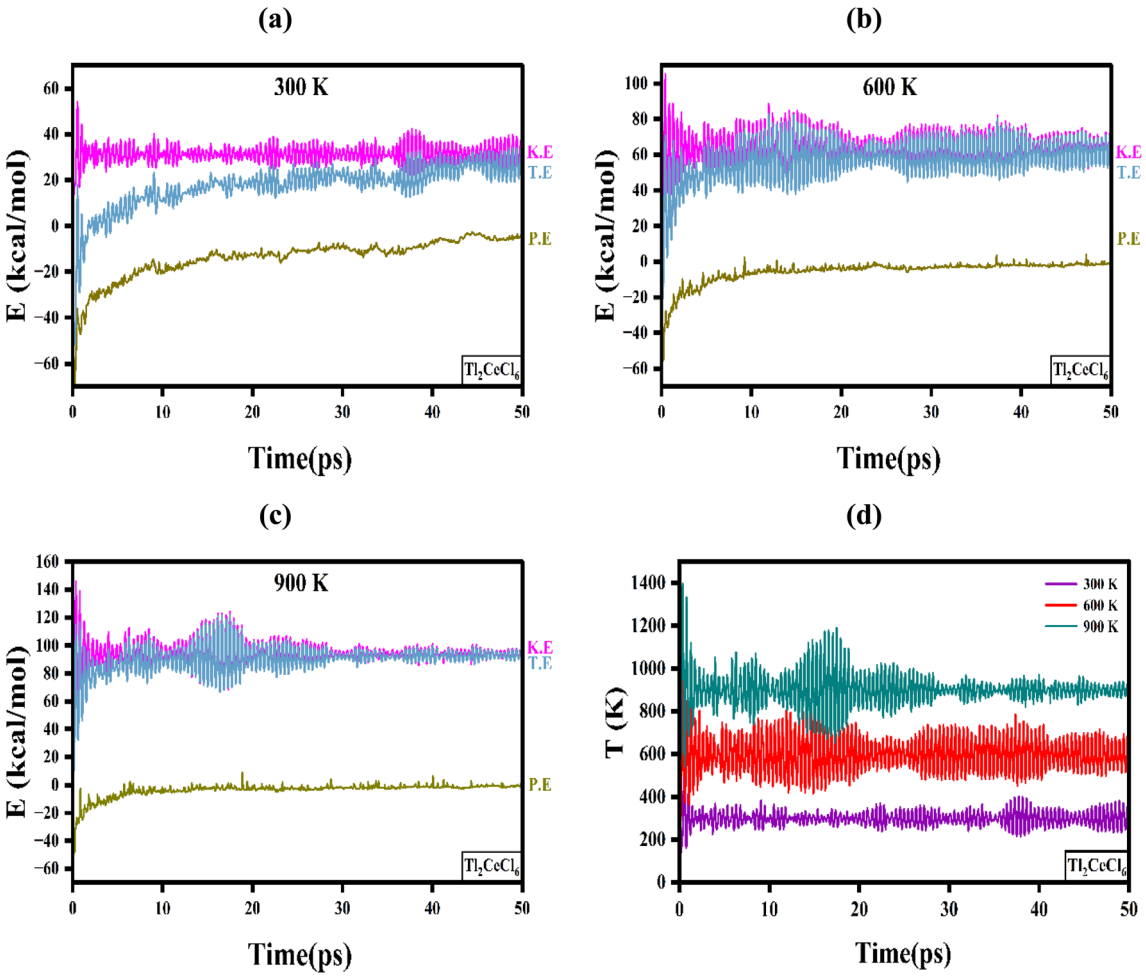

Fig. 19 Time evolution of potential, kinetic, and total energy for Tl_2CeCl_6 double perovskite at (a) 300 K, (b) 600 K, (c) 900 K, and (d) temperature variation over time.

compared to noble metals such as gold or platinum. These attributes make Ni a practical and economically viable choice for scalable perovskite solar cell fabrication.

Table 6 lists the material and structural parameters employed to configure the SCAPS-1D simulation architecture for the studied D_2CeX_6 (D = Ga, In, Tl; X = Cl, Br) double perovskite solar cells. The layer thickness is set at 50 nm for the transparent conducting oxide (FTO) and electron transport layer (WS_2), while the absorber layer is 800 nm, providing adequate optical absorption while minimizing recombination losses. The band gap (E_g) values, ranging from 0.859 eV (In_2CeBr_6) to 3.6 eV (FTO), define the spectral absorption range, with the perovskites covering a broad portion of the visible-near-infrared region for effective photon harvesting. Relative dielectric permittivity (ε_r) values between 3.36 and 13.60 influence the electrostatic screening of charge carriers, directly impacting exciton dissociation and defect tolerance. The electron affinity (χ), varying from 3.950 eV (WS_2) to 7.660 eV (In_2CeBr_6), determines band alignment at interfaces, which is crucial for efficient carrier transport and reduced energy barriers.

The effective density of states (N_V, N_C) for the valence and conduction bands, in the range of 1.429×10^{19}–1.492×10^{19} cm^{-3} (N_V) and 2.460×10^{19}–2.980×10^{19} cm^{-3} (N_C) for perovskites, influences carrier concentration and recombination dynamics. Doping concentrations are assigned such that the FTO and WS_2 layers have a donor density (N_D) of 1×10^{18} cm^{-3} to ensure high conductivity, while the absorber layers are lightly p-type doped ($N_A = 1 \times 10^{17}$ cm^{-3}) to facilitate charge separation. Hole mobility (μ_h) values for the absorbers range from 60 to 69 cm^2 V^{-1} s^{-1}, and electron mobility (μ_n) from 35 to 46 cm^2 V^{-1} s^{-1}, supporting balanced charge transport and minimizing space-charge buildup. The defect density (N_t), fixed at 1×10^{14} cm^{-3} for all layers, represents a moderate trap concentration to reflect realistic fabrication conditions while avoiding excessive recombination losses. Collectively, these parameters ensure that the simulated device reflects realistic material properties, enabling accurate prediction of optoelectronic performance and providing insight into how halide (Cl, Br) and A-site cation (Ga, In, Tl) substitutions influence solar cell efficiency.

This interface defect analysis in Table 7 is significant because the WS_2/absorber junction plays a critical role in determining overall solar cell efficiency, particularly in double perovskite-based devices like D_2CeX_6. Interface defects can act as recombination centers, trapping photogenerated carriers

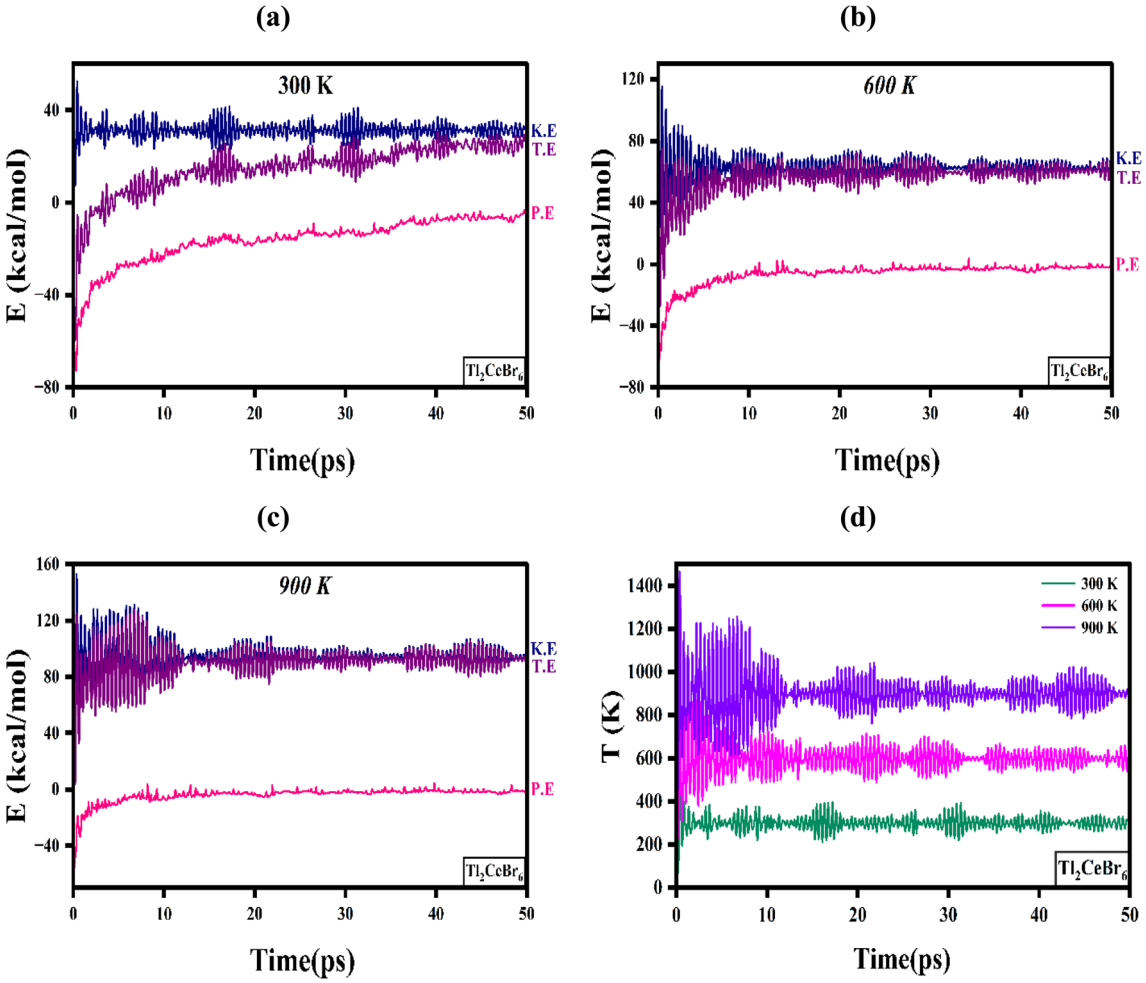

Fig. 20 Time evolution of potential, kinetic, and total energy for In_2CeBr_6 double perovskite at (a) 300 K, (b) 600 K, (c) 900 K, and (d) temperature variation over time.

before they contribute to the photocurrent, which reduces the open-circuit voltage (V_{OC}), short-circuit current density (J_{SC}), and ultimately the power conversion efficiency (PCE).[97] By quantifying parameters such as capture cross-section, defect type, and defect density, the simulation can realistically model the carrier recombination behavior at the heterojunction.

Table 7 summarizes the interface defect parameters used in the SCAPS-1D simulations for the heterojunctions between the electron transport layer (WS_2) and the absorber layers Ga_2CeCl_6, Ga_2CeBr_6, In_2CeCl_6, In_2CeBr_6, Tl_2CeCl_6, and Tl_2CeBr_6. For all interfaces, the capture cross-section for both electrons and holes is set at 1×10^{-19} cm^2, representing a relatively low probability of carrier trapping, which helps to minimize interface recombination losses. The defect type is assigned as neutral, indicating that these traps do not possess a fixed positive or negative charge state, thereby reducing the likelihood of strong coulombic scattering. The total defect density is maintained at 1×10^{11} cm^{-2} for all combinations, corresponding to a moderate but realistic level of interface states that could arise from lattice mismatch or imperfections at the WS_2/absorber junction. Such parameter uniformity across the Ga, In, and Tl-based D_2CeX_6 double perovskite absorbers ensures a controlled comparison of their intrinsic optoelectronic performance, allowing any variations in simulated device efficiency to be attributed primarily to the absorber material properties rather than interface quality differences.

4.1. Band diagram

This analysis presents a comprehensive study of the energy band alignment for six perovskite absorber layers, Ga_2CeCl_6 (Fig. 22(a)), Ga_2CeBr_6 (Fig. 22(b)), In_2CeCl_6 (Fig. 22(c)), In_2CeBr_6 (Fig. 22(d)), Tl_2CeCl_6 (Fig. 22(e)), and Tl_2CeBr_6 (Fig. 15(f)) within the simulated solar cell architectures. Understanding the relative positions of the conduction band minimum (CBM), valence band maximum (VBM), and quasi-Fermi levels is essential for evaluating charge carrier generation, separation, and transport efficiency. By mapping these energy levels across the device thickness, the study reveals how the intrinsic bandgap and band offsets of each material dictate the overall photovoltaic response.[98] Fig. 22 illustrates the comparative energy band diagrams of the six absorber materials; each modeled with a thickness of 0.80 μm. In each subfigure, the conduction band edge (E_C), valence band edge (E_V), electron quasi-Fermi level (F_n), and hole quasi-Fermi level (F_p) are plotted as functions of

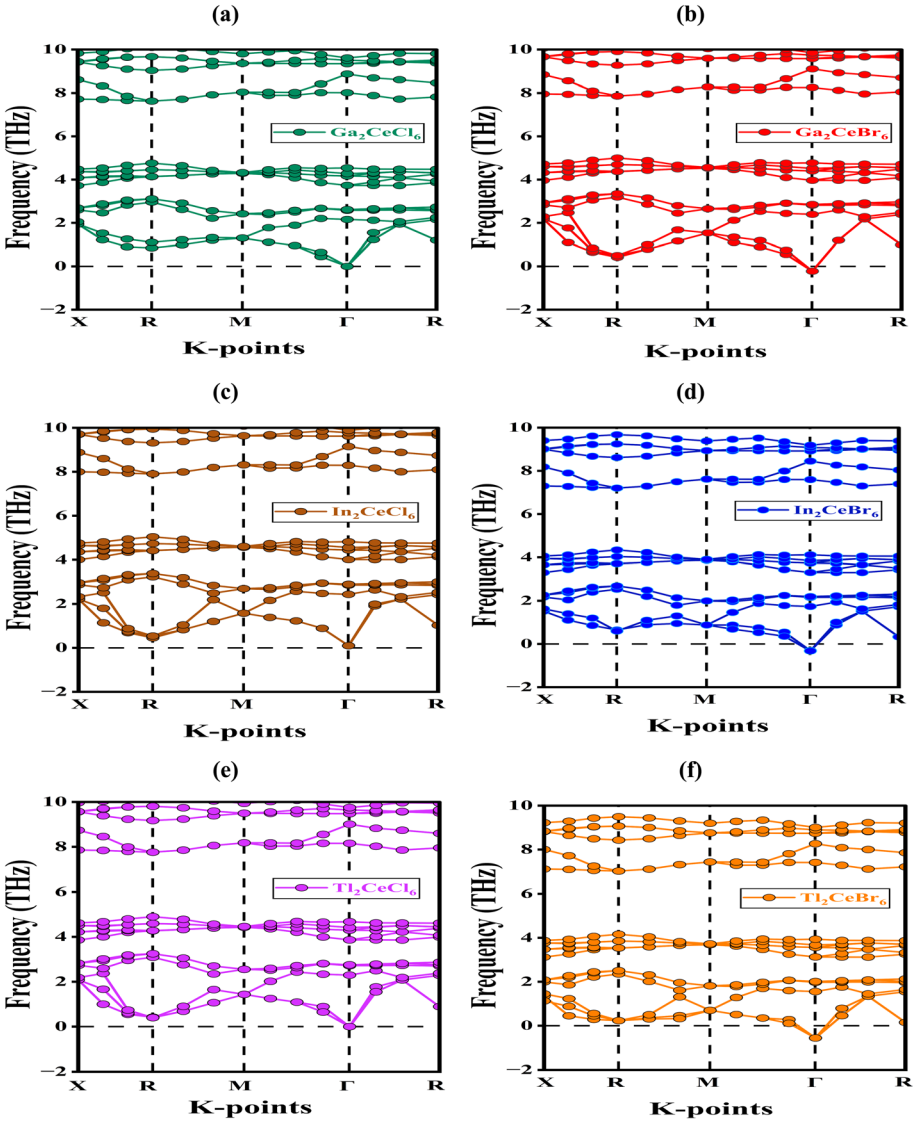

Fig. 21 Phonon dispersion curves of Ce-based (a) Ga_2CeCl_6, (b) Ga_2CeBr_6, (c) In_2CeCl_6, (d) In_2CeBr_6, (e) Tl_2CeCl_6, and (f) Tl_2CeBr_6 double perovskites materials.

depth, providing a clear visualization of the bandgap and alignment characteristics. The results indicate systematic variations, where Ga_2CeCl_6 and Tl_2CeCl_6 exhibit the widest band gaps of 1.778 eV and 1.735 eV, respectively, while their bromide counterparts show reduced values of 1.276 eV and 1.304 eV. Similarly, In_2CeCl_6 possesses a bandgap of 1.550 eV, which decreases to 0.855 eV in In_2CeBr_6. These trends demonstrate that chloride-containing compounds generally feature wider band gaps with sharper conduction–valence band separations, leading to higher photon energy thresholds and making them favorable for achieving high open-circuit voltages. In contrast, bromide-based analogues exhibit narrower band gaps, enabling stronger absorption in the longer-wavelength region of the solar spectrum but also raising the possibility of enhanced recombination losses.

While the transport layers (FTO/WS_2) maintain consistent band offsets across all structures, the internal energy level positioning within the absorbers varies considerably, which directly affects charge separation, extraction, and recombination dynamics. Overall, Ga_2CeCl_6 and Tl_2CeCl_6 are promising candidates for high-V_{OC} applications due to their wider band gaps and reduced thermalization losses, whereas In_2CeBr_6, with the narrowest band gap, offers strong potential for near-infrared light harvesting but requires careful optimization to suppress recombination and enhance device performance.

4.2. Optimizing absorber thickness for device performance

Analyzing the thickness-dependent behavior of Ce-based halide perovskite solar cells is vital for optimizing absorber layer design. In this study, the influence of absorber thickness on photovoltaic parameters PCE, FF, J_{SC}, and V_{OC} was systematically evaluated for Ga_2CeCl_6, Ga_2CeBr_6, In_2CeCl_6, In_2CeBr_6, Tl_2CeCl_6, and Tl_2CeBr_6. The results show that optimizing absorber thickness improves photon utilization across the solar spectrum while mitigating carrier recombination losses.[99]

Table 5 Mulliken and Hirshfeld charge analysis of different atoms of D_2CeX_6 (where D = Ga, In, Tl, and X = Cl, Br) double perovskites

Compound	Change spilling	Species	Mulliken atomic populations					Mulliken change	Hirshfeld change
			s	p	d	f	Total		
Ga_2CeCl_6	0.14%	Ga	1.93	0.32	10.00	0.00	12.25	0.75	0.48
		Ce	2.30	6.34	1.63	1.10	11.38	0.62	0.20
		Cl	1.95	5.40	0.00	0.00	7.35	−0.35	−0.19
Ga_2CeBr_6	0.10%	Ga	2.11	0.39	10.00	0.00	12.50	0.50	0.45
		Ce	2.45	6.63	1.73	1.13	11.94	0.06	0.12
		Br	1.85	5.33	0.00	0.00	7.18	−0.18	−0.17
In_2CeCl_6	0.14%	In	1.93	0.32	10.00	0.00	12.25	0.75	0.45
		Ce	2.30	6.34	1.63	1.09	11.37	0.63	0.21
		Cl	1.95	5.41	0.00	0.00	7.36	−0.36	−0.19
In_2CeBr_6	0.16%	In	2.23	0.59	10.00	0.00	12.82	0.18	0.29
		Ce	2.43	6.47	1.89	1.15	11.94	0.06	0.07
		Br	1.81	5.26	0.00	0.00	7.07	−0.07	−0.11
Tl_2CeCl_6	0.11%	Tl	3.93	6.31	10.00	0.00	20.24	0.76	0.46
		Ce	2.30	6.34	1.63	1.09	11.36	0.64	0.21
		Cl	1.95	5.41	0.00	0.00	7.36	−0.36	−0.19
Tl_2CeBr_6	0.13%	Tl	4.16	6.59	10.00	0.00	20.75	0.25	0.30
		Ce	2.44	6.47	1.89	1.15	11.95	0.05	0.07
		Br	1.82	5.27	0.00	0.00	7.09	−0.09	−0.11

Excessive thickness, however, restricts carrier diffusion and enhances bulk recombination,[100] whereas insufficient thickness reduces light absorption and lowers photocurrent generation.[101] These findings reveal material-specific trade-offs among absorption, carrier transport, and recombination, offering critical insights for designing efficient Ce-based halide perovskite absorbers. As illustrated in Fig. 23(a and b), increasing the absorber thickness from 0.2 μm to 0.8 μm leads to a pronounced improvement in both PCE and J_{SC}. This enhancement originates from more efficient photon absorption within the active layer, which increases carrier generation, while the diffusion length remains sufficient to suppress significant recombination losses. Within this range, the PCE and J_{SC} increase from 13.7% to 20.63% and 13.67 to 20.05 mA cm^{-2} for Ga_2CeCl_6, 17.18% to 24.34% and 17.74 to 25.35 mA cm^{-2} for In_2CeCl_6, 14.10% to 20.67% and 13.21 to 19.33 mA cm^{-2} for Tl_2CeCl_6, 19.44% to 25.29% and 25.70 to 35.07 mA cm^{-2} for Ga_2CeBr_6, 15.39% to 16.43% and 41.60 to 51.25 mA cm^{-2} for In_2CeBr_6, and 17.21% to 24.13% and 23.11 to 32.37 mA cm^{-2} for Tl_2CeBr_6. When the thickness is further increased from 0.8 μm to 1.4 μm, the performance shows only limited gains. At this stage, nearly all incident photons within the absorber's absorption range are harvested, so PCE and J_{SC} improvements primarily reflect marginal reductions in surface recombination. The highest efficiencies at 1.4 μm are 21.51% and 20.90 mA cm^{-2} (Ga_2CeCl_6), 24.92% and 26.17 mA cm^{-2} (In_2CeCl_6), 21.47% and 20.09 mA cm^{-2} (Tl_2CeCl_6), 25.36% and 35.90 mA cm^{-2} (Ga_2CeBr_6), 24.82% and 33.39 mA cm^{-2} (Tl_2CeBr_6), and 15.41% and 51.67 mA cm^{-2} (In_2CeBr_6). Beyond 1.4 μm, further thickness increases up to 2.1 μm yield negligible improvements, as optical absorption saturates and longer carrier transport pathways enhance bulk recombination.

The V_{OC} remains nearly constant across thickness variations, emphasizing that it is primarily dictated by the intrinsic bandgap and defect-related recombination of the material rather than absorber thickness. The simulated V_{OC} values are 1.259 V (Ga_2CeCl_6), 1.163 V (In_2CeCl_6), 1.297 V (Tl_2CeCl_6), 0.913 V (Ga_2CeBr_6), 0.497 V (In_2CeBr_6), and 0.969 V (Tl_2CeBr_6). These values confirm that Cl-based absorbers favor higher V_{OC}, whereas Br-based compounds favor higher J_{SC}, consistent with bandgap-dependent photovoltaic theory. Regarding the FF, increasing thickness from 0.2 μm to 0.8 μm causes slight

Table 6 Configurational parameters for the simulated device architecture

Parameters	FTO	WS_2	Ga_2CeCl_6	Ga_2CeBr_6	In_2CeCl_6	In_2CeBr_6	Tl_2CeCl_6	Tl_2CeBr_6
Thickness (nm)	50	50	800	800	800	800	800	800
Band gap, E_g (eV)	3.6	2.2	1.733	1.273	1.550	0.859	1.755	1.364
Dielectric permittivity, $\in_r$	10	13.60	3.520	3.750	3.650	3.360	3.540	3.36
Electron affinity, χ (eV)	4.5	3.950	4.472	5.410	4.560	7.660	4.280	7.160
V_B effective density of states, N_V (cm^{-3})	1.8×10^{19}	2.2×10^{18}	1.450×10^{19}	1.492×10^{19}	1.489×10^{19}	1.440×10^{19}	1.478×10^{19}	1.429×10^{19}
C_B effective density of states, N_C (cm^{-3})	2×10^{18}	1.8×10^{19}	2.460×10^{19}	2.476×10^{19}	2.980×10^{19}	2.930×10^{19}	2.504×10^{19}	2.483×10^{19}
Donor density, N_D (cm^{-3})	1×10^{18}	1×10^{18}	0	0	0	0	0	0
Acceptor density, N_A (cm^{-3})	0	0	1×10^{17}	1×10^{17}	1×10^{17}	1×10^{17}	1×10^{17}	1×10^{17}
Hole mobility, μ_h ($cm^2\ V^{-1}\ s^{-1}$)	20	100	65	60	67	65	69	69
Electron mobility, μ_n ($cm^2\ V^{-1}\ s^{-1}$)	100	100	40	35	37	42	46	46
Total defect density, N_t (cm^{-3})	1×10^{14}	1×10^{14}	1×10^{14}	1×10^{14}	1×10^{14}	1×10^{14}	1×10^{14}	1×10^{14}

Table 7 The simulated design of WS_2/D_2CeX_6 solar cells' specific interface input parameters

Interfaces	Capture cross section: Electrons/holes (cm^2)	Defect type	Total interface defect density (cm^{-2})
WS_2/Ga_2CeCl_6	1×10^{-19}	Neutral	1×10^{11}
WS_2/Ga_2CeBr_6	1×10^{-19}	Neutral	1×10^{11}
WS_2/In_2CeCl_6	1×10^{-19}	Neutral	1×10^{11}
WS_2/In_2CeBr_6	1×10^{-19}	Neutral	1×10^{11}
WS_2/Tl_2CeCl_6	1×10^{-19}	Neutral	1×10^{11}
WS_2/Tl_2CeBr_6	1×10^{-19}	Neutral	1×10^{11}

decreases for most materials, reflecting the interplay between increased series resistance and enhanced absorption. FF decreases from 82.67% to 81.75% (Ga_2CeCl_6), 82.39% to 82.55% (In_2CeCl_6), 83.26% to 82.44% (Tl_2CeCl_6), 80.13% to 79.03% (Ga_2CeBr_6), 71.35% to 64.56% (In_2CeBr_6), and 77.03% to 76.91% (Tl_2CeBr_6). When the thickness is further increased to 2.3 μm, FF stabilizes for most absorbers, except In_2CeBr_6, which decreases from 64.56% to 58.82% due to increased bulk recombination and resistive losses. Overall, these results demonstrate that both cation choice (Ga, In, Tl) and anion substitution (Cl *vs.* Br) significantly influence thickness-dependent performance: Br-based perovskites achieve higher J_{SC} owing to narrower band gaps, while Cl-based perovskites retain higher V_{OC}, and the optimal thickness for balancing light absorption, carrier transport, and recombination generally lies at 0.8 μm for all materials.

4.3. Optimizing total defect density for device performance

As depicted in Fig. 24(a and b), varying the effect of varying defect density from 10^{11} to 10^{18} cm^{-3} on the photovoltaic parameters PCE, FF, J_{SC}, and V_{OC} of Ga_2CeCl_6, In_2CeCl_6, Tl_2CeCl_6, Ga_2CeBr_6, In_2CeBr_6, and Tl_2CeBr_6-based solar cells. This is commonly referred to as defect tolerance analysis, which quantifies how device efficiency responds to intrinsic material imperfections. Defect-tolerant materials exhibit minimal performance degradation even at higher defect concentrations, an essential attribute for the fabrication of scalable, cost-effective, and durable perovskite solar technologies. Our results reveal a progressive degradation in all photovoltaic parameters with increasing defect density. At low defect levels (10^{11} to 10^{14} cm^{-3}), performance remains nearly unchanged, with only slight reductions due to enhanced Shockley–Read–Hall (SRH) recombination and trap-assisted non-radiative processes that slightly shorten carrier lifetimes. For instance, when the acceptor concentration increases, only slight variations are observed in the photovoltaic parameters. The PCE, FF, J_{SC}, and V_{OC} values remain almost stable for all D_2CeX_6 compounds, showing minimal fluctuations within a narrow range. For example, Ga_2CeCl_6 exhibits a minor change from 19.9% to 20.6% (PCE) and 1.26 to 1.26 V (V_{OC}), while In_2CeCl_6 and Tl_2CeCl_6 show similarly small differences. A comparable trend is seen for the bromide systems, where Ga_2CeBr_6, In_2CeBr_6, and Tl_2CeBr_6 display only slight declines or adjustments in efficiency, current, and voltage.

However, when the defect density exceeds 10^{14} cm^{-3}, a noticeable performance degradation occurs. At a higher defect density of around 10^{18} cm^{-3}, this decline becomes severe, with significant reductions observed in all key photovoltaic parameters. The PCE, FF, J_{SC}, and V_{OC} values drop sharply for each material, indicating increased non-radiative recombination and hindered charge transport. These steep declines stem from the fact that higher defect concentrations introduce deep-level trap states, which increase carrier recombination rates, lower carrier diffusion lengths, and reduce quasi-Fermi level splitting, thereby strongly suppressing both V_{OC} and J_{SC}. Overall, the analysis highlights that cation (Ga → In → Tl) and anion (Cl → Br) substitutions significantly affect defect tolerance, with Cl-based compounds generally showing better stability against defect-induced performance loss compared to their Br counterparts. This insight provides critical guidance for material selection in designing defect-tolerant halide double perovskite solar cells.

4.4. Effect of shallow acceptor density of the absorber layer

Fig. 26(a and b) demonstrates how changes in the shallow acceptor density (N_A) from 10^{13} to 10^{20} cm^{-3} influence key photovoltaic metrics PCE, FF, J_{SC}, and V_{OC}. This trend is observed in Ga_2CeCl_6, In_2CeCl_6, Tl_2CeCl_6, Ga_2CeBr_6, In_2CeBr_6, and Tl_2CeBr_6 solar cells. The shallow acceptor density denotes the number of shallow-level acceptor impurities per unit volume in a semiconductor, which governs its p-type (D_2CeX_6) conductivity by generating holes as charge carriers. While higher N_A values enhance hole concentration and initially improve device performance, excessive doping leads to stronger recombination losses and reduced efficiency.[102] An optimal range of 10^{15}–10^{17} cm^{-3} achieves the best trade-off between carrier generation and recombination, making shallow acceptor density a key factor in the design of high-efficiency photovoltaic and electronic devices.[103] As shown in Fig. 26(a and c), increasing the acceptor concentration (N_A) from 10^{13} to 10^{17} cm^{-3} leads to a steady improvement in both V_{OC} and FF across all D_2CeX_6-based solar cells. Within this range, each compound exhibits a noticeable rise in voltage and fill factor, indicating enhanced charge separation and reduced recombination. Further increasing N_A up to around 1020 cm^{-3} continues to improve these parameters, reaching their maximum values for all materials. However, an excessively high N_A may also promote additional recombination losses. Generally, a moderate doping

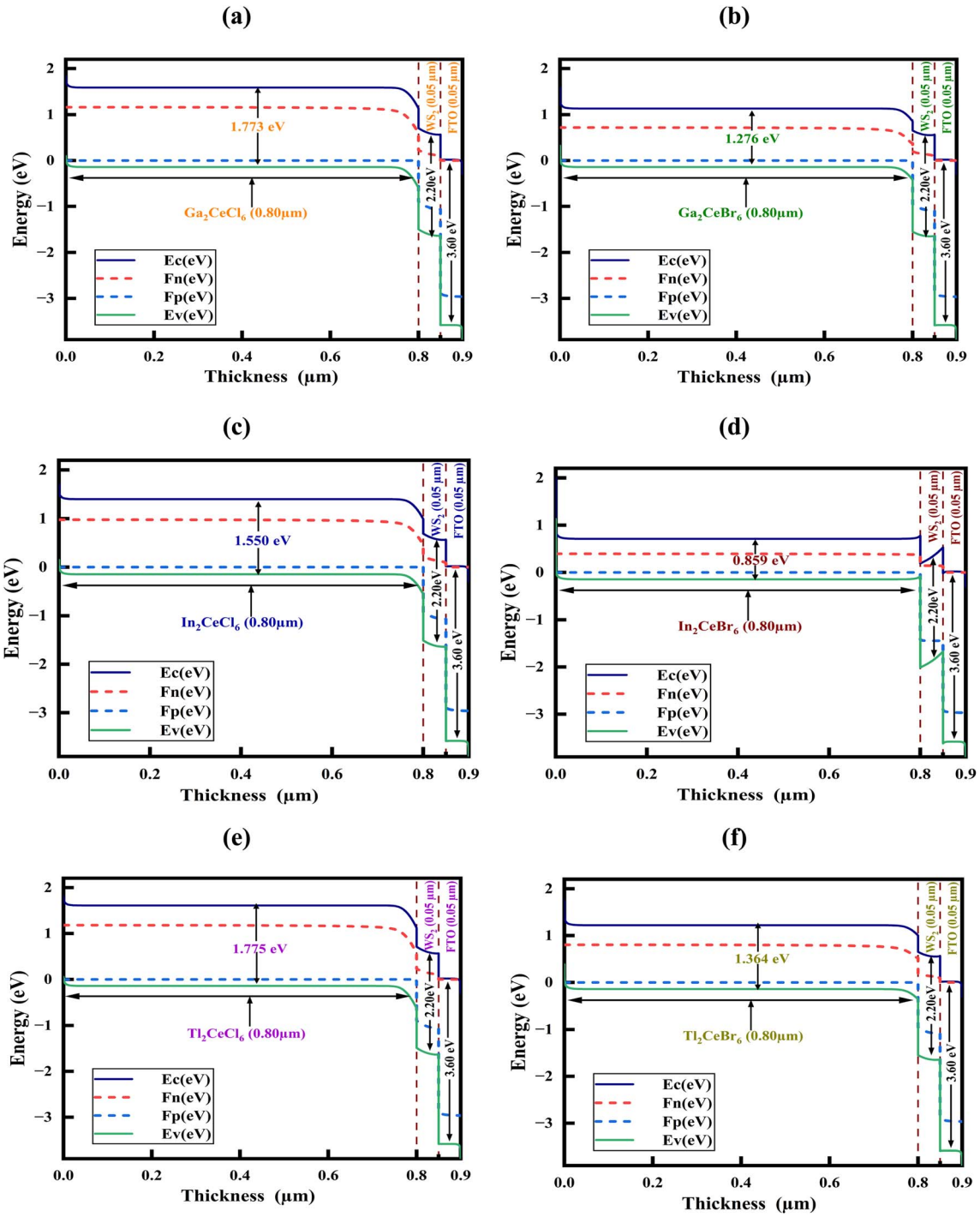

Fig. 22 Energy band diagrams of (a) Ga_2CeCl_6, (b) Ga_2CeBr_6, (c) In_2CeCl_6, (d) In_2CeBr_6, (e) Tl_2CeCl_6, and (f) Tl_2CeBr_6 double perovskite absorber layers in the simulated solar cell structures.

level of about 10^{17} cm^{-3} offers the most balanced performance, ensuring optimal carrier transport and device efficiency.

As illustrated in Fig. 25(b), increasing the N_A from 10^{13} to 10^{17} cm^{-3} results in nearly constant J_{SC} values for most of the investigated D_2CeX_6 solar cells, except for In_2CeBr_6. The J_{SC} remains approximately 20.05 mA cm^{-2} (Ga_2CeCl_6), 25.36 mA cm^{-2} (In_2CeCl_6), 19.33 mA cm^{-2} (Tl_2CeCl_6), 35.07 mA cm^{-2} (Ga_2CeBr_6), and 32.37 mA cm^{-2} (Tl_2CeBr_6), while In_2CeBr_6 shows a slight increase from 50.35 to 51.25 mA cm^{-2} over the same N_A range. With further doping up to 10^{20} cm^{-3}, J_{SC} values largely remain constant, except for slight reductions observed in Ga_2CeCl_6 (18.70 mA cm^{-2}) and Tl_2CeCl_6 (16.53 mA cm^{-2}). This indicates that J_{SC} in these perovskite systems is less sensitive to shallow acceptor density variations compared to V_{OC} and FF, suggesting that carrier collection efficiency remains largely

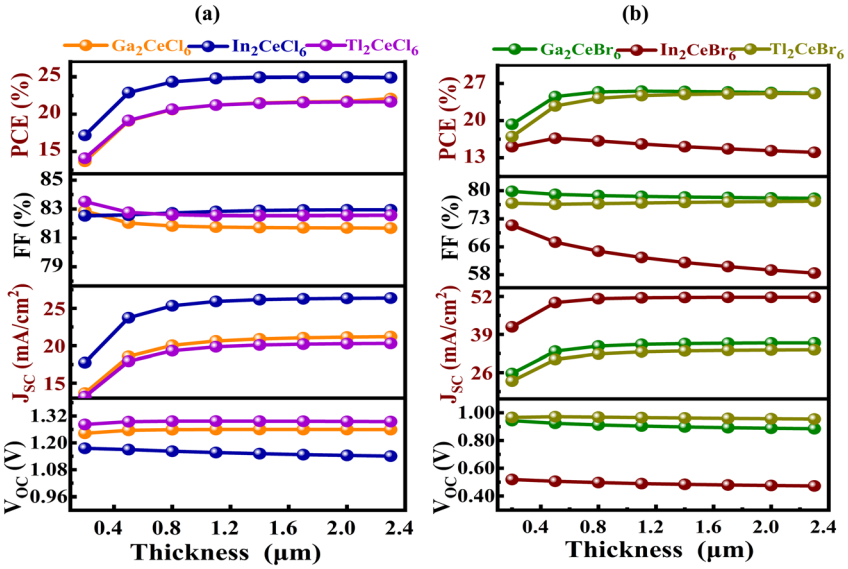

Fig. 23 Optimization of absorber layer thickness on PCE, FF, J_{SC}, and V_{OC} for (a) D_2CeCl_6 and (b) D_2CeBr_6 double perovskite materials.

unaffected by excess doping, except in specific cases where recombination effects begin to dominate.

As illustrated in Fig. 25(d), the variation of PCE exhibits a similar trend to that of V_{OC} and FF. When the acceptor concentration (N_A) increases to around 10^{17} cm^{-3}, the PCE values show a notable improvement for both chloride- and bromide-based devices. Upon further increasing N_A to approximately 10^{20} cm^{-3}, the efficiencies rise even higher across all configurations, with Ga_2CeBr_6 and Tl_2CeBr_6 achieving the best performance. This overall enhancement with increasing N_A suggests improved charge transport and reduced recombination losses, leading to more efficient device operation. These results indicate that moderate N_A of 10^{17} cm^{-3} significantly enhances device performance by improving carrier concentration and transport, while excessive doping continues to raise PCE but may approach saturation due to increased recombination losses. The optimized N_A for V_{OC}, J_{SC}, FF, and PCE was found to be 10^{17} cm^{-3} for all the studied D_2CeX_6 materials. At this N_A value, the devices achieve a balanced enhancement of carrier concentration and transport, resulting in maximum overall photovoltaic performance before recombination losses from excessive doping become significant.

4.5. Impact on temperature-dependent photovoltaic performance

This temperature-dependent photovoltaic performance analysis is important because it reveals how different D-site cations (Ga,

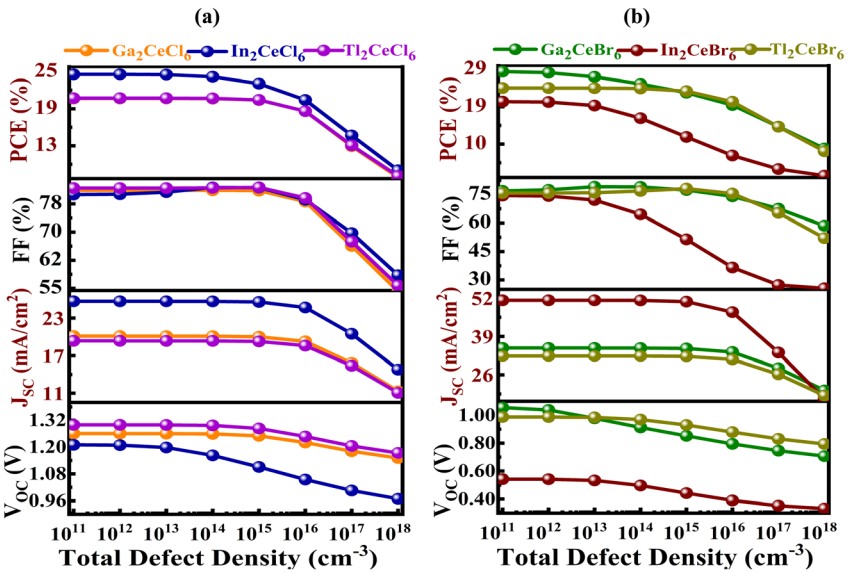

Fig. 24 Optimization of total defect density on PCE, FF, J_{SC}, and V_{OC} for (a) D_2CeCl_6 and (b) D_2CeBr_6 double perovskite materials.

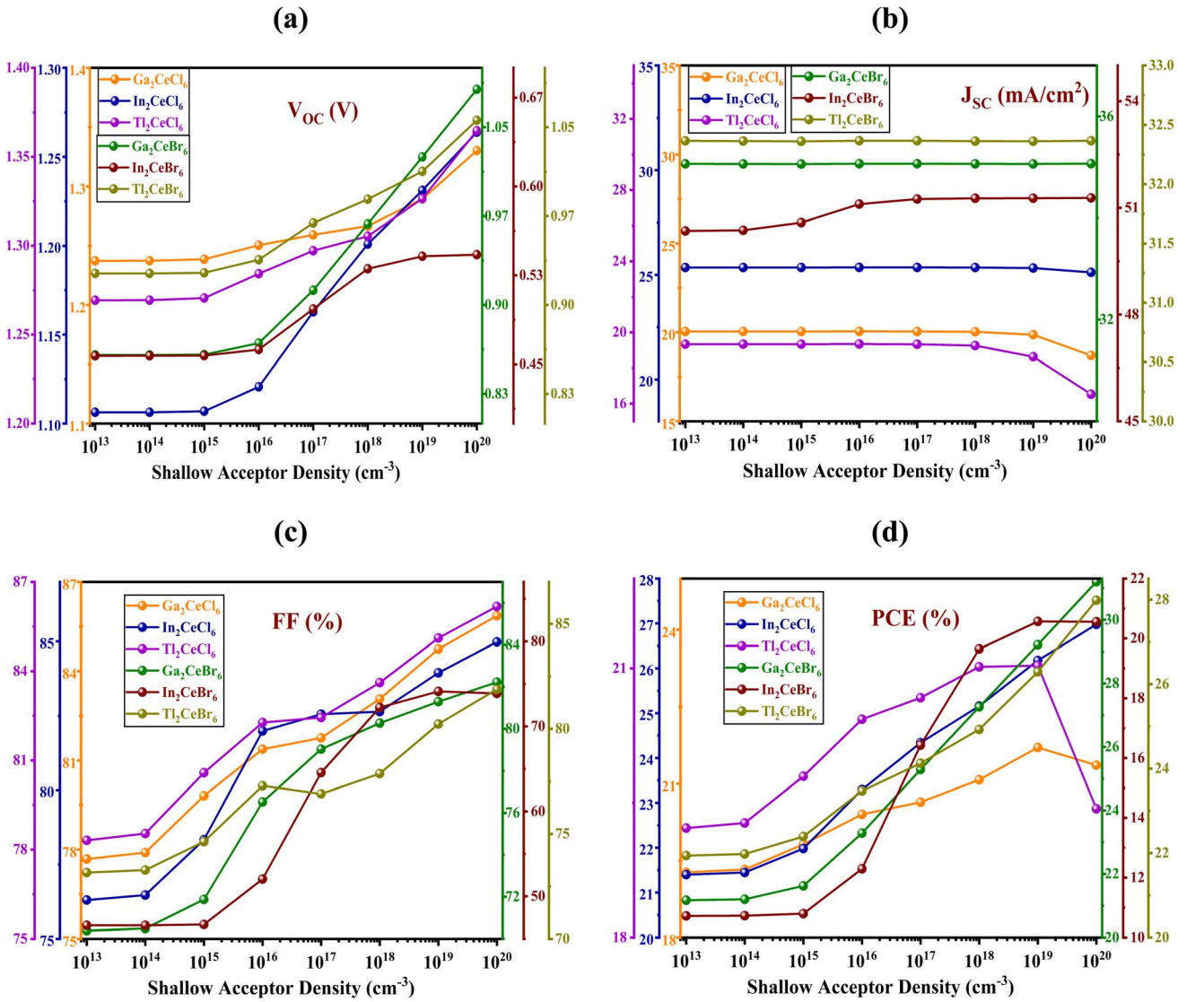

Fig. 25 Optimization of shallow acceptor density on (a) V_{OC}, (b) J_{SC}, (c) FF, and (d) PCE for D_2CeX_6 double perovskite materials.

In, Tl) and halide anions (Cl, Br) influence the thermal stability and efficiency retention of double perovskite solar cells under varying operating conditions. By examining the trends in V_{OC}, J_{SC}, FF, and PCE across a broad temperature range, it becomes possible to identify materials that maintain high output and stability despite thermal stress, an essential requirement for real-world solar energy deployment where temperature fluctuations are inevitable. Such insights not only highlight the trade-offs between voltage, current generation, and charge transport in different compositions but also pinpoint the most promising candidates, like Tl-based compounds, for achieving high efficiency and durability, guiding the design of next-generation, thermally robust photovoltaic devices. Fig. 26 presents the temperature-dependent photovoltaic performance parameters of six double perovskite halides: Ga_2CeCl_6, In_2CeCl_6, Tl_2CeCl_6, Ga_2CeBr_6, In_2CeBr_6, and Tl_2CeBr_6, displayed across four figures: Fig. 26(a). V_{OC}, Fig. 26(b). J_{SC}, Fig. 26(c). FF, and Fig. 26(d). PCE. Fig. 26(a), V_{OC} decreases consistently with increasing temperature for all materials, with Ga_2CeCl_6 and Tl_2CeCl_6 showing the highest initial values at low temperatures, while bromide-based compounds generally exhibit lower V_{OC} due to their narrower band gaps. In Fig. 26(b), J_{SC} slightly increases with temperature for bromides (notably Tl_2CeBr_6) but remains relatively stable for chlorides, reflecting enhanced carrier generation in narrower-bandgap materials at higher temperatures. Fig. 26(c) shows FF values slightly decreasing with temperature, with Tl-based compounds maintaining higher FF across the range, indicating better charge extraction stability.

Finally, Fig. 26(d) reveals that PCE declines with rising temperature for all materials, with Tl_2CeCl_6 and Tl_2CeBr_6 retaining superior efficiencies compared to Ga- and In-based counterparts, suggesting that Tl-containing perovskites offer a better balance between voltage, current, and charge transport. This analysis is crucial because it reveals how intrinsic material properties and halide composition govern the thermal stability and operational performance of perovskite solar cells, aiding in identifying the most thermally robust candidates for high-temperature photovoltaic applications.

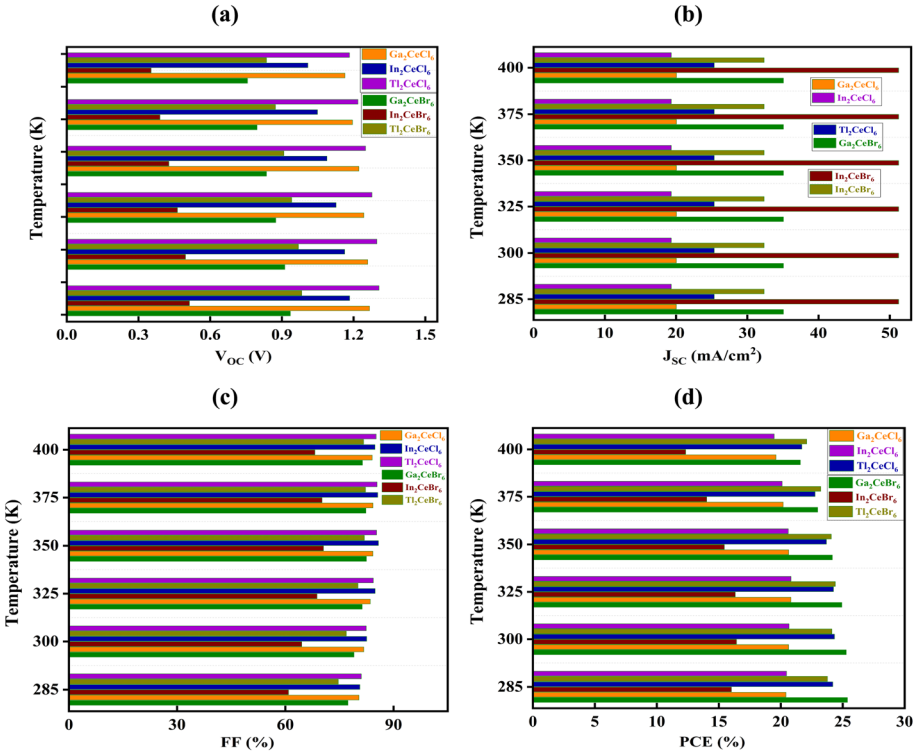

Fig. 26 Temperature-dependent photovoltaic parameters of (a) V_{OC}, (b) J_{SC}, (c) FF, and (d) PCE of D_2CeX_6-based solar cells.

4.6. JV and QE properties

A thorough examination of the quantum efficiency (QE) and current density–voltage (J–V) characteristics is indispensable for elucidating the optoelectronic behavior of photovoltaic devices. These parameters function as critical diagnostic indicators, providing quantitative insights into the efficiency of photon absorption, carrier photogeneration, and charge transport dynamics.[104] The QE spectrum delineates the proportion of incident photons converted into collected charge carriers, thereby serving as a direct measure of spectral responsivity. In parallel, the J–V profile describes the current density as a function of applied bias, enabling a rigorous evaluation of key device performance metrics.[105]

Fig. 27(a) and (b) depict the J–V and QE characteristics of D_2CeX_6-based double perovskite solar cells. The optimized Al/FTO/WS_2/D_2CeX_6/Au configuration was obtained using carefully tuned parameters: an absorber thickness of 800 nm, a total defect density of 10^{14} cm^{-3}, and a shallow acceptor density of 10^{17} cm^{-3}. As shown in Fig. 27(a), the simulated J–V curves yield J_{SC} of 20.05, 25.35, 19.33, 35.07, 51.25, and 32.37 mA cm^{-2} for Ga_2CeCl_6, In_2CeCl_6, Tl_2CeCl_6, Ga_2CeBr_6, In_2CeBr_6, and Tl_2CeBr_6, respectively, under zero voltage. With increasing voltage, J_{SC} initially remains nearly constant but then decreases sharply to zero at the corresponding V_{OC} of 1.259, 1.163, 1.297, 0.913, 0.497, and 0.969 V. This reduction in photocurrent at higher voltage is primarily attributed to carrier saturation and recombination effects. As shown in Fig. 27(b), the simulated QE

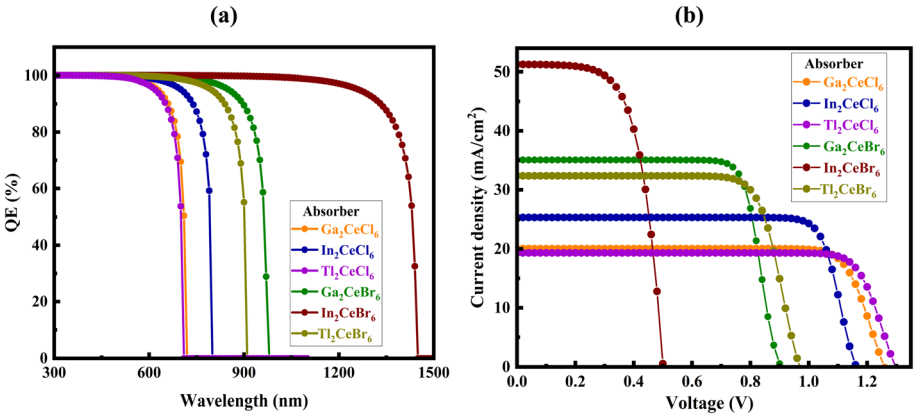

Fig. 27 (a) J–V characteristics and (b) QE spectra of D_2CeX_6-based double perovskite solar cells.

spectra exhibit an initial maximum value of nearly 100% for all compositions at short wavelengths, indicating excellent photon-to-carrier conversion efficiency under strong absorption conditions. With increasing wavelength, QE remains relatively constant over the visible region but decreases sharply to zero at the respective cutoff wavelengths of 720, 800, 710, 980, 1450, and 910 nm for Ga_2CeCl_6, In_2CeCl_6, Tl_2CeCl_6, Ga_2CeBr_6, In_2CeBr_6, and Tl_2CeBr_6, respectively. These cutoff positions are strongly correlated with the optical band gaps, where larger band gaps (*e.g.*, Ga_2CeCl_6, Tl_2CeCl_6) correspond to shorter cutoff wavelengths, while smaller band gaps (*e.g.*, In_2CeBr_6) extend absorption into the near-infrared region. The observed trends highlight the role of cationic substitution (Ga → In → Tl) and halide exchange (Cl → Br) in tailoring the optical response. Replacing Cl with Br reduces the band gap, red-shifting the absorption edge and enhancing long-wavelength QE, thereby improving light-harvesting capability. Similarly, the choice of the trivalent cation influences orbital hybridization and band dispersion, which governs carrier generation and transport. These theoretical insights confirm that compositional engineering in D_2CeX_6 double perovskites offers a viable pathway to optimize the spectral response and photovoltaic performance of the devices.

4.7. Device overall performance

Optimization of the device parameters was carried out with an absorber thickness of 800 nm, a total defect density of 10^{14} cm^{-3}, and a shallow acceptor density of 10^{17} cm^{-3}. Under these optimized conditions, the photovoltaic parameters were measured as follows: Al/FTO/WS_2/Ga_2CeCl_6/Au delivered a V_{OC} of 1.259 V, a J_{SC} of 20.05 mA cm^{-2}, an FF of 81.75%, and a PCE of 20.64%. Al/FTO/WS_2/In_2CeCl_6/Au exhibited a V_{OC} of 1.163 V, a J_{SC} of 25.35 mA cm^{-2}, an FF of 82.55%, and a PCE of 24.34%. As shown in Fig. 28, the Al/FTO/WS_2/Tl_2CeCl_6/Au device achieved the highest V_{OC} (~1.29 V) but moderate J_{SC} (~19 mA cm^{-2}), resulting in a PCE of about 20.6%. In contrast, the bromide-based cells showed lower V_{OC} but higher J_{SC} values. Among them, Al/FTO/WS_2/Ga_2CeBr_6/Au reached the best efficiency (~25.3%) with a balanced V_{OC} (~0.91 V) and J_{SC} (~35 mA cm^{-2}). The In-based device exhibited the highest J_{SC} (~51 mA cm^{-2}) but lowest V_{OC} (~0.50 V), giving a moderate PCE (~16.4%), while Al/FTO/WS_2/Tl_2CeBr_6/Au showed a well-balanced performance (~24.1% PCE). Overall, chloride systems favor higher voltage, whereas bromide systems enhance current generation.

A comparative evaluation highlights distinct trends associated with cationic and anionic substitutions. The chloride-based systems (Ga_2CeCl_6, In_2CeCl_6, Tl_2CeCl_6) generally provide higher V_{OC} owing to their wider band gaps, although at the cost of reduced photocurrent. Among them, Ga_2CeBr_6 achieves the highest efficiency of 25.29%, reflecting a favorable balance between voltage and current density. The bromide-based systems (Ga_2CeBr_6, In_2CeBr_6, Tl_2CeBr_6), in contrast, show red-shifted absorption edges that enhance photocurrent but simultaneously lower the voltage due to narrower band gaps. In_2CeCl_6 demonstrates the best overall performance with

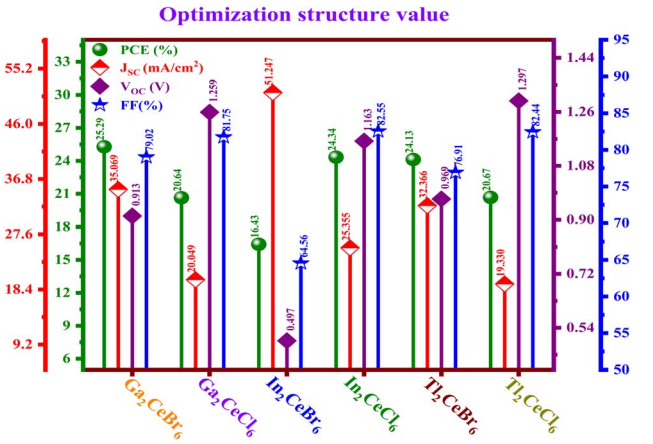

Fig. 28 Comparison of V_{OC}, J_{SC}, FF, and PCE for Ga_2CeBr_6, Ga_2CeCl_6, In_2CeBr_6, In_2CeCl_6, Tl_2CeBr_6, and Tl_2CeCl_6 absorber-based solar cells.

an efficiency of 24.34%, arising from a well-balanced combination of V_{OC} and J_{SC}. In_2CeBr_6, despite delivering the highest photocurrent of 51.25 mA cm^{-2}, suffers from severe voltage loss, restricting its efficiency to only 16.43%. Tl_2CeBr_6 exhibits intermediate behavior, with an efficiency of 24.13%, reflecting the role of cation substitution in fine-tuning electronic structure and carrier transport. These findings underscore that chloride-based compounds are favorable for higher voltage stability, while bromide substitution enhances photocurrent generation. Among the studied materials, Ga_2CeBr_6 emerges as the most promising candidate, demonstrating that halide exchange combined with careful cation selection can effectively optimize photovoltaic performance in D_2CeX_6 double perovskite solar cells.

4.8. Limitations of the study

This study has several limitations. First, the initial DOS calculations employed relatively large Gaussian smearing values, which increased numerical broadening and led to inconsistencies between the DOS and band structure bandgap. In future work, this issue can be explored in greater depth to further improve the reliability of the results. Nevertheless, selecting an appropriate smearing parameter remains essential for accurately determining the electronic structure.

Second, in the earlier version, the convergence criteria used for the phonon dispersion calculations were not sufficiently strict, and relatively small supercells were employed. As a result, the acoustic phonon frequencies at the Γ-point did not appear as zero, and slight imaginary modes were observed in some bromine-containing compounds. Although these issues have been significantly corrected in the revised calculations, very small negative or near-zero frequencies still appear near the Γ-point for Ga_2CeBr_6, In_2CeBr_6, and Tl_2CeBr_6. These features indicate possible soft phonon modes or minor lattice instabilities. In the future, the stability of these Br-based compounds may be enhanced through pressure, temperature effects, or doping. Finally, the phonon calculations were performed within the harmonic approximation at 0 K. Anharmonic effects, thermal stabilization, and pressure-dependent behavior were

not considered and may influence the dynamical stability of the bromine-containing compounds.

5 Conclusion

Based on the structural, electronic, optical, and molecular dynamics analyses, the overall findings highlight the promising stability and functionality of the investigated materials. This study presented a comprehensive first-principles and device-level investigation of lead-free, vacancy-ordered halide double perovskites D_2CeX_6 (D = Ga, In, Tl; X = Cl, Br) for solar energy applications. All compounds crystallize in a stable cubic $Fm\bar{3}m$ phase, with negative formation enthalpies and tolerance factors confirming thermodynamic and structural stability. Halide substitution (Cl → Br) enlarged lattice constants, narrowed band gaps, and improved visible-light absorption, while D-site cation variation (Ga → In → Tl) tuned bonding strength, charge distribution, and mechanical robustness. Electronic structure analysis revealed tunable direct and indirect band gaps (0.859 to 3.632 eV), with Ce-4f and halogen-p orbitals dominating near the band edges, supporting efficient charge-transfer transitions. Optical evaluations confirmed strong UV-visible absorption coefficients ($\alpha > 10^4$ cm^{-1}), high refractive indices, and large dielectric constants, especially in In_2CeBr_6 and Tl_2CeBr_6, making them promising for optoelectronics and photodetectors. Mechanical analysis showed ductile behavior across the series. Tl_2CeBr_6 had the highest bulk, shear, and Young's moduli, while In_2CeBr_6 exhibited excellent isotropy and flexibility suitable for stable thin-film or flexible solar cells. Phonon dispersion spectra confirm full dynamical stability for Ga_2CeCl_6, In_2CeCl_6, and Tl_2CeCl_6, while minor soft modes in bromides are expected to be stabilized at finite temperatures. Importantly, molecular dynamics simulations performed at 300 K, 600 K, and 900 K under NPT conditions demonstrate that all studied materials maintain thermal stability across a wide temperature range, highlighting their robustness for practical applications. Device simulations using SCAPS-1D demonstrated high photovoltaic potential. The device parameters were optimized with an absorber thickness of 800 nm, a total defect density of 10^{14} cm^{-3}, and a shallow acceptor density of 10^{17} cm^{-3}. In_2CeCl_6 reached an efficiency of 24.34%, while Ga_2CeBr_6 achieved the highest PCE of 25.29% due to a favorable trade-off between voltage and current. Bromide compounds enhanced photocurrent through band-gap narrowing, whereas chloride compounds delivered higher voltages. D_2CeX_6 family exhibits stability, tunable optoelectronic response, and strong photovoltaic performance, with In_2CeCl_6, Tl_2CeBr_6, and Ga_2CeBr_6 emerging as the most promising absorbers. These findings provide valuable guidance for experimental synthesis and compositional engineering of sustainable, lead-free perovskites for next-generation solar cells and optoelectronic technologies.

Ethical approval

The manuscript's authors agree that there are no research involving human participants, human data or tissue, or animal subjects.

Author contributions

Rifat Rafiu, Md. Sakib Hasan Saikot, Md. Azizur Rahman, Imtiaz Ahamed Apon, Imtiaz Ahmed Talukder: methodology, validation, software, conceptualization, investigation, formal analysis, data curation, visualization, writing – original draft, and review and editing. Karim KRIAA, N. Sfina, Mohd Taukeer Khan, S. AlFaify, Noureddine Elboughdiri: investigation, validation, software, formal analysis, data curation, writing – original draft, and review and editing.

Conflicts of interest

The authors have no conflicts of interest.

Data availability

Data will be made available on reasonable request.

Acknowledgements

The authors extend their appreciation to the Deanship of Research and Graduate Studies at King Khalid University for funding this work through the Large Research Project under grant number RGP2/119/46.

References

1 T. M. Razykov, C. S. Ferekides, D. Morel, E. Stefanakos, H. S. Ullal and H. M. Upadhyaya, *Sol. Energy*, 2011, **85**, 1580–1608.
2 G. T. Chala and S. M. Al Alshaikh, *Energies*, 2023, **16**, 7919.
3 A. Machín and F. Márquez, *Materials*, 2024, **17**, 1165.
4 J. Y. Kim, J.-W. Lee, H. S. Jung, H. Shin and N.-G. Park, *Chem. Rev.*, 2020, **120**, 7867–7918.
5 G. G. Njema and J. K. Kibet, *Int. J. Photoenergy*, 2023, **2023**, 1–35.
6 G. Schileo and G. Grancini, *J. Mater. Chem. C*, 2021, **9**, 67–76.
7 M. Faizan, X. Wang, S. A. M. Abdelmohsen, K. C. Bhamu, S. Sappati, A. Laref, N. Muhammad, M. Mushtaq, A. M. M. Abdelbacki and R. Khenata, *Energy Fuels*, 2022, **36**, 7065–7074.
8 A. E. Maughan, A. M. Ganose, M. M. Bordelon, E. M. Miller, D. O. Scanlon and J. R. Neilson, *J. Am. Chem. Soc.*, 2016, **138**, 8453–8464.
9 Y. Cai, W. Xie, H. Ding, Y. Chen, K. Thirumal, L. H. Wong, N. Mathews, S. G. Mhaisalkar, M. Sherburne and M. Asta, *Chem. Mater.*, 2017, **29**, 7740–7749.
10 A. Jabar, S. Idrissi and L. Bahmad, *J. Electroceram.*, 2025, **53**, 186–198.
11 T. Kaatz and M. Marcovich, *Acta Crystallogr.*, 1966, **21**, 1011.
12 J. Du, J. Shi, W. Guo, S. Liu, Y. He, C. Tian, Y. Zhu and H. Zhong, *Phys. Rev. B*, 2021, **104**, 235206.
13 R. K. Pingak, A. Z. Johannes, N. U. J. Hauwali, H. L. Sianturi, A. Warsito, L. A. S. Lapono, F. R. Ngana, J. Tarigan and A. Wahid, *Comput. Condens. Matter.*, 2024, **41**, e00979.

14 M. K. Butt, M. Yaseen, J. Iqbal, A. S. Altowyan, A. Murtaza, M. Iqbal and A. Laref, *J. Phys. Chem. Solids*, 2021, **154**, 110084.
15 M. Zhuravleva, K. Yang, H. Rothfuss and C. L. Melcher, in *IEEE Nuclear Science Symposuim & Medical Imaging Conference*, IEEE, Knoxville, TN, 2010, pp. 1296–1299.
16 R. K. Pingak, A. Harbi, S. Bouhmaidi, F. Nitti, M. Moutaabbid, L. Setti, A. Z. Johannes and N. U. J. Hauwali, *Chem. Phys.*, 2024, **584**, 112348.
17 A. A. AlObaid, S. A. Rouf, T. I. Al-Muhimeed, A. I. Aljameel, S. Bouzgarrou, H. H. Hegazy, T. Alshahrani, G. Nazir, A. Mera and Q. Mahmood, *Mater. Chem. Phys.*, 2021, **271**, 124876.
18 N. V. Skorodumova, R. Ahuja, S. I. Simak, I. A. Abrikosov, B. Johansson and B. I. Lundqvist, *Phys. Rev. B:Condens. Matter Mater. Phys.*, 2001, **64**, 115108.
19 T. Tang, X. Diao and Y. Tang, *Chem. Phys. Lett.*, 2023, **826**, 140678.
20 A. Hermann and D. Kurzydłowski, *Crystals*, 2019, **9**, 463.
21 S. M. Woodley and R. Catlow, *Nat. Mater.*, 2008, **7**, 937–946.
22 A. Hermann and D. Kurzydłowski, *Crystals*, 2019, **9**, 463.
23 S. H. Mir, N. A. Teli and B. Want, *Sol. Energy*, 2025, **298**, 113705.
24 I. A. Apon, Md. R. Hasan, R. Rafiu, R. Kawsar, Md. S. Hasan Saikot, Md. A. Hossain, Md. A. Rahman, K. KRIAA, N. Elboughdiri, Q. Mohsen, M. T. Khan and A. A. Alshihri, *J. Inorg. Organomet. Polym. Mater.*, 2025, DOI: **10.1007/s10904-025-03957-4**.
25 N. Elboughdiri, B. B. Sarkar, Md. A. Rahman, A. M. A. Adam, Md. H. Rahman, J. R. Rajabathar, Q. Mohsen, A. A. Alshihri, M. T. Khan, Md. S. Uddin and S. Saidi, *New J. Chem.*, 2025, **49**, 14529–14552.
26 M. H. Rahman, F. Ahmed, N. Elboughdiri, K. KRIAA, M. S. Uddin, M. A. Rahman, M. N. Tasnim, I. Boukhris, A. Akremi, J. R. Rajabathar and M. T. Khan, *Polyhedron*, 2025, **280**, 117676.
27 M. S. I. Ria, M. A. Rahman, A. Ghosh, M. M. Billah, D. Das, N. Elboughdiri, A. M. Alsuhaibani, Q. Mohsen, M. S. Refat, I. Boukhris and M. T. Khan, *J. Phys. Chem. Solids*, 2025, **207**, 112955.
28 D. R. Hamann, M. Schlüter and C. Chiang, *Phys. Rev. Lett.*, 1979, **43**, 1494–1497.
29 S. Jubayer, R. Boudissa, R. Kawsar, R. Rafiu, M. S. Refat, Md. S. H. Saikot, A. M. Alsuhaibani, Md. A. Rahman, Md. A. Hossain and N. Elboughdiri, *J. Inorg. Organomet. Polym. Mater.*, 2025, DOI: **10.1007/s10904-025-03821-5**.
30 L. Protesescu, S. Yakunin, M. I. Bodnarchuk, F. Krieg, R. Caputo, C. H. Hendon, R. X. Yang, A. Walsh and M. V. Kovalenko, *Nano Lett.*, 2015, **15**, 3692–3696.
31 H. J. Monkhorst and J. D. Pack, *Phys. Rev. B*, 1976, **13**, 5188–5192.
32 P. Wisesa, K. A. McGill and T. Mueller, *Phys. Rev. B*, 2016, **93**, 155109.
33 M. S. Hayat and R. M. A. Khalil, *Solid State Commun.*, 2023, **361**, 115064.
34 J. P. Perdew, K. Burke and M. Ernzerhof, *Phys. Rev. Lett.*, 1996, **77**, 3865–3868.
35 J. Heyd and G. E. Scuseria, *J. Chem. Phys.*, 2004, **121**, 1187–1192.
36 K. Momma and F. Izumi, *J. Appl. Crystallogr.*, 2008, **41**, 653–658.
37 S. Sharma, *Molecular Dynamics Simulation of Nanocomposites Using BIOVIA Materials Studio, Lammps and Gromacs*, Elsevier, 2025.
38 M. Burgelman, P. Nollet and S. Degrave, *Thin Solid Films*, 2000, **361–362**, 527–532.
39 P. A. Markowich, C. A. Ringhofer and C. Schmeiser, *Semiconductor Equations*, Springer Science & Business Media, 2012.
40 W. Van Roosbroeck, *Bell Syst. Tech. J.*, 1950, **29**, 560–607.
41 C. Cercignani, in *The Boltzmann Equation and its Applications*, Springer New York, New York, NY, 1988, vol. 67, pp. 40–103.
42 J. Epp, in *Materials Characterization Using Nondestructive Evaluation (NDE) Methods*, Elsevier, 2016, pp. 81–124.
43 A. A. Bunaciu, E. G. Udriştioiu and H. Y. Aboul-Enein, *Crit. Rev. Anal. Chem.*, 2015, **45**, 289–299.
44 A. Ali, Y. W. Chiang and R. M. Santos, *Minerals*, 2022, **12**, 205.
45 G. E. M. Jauncey, *Proc. Natl. Acad. Sci. U. S. A.*, 1924, **10**, 57–60.
46 R. H. Mitchell, M. D. Welch and A. R. Chakhmouradian, *Mineral. Mag.*, 2017, **81**, 411–461.
47 G. P. Nagabhushana, R. Shivaramaiah and A. Navrotsky, *Proc. Natl. Acad. Sci. U. S. A.*, 2016, **113**, 7717–7721.
48 R. Rafiu, S. Hasan, A. El-Rayyes, I. A. Apon, M. Shkir, M. T. Khan, M. A. Sayed and M. A. Rahman, *J. Phys. Chem. Solids*, 2025, 113126.
49 C. J. Bartel, C. Sutton, B. R. Goldsmith, R. Ouyang, C. B. Musgrave, L. M. Ghiringhelli and M. Scheffler, *Sci. Adv.*, 2019, **5**, eaav0693.
50 C. Shi, C. Yu and W. Zhang, *Angew. Chem.*, 2016, **128**, 5892–5896.
51 R. E. Hummel, *Electronic Properties of Materials*, Springer, New York, 4th edn, 2011.
52 K. M. Gupta and N. Gupta, *Advanced Semiconducting Materials and Devices*, Springer, 2016.
53 J. R. Hook, H. E. Hall and H. E. Hall, *Solid State Physics*, Wiley, Chichester ; New York, 2nd edn, 1991.
54 P. Makkar and N. N. Ghosh, *RSC Adv.*, 2021, **11**, 27897–27924.
55 A. G. Van Der Geest, P. Blaise and N. Richard, *Phys. Rev. B:Condens. Matter Mater. Phys.*, 2012, **86**, 085320.
56 Y. Huang, C. Rong, R. Zhang and S. Liu, *J. Mol. Model.*, 2016, **23**, 3.
57 R. Świsłocka, E. Regulska, J. Karpińska, G. Świderski and W. Lewandowski, *Molecules*, 2019, **24**(14), 2645.
58 A. Mohamed, D. P. Jr. Visco, K. Breimaier and D. M. Bastidas, *ACS Omega*, 2025, **10**, 2799–2808.
59 M. Ratul Hasan, I. A. Apon, Md. Mafidul Islam, J. Y. Al-Humaidi and Md. Rasidul Islam, *Mater. Sci. Eng., B*, 2025, **313**, 117936.
60 Md. R. Hasan, I. A. Apon, Md. M. Islam, A. U. Azad, Md. Solayman and Md. S. Haque, *Mater. Adv.*, 2025, **6**(5), 1794–1821.

61 Md. S. H. Saikot, R. Rafiu, I. Boukris, Md. A. Rahman, I. A. Apon, R. Kawsar, M. T. Khan, H. Etabti, J. Rajabathar and H. Albalawi, *New J. Chem.*, 2025, **49**(39), 17221–17245.
62 R. Gupta, H. Chauhan, V. K. Garg and N. Kataria, in *Sustainable Nanotechnology for Environmental Remediation*, ed. J. R. Koduru, R. R. Karri, N. M. Mubarak and E. R. Bandala, Elsevier, 2022, pp. 199–220.
63 M. A. Ghebouli, K. Bouferrache, F. K. Alanazi, B. Ghebouli and M. Fatmi, *Adv. Theory Simul.*, 2025, **8**, 2400938.
64 M. Hussain, M. Rashid, A. Ali, M. F. Bhopal and A. S. Bhatti, *Ceram. Int.*, 2020, **46**, 21378–21387.
65 Q. Li, L. Zhou, Y. Ge, Y. Ren, J. Zhao, W. Wan, K. Zhang and Y. Liu, *arXiv*, 2019, preprint, arXiv:2411.08528, DOI: 10.48550/arXiv.2411.08528.
66 H. Y. Hisashi Yoshikawa and S. A. Sadao Adachi, *Jpn. J. Appl. Phys.*, 1997, **36**, 6237.
67 W. Wang and L. Qi, *Adv. Funct. Mater.*, 2019, **29**, 1807275.
68 C. Ambrosch-Draxl and J. O. Sofo, *Comput. Phys. Commun.*, 2006, **175**, 1–14.
69 H. J. Lee, M. M. A. Gamel, P. J. Ker, M. Z. Jamaludin, Y. H. Wong and J. P. R. David, *J. Electron. Mater.*, 2022, **51**, 6082–6107.
70 S. Donati, *Photodetectors: Devices, Circuits and Applications*, IEEE Press, Wiley, Hoboken, 2nd edn, revised and expanded., 2021.
71 Md. S. H. Saikot, R. Rafiu, I. A. Apon, A. El-Rayyes, Md. A. Rahman, M. Shkir, Z. Ahmad and R. Marnadu, *RSC Adv.*, 2025, **15**, 39071–39091.
72 I. A. Apon, K. KRIAA, Md. A. Rahman, Md. Alamgir Hossain, C. Maatki, A. A. Assadi and N. Elboughdiri, *RSC Adv.*, 2025, **15**, 40209–40230.
73 Z. Huan, Y. Zheng, K. Wang, Z. Shen, W. Ni, J. Zu and Y. Shao, *J. Mater. Chem. A*, 2024, **12**, 1910–1922.
74 D. Shao, W. Zhu, X. Liu, M. Li, J. Chen, Y.-Y. Sun, G. Xin, J. Lian and S. Sawyer, *ACS Appl. Mater. Interfaces*, 2020, **12**, 43106–43114.
75 L. Solymar, D. Walsh and R. R. A. Syms, *Electrical Properties of Materials*, Oxford university press, OxfordUnited, 9th edn, 2014.
76 M. L. Bortz and R. H. French, *Appl. Phys. Lett.*, 1989, **55**, 1955–1957.
77 F. Flory, *J. Nanophotonics*, 2011, **5**, 052502.
78 A. A. I. Abd-Elmageed, S. M. Ibrahim, A. Bourezgui and A. F. Al-Hossainy, *New J. Chem.*, 2020, **44**, 8621–8637.
79 M. Nabi and D. C. Gupta, *RSC Adv.*, 2019, **9**, 15852–15867.
80 P. E. Batson and J. Silcox, *Phys. Rev. B:Condens. Matter Mater. Phys.*, 1983, **27**, 5224–5239.
81 M. W. Barsoum and M. Radovic, *Annu. Rev. Mater. Res.*, 2011, **41**, 195–227.
82 S. J. Schön, in *Physical Properties of Rocks*, ed. J. H. Schön, Elsevier, 2011, vol. 8, pp. 149–243.
83 P. Giannozzi, S. De Gironcoli, P. Pavone and S. Baroni, *Phys. Rev. B:Condens. Matter Mater. Phys.*, 1991, **43**, 7231–7242.
84 M. Ali, Z. Bibi, M. W. Younis, H. Huang, M. Raheel, U. Afzal, R. A. Alshgari and S. Mohammad, *J. Inorg. Organomet. Polym. Mater.*, 2025, **35**(5), 3313–3324.
85 B. Ghebouli, M. A. Ghebouli, H. Choutri, M. Fatmi, T. Chihi, L. Louail, A. Bouhemadou, S. Bin-Omran, R. Khenata and H. Khachai, *Mater. Sci. Semicond. Process.*, 2016, **42**, 405–412.
86 M. Jamal, S. Jalali Asadabadi, I. Ahmad and H. A. Rahnamaye Aliabad, *Comput. Mater. Sci.*, 2014, **95**, 592–599.
87 M. Born, *Math. Proc. Cambridge Philos. Soc.*, 1940, **36**, 160–172.
88 I. A. Apon, M. D. Ratul Hasan, I. A. Ovi and F. Tuz-Zahra, *AIP Adv.*, 2024, **14**, 065126.
89 I. A. Apon, M. D. Ratul Hasan, I. A. Ovi and F. Tuz-Zahra, *AIP Adv.*, 2024, **14**, 065126.
90 *In Dictionary of Concrete Technology*, Springer Nature Singapore, Singapore, 2025, pp. , pp. 870–871.
91 Y. Suo, X. Zhu, C. Zhao, T. Gong, Z. Li, G. Gao and C. Bi, *Phys. Fluids*, 2025, **37**, 016111.
92 M. A. Islam, S. M. M. Rahman, J. J. Mim, S. Khan, F. Khan, M. A. I. Patwary and N. Hossain, *Chem. Eng. J. Adv.*, 2025, **22**, 100731.
93 R. Rafiu, Md. S. Hasan Saikot, I. A. Apon, I. Boukhris, A. El-Rayyes, M. T. Khan, Q. Mohsen and Md. A. Rahman, *J. Comput. Chem.*, 2025, **46**, e70221.
94 I. A. Apon, S. Jubayer, R. Boudissa, R. Kawsar, R. Rafiu, M. S. Refat, Md. S. H. Saikot, A. M. Alsuhaibani, Md. A. Rahman, Md. A. Hossain and N. Elboughdiri, *J. Inorg. Organomet. Polym. Mater.*, 2025, DOI: 10.1007/s10904-025-03821-5.
95 R. S. Mulliken, *J. Chem. Phys.*, 1955, **23**, 1833–1840.
96 P. Bultinck, C. Van Alsenoy, P. W. Ayers and R. Carbó-Dorca, *J. Chem. Phys.*, 2007, **126**, 144111.
97 M. F. Rahman, M. K. Hasan, M. Chowdhury, M. R. Islam, M. H. Rahman, M. A. Rahman, S. R. A. Ahmed, A. B. M. Ismail, M. Amami, M. K. Hossain and G. A. A. M. Al-Hazmi, *Heliyon*, 2023, **9**, e22866.
98 M. A. Rahman, A. Ghosh, N. S. Awwad, N. Elboughdiri, A. M. Alsuhaibani, Q. Mohsen and M. S. Refat, *J. Phys. Chem. Solids*, 2025, **203**, 112728.
99 M. Amir, I. Masood and M. P. Singh, *Discov. Electron.*, 2025, **2**, 41.
100 M. Saadat and S. Bameri, *Discover Appl. Sci.*, 2025, **7**, 440.
101 M. A. I. Bhuiyan, M. S. Reza, A. Ghosh, H. Al-Dmour, Y. A. Kumar, M. I. I. Rahim, M. Aktarujjaman, F. Yeasmin, H. Al-Lohedan, R. J. Ramalingam and M. S. Reza, *Opt. Commun.*, 2025, **583**, 131761.
102 R. Rafiu, M. S. H. Saikot, A. El-Rayyes, I. A. Apon, M. Shkir, M. T. Khan, M. A. Sayed and M. A. Rahman, *J. Phys. Chem. Solids*, 2026, **208**, 113126.
103 A. M. M. Ul Akhir and M. T. Imam, *GUB J. Sci. Eng.*, 2022, **8**, 41–48.
104 M. S. Uddin, S. M. A. Rahman, M. A. Rahman, S. Mia, M. M. Rahman and M. S. Refat, *J. Phys. Chem. Solids*, 2025, **200**, 112622.
105 M. A. Rahman, A. Ghosh, N. S. Awwad, N. Elboughdiri, A. M. Alsuhaibani, Q. Mohsen and M. S. Refat, *J. Phys. Chem. Solids*, 2025, **203**, 112728.